

From bio-based residues to nanofibers
using mechanical fibrillation for
functional biomaterials



Linn Berglund

Wood and Bionanocomposites

From bio-based residues to nanofibers using mechanical fibrillation for functional biomaterials

Doctoral thesis by

Linn Berglund



Luleå University of Technology
Department of Engineering Sciences and Mathematics
Division of Materials Science
November 2019

Principal supervisor:

Professor Kristiina Oksman (Luleå University of Technology, Sweden)

Co-supervisor:

Professor Mohammad L. Hassan (National Research Centre, Egypt)

Faculty Opponent:

Associate Professor Monika Österberg (Aalto University, Finland)

Evaluation Committee:

Associate Professor Richard T. Olsson (KTH, Sweden)

Senior researcher Carlos Martín (Umeå University, Sweden)

Associate Professor Akram Zamani (University of Borås, Sweden)

Printed by Luleå University of Technology, Graphic Production 2019

ISSN 1402-1544

ISBN 978-91-7790-444-1 (print)

ISBN 978-91-7790-445-8 (pdf)

Luleå 2019

www.ltu.se

To my wonderful family

ACKNOWLEDGMENTS

I would like to acknowledge the financial support of the European Commission under INCOM EC FP7, Industrial Production Processes for Nanoreinforced Composite Structures, Grant Agreement No: 608746; Bio4Energy—a strategic research environment appointed by the Swedish government; the European Regional Development Fund under Interreg Nord: Sea-Surf-Snow project, Grant Agreement No: 20201287; and the Swedish Research Council within the project on ultrafiltration: membranes based on cellulose nanomaterials from agricultural waste for sustainable cleaning of water (Project No.2015-05847).

This work would not have been possible, nor as rewarding, and enjoyable without the following people that I acknowledge:

My supervisor, Kristiina Oksman for giving me the opportunity to work within these projects, along with introducing me to these fascinating materials. Your work ethics, support, knowledge and advice during the realization of my doctoral journey have been a fundamental part of my development as a researcher, thank you for that. My co-supervisor, Mohammad L. Hassan for the fruitful scientific discussions during hours of fibrillation, as well as after. My former co-supervisors, Yvonne Aitomäki and Mehdi Jonoobi, for your support, discussions and advice.

My co-authors, Maxime Noël, Tommy Öman, Ikenna Anugwom, Mattias Hedenström, Jyri-Pekka Mikkola, and Fredrik Forsberg for your valuable contributions and collaboration. All my former and present colleagues and friends at the division of materials science, especially the wood and bionanocomposite group for the joyful working environment.

My whole family for being so wonderful and reminding me about what is important in life. Lennox, du är anledningen till varför “mamma jobbar med små morötter”, och Tommy för att du är en ”miljömupp” med mig. Farfar och farmor, tack för att ni finns. Mamma, tack för att du är du!

November 2019, Luleå
Linn Berglund

Bio-based resource utilization in different forms has been driven by societal, industrial and academic research interests towards the development of “green”, sustainable materials from renewable sources. Within this context, exploiting biomass from different industrial residues is further advantageous from an environmental and economic point of view, leading to minimization of residues by means of waste treatment and to the development of high-added-value- products. Breaking down the cell wall structure to its smallest structural components is one means of turning bio-based residues into high-value products, leaving us with nanofibers. The aim of this work has been to understand how these nanofibers can be liberated from various cellulosic sources using mechanical fibrillation and how they can be assembled into functional hydrogels.

The production of bio-based nanofibers as a sustainable bio-based material is in the early stages of commercialization and considerable research has been devoted to explore different methods of reaching nanoscale. However, the extraction process by chemical and/or mechanical means is still associated with a relatively high energy demand and/or cost. These are key obstacles for use of the material in a wide range of applications. Another challenge is that methods to characterize nanofiber dimensions are still being developed, with few options available as online measurements for assessing the degree of fibrillation. Allowing for assessment during the fibrillation process would enable not only optimization towards a more energy efficient fibrillation, but also matching of the nanofiber quality to its intended function, since different applications will require widely different nanofiber qualities.

Energy-efficient fibrillation and scalability from industrial residues were explored using upscalable ultrafine grinding processes.

Nanofibers from various industrial bio-residues and wood were prepared and characterized, including the development of a method for evaluation of the fibrillation process online via viscosity measurements as an indication of the degree of fibrillation down to nanoscale. Furthermore, the correlation of viscosity to that of the strength of the nanopapers (dried fiber networks) was evaluated for the different raw materials.

Switchable ionic liquids (SIL) were tested as a green pretreatment for delignification, without bleaching of wood prior to fibrillation, with the aim to preserve the low environmental impact that the raw material source offers.

In order to employ the hydrophilic nature and strong network formation ability of the fibrillated nanofibers, they were utilized in the preparation of functional biomaterials in the form of hydrogels. Firstly, brewer’s spent grain nanofibers were used to promote and reinforce hydrogel formation of lignin-containing arabinoxylan, resulting in a hydrogel completely derived from barley residues. In addition, alginate-rich seaweed nanofibers from the stipe (stem-like part of the seaweed) were used directly after fibrillation as an ink and hydrogels were formed via 3D printing.

Keywords: Nanofibers; Industrial residues; Ultrafine grinding; Energy-efficiency; Network formation; Hydrogel

LIST OF APPENDED PAPERS

- Paper 1.** Berglund L., Noël M., Aitomäki Y., Öman T., Oksman K. *Production potential of cellulose nanofibers from industrial residues: efficiency and nanofiber characteristics*. Industrial Crops and Products, 92 (2016) 84-92.
- Contribution:** Participated in planning, performed the majority of the experiments and wrote part of the manuscript under supervision of K. Oksman and Y. Aitomäki.
- Paper 2.** Berglund L., Anugwom I., Aitomäki Y., Mikkola JP., Oksman K. *Switchable ionic liquids enable efficient nanofibrillation of wood pulp*. Cellulose, 24 (2017) 3265-3279.
- Contribution:** Participated in planning, performed part of the experiments and wrote the majority of the manuscript under supervision of K. Oksman and Y. Aitomäki.
- Paper 3.** Berglund L., Forsberg F., Oksman K. *Direct preparation of alginate/cellulose nanofiber hybrid-ink from brown seaweed for 3D biomimetic hydrogels. To be submitted*
- Contribution:** Developed the research idea, performed most of the experiments (X-ray microtomography was conducted together with the co-author) and wrote the manuscript under supervision of K. Oksman.
- Paper 4.** Berglund L., Forsberg F., Jonoobi M., Oksman K. *Promoted hydrogel formation of lignin-containing arabinoxylan aerogel using cellulose nanofibers as a functional biomaterial*. RSC Advances, 8 (2018) 38219-38228.
- Contribution:** Participated in planning, performed the majority of the experiments (X-ray microtomography was conducted together with the co-author) and wrote the manuscript under supervision of K. Oksman and M. Jonoobi.

CONTRIBUTIONS NOT INCLUDED IN THE THESIS

- Paper 5.** Zhou X, Sethi J, Geng S, Berglund L, Frisk N, Aitomäki Y, Sain, MM, Oksman K. Dispersion and reinforcing effect of carrot nanofibers on biopolyurethane foams. *Materials and Design*, 110 (2016) 526-531.
- Paper 6.** Kusano Y, Berglund L, Aitomäki Y, Oksman K. Gliding arc surface modification of carrot nanofibre coating: Perspective for composite processing. *IOP Series: Materials Science and Engineering*, 139 (2016) 1-8.
- Paper 7.** Kusano Y, Berglund L, Aitomäki Y, Oksman K, Madsen B. Dielectric barrier discharge plasma treatment of cellulose nanofibre surfaces. *Surface Engineering*, 34 (2017) 1-7.
- Paper 8.** Hooshmand S, Aitomäki Y, Berglund L, Mathew A, Oksman K. Enhanced alignment and mechanical properties through the use of hydroxyethyl cellulose in solvent-free native cellulose spun filaments. *Composites Science and Technology*, 150 (2017) 79-86.
- Paper 9.** Hassan ML, Abou-Zeid RE, Hassan EA, Berglund L, Aitomäki Y, Oksman K. Membranes based on cellulose nanofibers and activated carbon for removal of Escherichia coli bacteria from water. *Polymers*, 9 (2017) 335.
- Paper 10.** Hassan EA, Hassan ML, Abou-Zeid RE, Berglund L, Oksman K. Use of bacterial cellulose and crosslinked cellulose nanofibers membranes for removal of oil from oil-in-water emulsions. *Polymers*, 9 (2017) 388.
- Paper 11.** Hassan ML, Hassan EA, Fadel SM, Abou-Zeid RE, Berglund L, Oksman K. Metallo-terpyridine-modified cellulose nanofiber membranes for papermaking wastewater purification. *Journal of Inorganic and Organometallic Polymers and Materials*, 28 (2018) 439-447.
- Paper 12.** Hassan ML, Berglund L, Hassan EA, Abou-Zeid RE, Oksman K. Effect of xylanase pretreatment of rice straw unbleached soda and neutral sulfite pulps on isolation of nanofibers and their properties. *Cellulose*, 25 (2018) 2939-2953.
- Paper 13.** Adu C, Berglund L, Oksman K, Eichhorn SJ, Jolly M, Zhu C. Properties of cellulose nanofibre networks prepared from never-dried and dried paper mill sludge. *Journal of Cleaner Production*, 197 (2018) 765-771.

- Paper 14.** Hietala M, Varrio K, Berglund L, Soini J, Oksman K. Potential of municipal solid waste paper as raw material for production of cellulose nanofibers. *Waste Management*, 80 (2018) 319-326.
- Paper 15.** Hassan M, Berglund L, Abou-Zeid R, Hassan E, Abou-Elseouda W, Oksman K. Nanocomposite film based on cellulose acetate and lignin-rich rice straw nanofibers. *Polymers*, 12 (2018) 1-17.
- Paper 16.** Hassan M, Abou-Zeid R, Abou-Elseoud W, Hassan E, Berglund L, Oksman K. Effect of unbleached rice straw cellulose nanofibers on the properties of polysulfone membranes. *Polymers*, 29 (2019) 1-14.
- Paper 17.** Kusano Y, Madsen B, Berglund L, Oksman K. Modification of cellulose nanofibre surfaces by He/NH₃ plasma at atmospheric pressure. *Cellulose*, 26 (2019) 7185-7194.
- Paper 18.** Berglund L, Breedveld L, Oksman K. Toward eco-efficient production of natural nanofibers from industrial residue: Eco-design and quality assessment. Submitted to *Journal of Cleaner Production*.

CONFERENCES CONTRIBUTIONS

Berglund L, Anugwom I, Aitomäki Y, Mikkola JP, Oksman K. Superior Process for Cellulose Nanofibres from Ionic Liquid Treated Wood Chips. *The 10th Biennial Johan Gullichsen Colloquium*. November 19, **2015**, Helsinki, Finland. Poster presentation.

Berglund L, Aitomäki Y, Oksman K. Nanofibre fibrillation: quality measurement and process efficiency of different cellulosic sources. *FPIRC's International Summer conference*, August 30 – September 1, **2016**, Stockholm, Sweden. Conference paper and oral presentation.

Berglund L, Anugwom I, Aitomäki Y, Mikkola JP, Oksman K. Nanofibrillation of switchable ionic liquid pretreated wood pulp. *The Marcus Wallenberg Prize (MWP), Young researchers' challenge*, October 10-13, **2016**, Stockholm, Sweden. Poster and pitch presentation.

Berglund L, Jonoobi M, Oksman K. Xylan-lignin based aerogels and hydrogels - effect of crosslinking degree and nanofibre reinforcement. *Advancements in Fiber-Polymer Composites Symposium*, May 16-18, **2017**, Madison, WI USA, Conference paper and oral presentation.

Berglund L, Breedveld L, Oksman K. Eco-efficient production of natural nanofibers. *Forest Products Society's 72nd International Convention*, June 11-14, **2018**, Madison, WI, USA. Poster presentation.

Berglund L, Gerardin L, Valdecabres B, Forsberg F, Oksman K. From the seaweed forest to multifunctional, bio-inspired foams. *56th Nordic Polymer Days*, June 5-7, **2019**, Trondheim, Norway. Oral presentation.

NOMENCLATURE

EU	European Union
UN	United Nations
ICCT	International Council on Clean Transport
ISO	International Organization for Standardization
NRCAN	Natural Resources Canada
ECS	European Committee for Standardization
I_{am}	Intensity of the amorphous peak
I_{002}	Intensity of the crystalline peak
XRD	X-ray Diffraction
CI	Crystallinity Index
Hz	Hertz
wt. %	Weight percent
rpm	Revolutions Per Minute
BSG	Brewer's Spent Grain
RCG	Reed Canary Grass
FVR	Fruit and Vegetable Residues
XYL	Xylanase
NS	Neutral Sulfite
TEMPO	2,2,6,6-tetramethylpiperidine-1-oxyl
SIL	Switchable Ionic Liquids
DBU	1,8-diazabicyclo-[5.4.0]-undec-7-ene
MEA	Monoethanolamine
STHT	Short Time-High Temperature
SO ₂	Sulfur dioxide
G'	Storage modulus
G''	Loss modulus
AFM	Atomic Force Microscopy
OM	Optical Microscopy
SEM	Scanning Electron Microscopy
AX	Arabinoxylan

CA	Citric Acid
3D	Three-dimensional
STL	Standard Triangle Language
CAD	Computer Aided Design
CaCl ₂	Calcium Chloride
NaOH	Sodium Hydroxide
NaClO ₂	Sodium Chlorite
W ₀	Dry weight of raw material
W ₁	Dry weight after pretreatment
kWh/kg	Kilowatt hour per kilogram
kPa	Kilopascal
kV	Kilovolt
kN	Kilonewton
mA	Milliampere
mM	Millimolar
μl	Microliter
mm	Millimeter
min	Minutes
μm	Micrometer
s	Seconds
W	Watt
σ _{50%}	Strength at 50% strain
E _{50%}	Tangent modulus at 50% strain
W _A	Mass of sample in aerogel state
W _H	Mass of sample in hydrogel state
DMA	Dynamic Mechanical Analysis
Jσ _{max}	Energy at maximum network strength
Jμ _{max}	Energy at maximum viscosity
g	Gram
h	Hours
Eq.	Equation
λ	Wavelength
nm	Nanometer

TABLE OF CONTENTS

Chapter 1 Introduction	13
1.1 BACKGROUND	13
1.2 THE MATERIALS OF NATURE	14
1.3 BIO-BASED NANOFIBERS	16
1.4 NANOFIBERS IN BIOMATERIALS	18
1.5 RESEARCH GAP	19
1.6 AIM OF STUDY	20
Chapter 2 Experimental work	23
2.1 RAW MATERIALS	23
2.2 PRETREATMENTS	24
2.3 MECHANICAL FIBRILLATION.....	24
2.4 PREPARATION OF NANOPAPERS	26
2.5 PREPARATION OF HYDROGELS	27
2.6 CHARACTERIZATION	29
Chapter 3 Nanofibers and functional biomaterials from bio-based residues.....	33
3.1 EFFECT OF RAW MATERIAL	33
3.2 EFFECT OF PRETREATMENT	36
3.3 QUALITY OF MECHANICALLY FIBRILLATED NANOFIBERS.....	37
3.4 ADDED-VALUE BIOMATERIALS FROM MECHANICALLY FIBRILLATED BIO-RESIDUES	42
Chapter 4 Conclusion and future work	47
Appended publications	55

Chapter 1

Introduction

1.1 BACKGROUND

Bio-based resources were the predominant source of energy, organic chemicals and fibers as recently as 150 years ago (Brown et al., 2003). The EU goals of the 2030 EU agenda for sustainable development of our planet target a transition back to making the most of what nature has to offer, including sustainable consumption and production, as well as sustainable usage of our natural resources to meet the needs of the present and future generations (UN, 2019). Staffas et al. (2013) described the concept of bio-based economy and its focus on an economy which is based on the use of bio-based resources rather than fossil-based products and systems, and they further analyzed the strategies for this transition among different countries. Replacing the acknowledged limited fossil resources for energy, chemicals and materials with biomass was identified as a major challenge for all countries in terms of availability. According to the same study, agriculture and forestry alone would not be sufficient to replace the fossil carbon used today, which is consequently a further argument for research on materials from residues/waste streams as raw material.

Exploiting cellulosic biomass, which is considered one of the most important natural resources, from different industrial and agricultural residues is advantageous both from an environmental and economic point of view. This applies to the entire chain of resources, from sustainable use of raw materials to the reduction of residues by means of waste treatment or disposal (Huppes and Ishikawa, 2005), and furthermore to the development of high-added-value products. One of these products has emerged by separating the cellulose to its smallest structural components; nanofibers.

The estimated sustainable availability of cellulosic biomass from residues in the EU has been reported to be about 220 million tonnes per year, with an equivalent available quantity foreseen for 2030 (ICCT, 2013). The majority is estimated to come from crop residues, but waste from industrial processing such as paper and food, or forestry residues constitute the other categories. However, it should be noted that some wastes and residues should be considered as low-value input materials, while others may still provide environmental benefit.

1.2 THE MATERIALS OF NATURE

Cellulose is the main structural component of plants, found in different sources like higher plants (wood), annual plants (crops, vegetables), as well as underwater plants (aquatic). The majority of cell walls in terrestrial plants consist of cellulose, hemicelluloses, lignin as main components, where lignin acts as a binder between cellulose and hemicelluloses components. Plant materials are made up of either simple tissues (a single type of cell), or complex tissues (different types of cells), each with their own structure. The composition of the main components, their arrangement and complexity is highly dependent on the source and its environment. (Hamad et al., 2002)

These variations in the natural hierarchical microstructure of plants give rise to a wide range of mechanical properties. An illustration of the log–log scales of strength as a function of elastic modulus for three groups of plant materials woods, parenchyma and arborescent palm stems is shown in Figure 1.1. (Gibson et al., 2012)

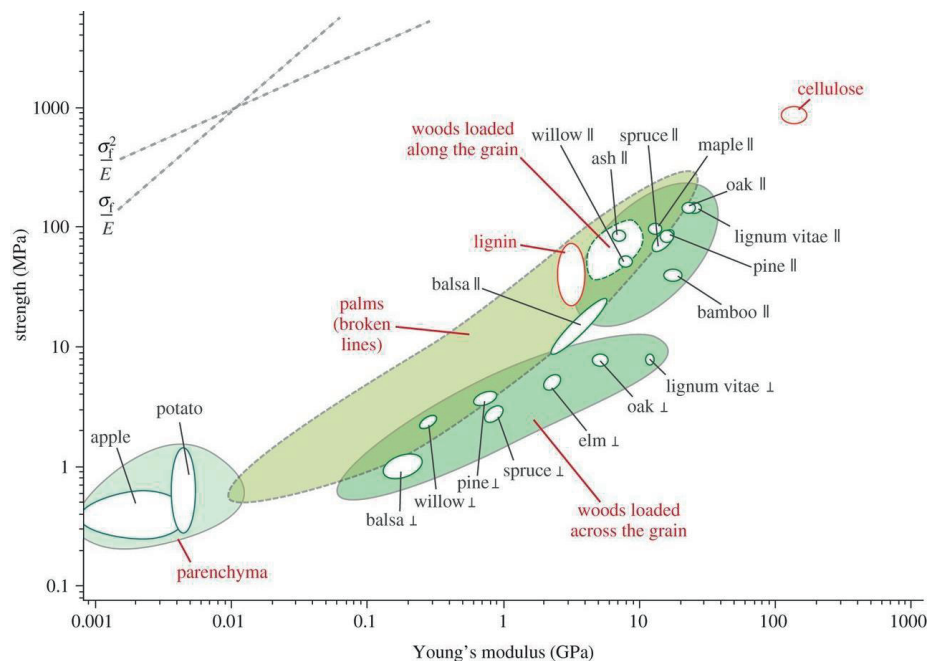


Figure 1.1 Strength as a function of Young's (elastic) modulus for selected plant materials. The properties of the cellulose and lignin are indicated in red. Reprinted from Gibson et al., 2012 with kind permission from The Royal Society.

Annual plants such as crops and vegetables are not designed by nature to stand tall for many years; consequently, they constitute a less complex structure compared to that of wood. Carrots, for example, are made up of a simple tissue: parenchyma with thin-walled, foam-like,

polyhedral cells with low mechanical robustness, as seen from the low stiffness and strength in Figure 1.1 (Gibson et al., 2012).

Higher plants such as trees derive from complex plant tissues, with different cells, depending on type of specie, and thus display high stiffness and strength overall (Figure 1.1). For wood, the hierarchical arrangement throughout the tree not only serves as a mechanical support, allowing them to grow tall, but also allows for performance of functions such as moisture transport that are critical for the survival of the tree. (Hamad et al., 2002)

Aquatic plants such as seaweeds absorb water and nutrients in all their tissues directly from the surrounding water. For this reason, they do not have the complex system of roots, specialized tissues and leaves that help plants transport water and nutrients. In addition, the building blocks of seaweed differ from those found in terrestrial plants, as well as between their three categories red (rhodophyta), brown (phaeophyta) and green (chlorophyta), where the green are the most complex and most closely resemble plants. Cellulose is present in all categories, although, for example, the major structural component of the cell wall in brown seaweed is alginate. (McHugh et al., 2003)

The diversity found in natural materials, both below and above water; gives rise to considerable variation in composition and robustness of the cell wall structure (Hamad et al., 2002). This, in turn, will further dictate how much effort is required to isolate building blocks from the plant and pose challenges as to how to make the most of them when refining and utilizing these resources. Today, the most common method for isolating/producing liberated cellulose (pulp) fibers is from wood as a raw material source using the sulfate (kraft) process that was invented already during the 19th century (Gierer et al., 1980).

The hierarchical structure of hardwood, from macro- to microscale, is shown in Figure 1.2, where a piece of the cross section (a) is magnified with SEM to visualize the wood cells (b,c). Cellulose fibers are embedded in a matrix of hemicellulose and lignin and liberation of these from the cell wall is carried out by degradation of the lignin (Figure 1.2 d,e) . The cellulose fiber is further made up of parallel linear chains of several hundreds to thousands of β -(1 \rightarrow 4)-D-glucose units held together by hydrogen bonding. The chemical structure of cellulose repeating cellobiose unit is shown in Figure 1.2 (g), which forms fibrils typically about 1.5-3.5 nm (f), often referred to as elementary fibrils (Klemm et al., 2005) that in turn form bundles of cellulose microfibrils (e, f), typically about 10-20 nm in width (Hamad et al., 2002; Schniewind et al., 1989). These fibrils are what considered cellulose nanofibers. How they can be liberated is further discussed in the following section.

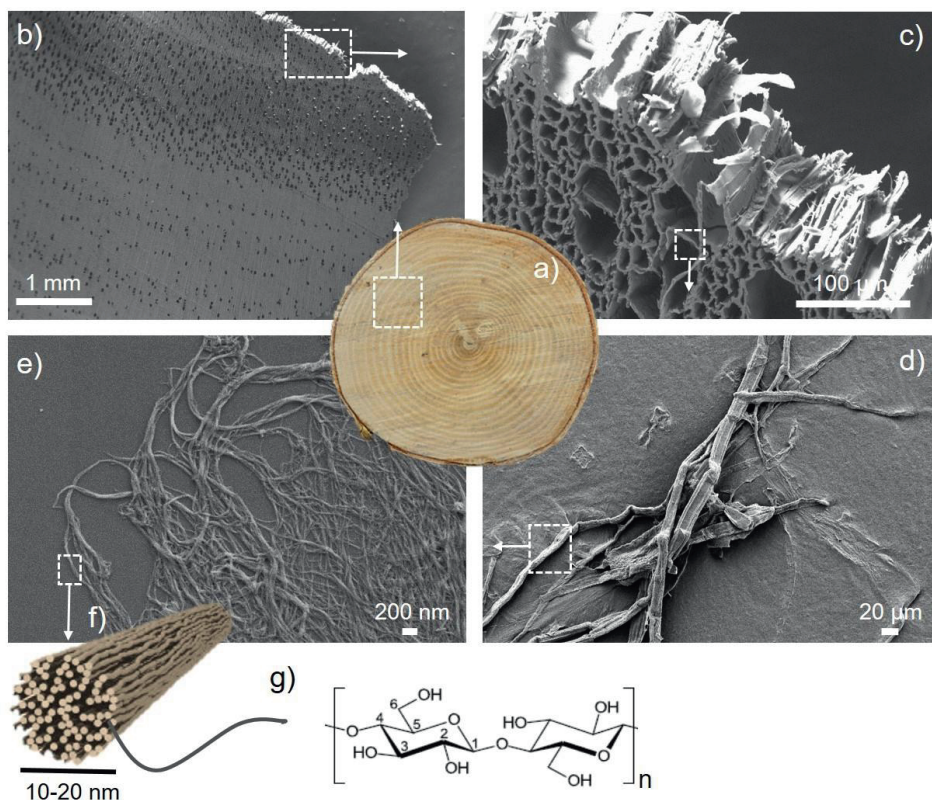


Figure 1.2 Hierarchical structure from hardwood to cellulose at different length scale. a) Macroscale cross section of wood, b) magnification, and c) higher magnification and of the cell wall structure of wood, d) liberated cellulose fibers (pulp), e) cellulose microfibrils (nanofibers), f) schematic of elementary fiber bundles that make up the cellulose microfibrils, g) chemical structure of cellulose, drawn from Hamad et al. (2002), (numbering system for carbon atoms), where “n” is the number of repeating cellobiose units.

1.3 BIO-BASED NANOFIBERS

A nanomaterial is defined according to ISO, 2015 as: “a material with any external dimension in the nanoscale (size range from approximately 1-100 nm) or having internal structure or surface structure in the nanoscale”. The term “bio-based” is defined according to ECS, 2014 as a material derived from biomass, where the biomass can have undergone physical, chemical or biological treatment(s). Within the field today, nanosized fibers are considered as cellulose nanofibers and the nomenclature used is as broad as the field is extensive. For this work, they are referred to as bio-based nanofibers, or simply nanofibers since they are derived from different plants or residue originating from biomass, and with different composition of cellulose, hemicellulose and lignin.

Since the beginning of the 21st century, there has been an exponential increase in the number of publications within the field nanosized materials. Turbak et al. published the first paper on

mechanical fibrillation of microfibrillated cellulose from wood pulp already in 1983 (Turbak et al., 1983). Due to the high energy consumption during the production of the nanofibers the research and development took a significant leap more than two decades later, in part owing to the forest product industries' need to find new uses for pulp, owing to the negative impact of digital technology on the market for paper. Another contributing factor was the development of chemical pretreatments that significantly reduced the energy consumption of the fibrillation process and further engaged industrial interest. Today nanofibers are still mainly produced from already bleached wood pulp. However, using different methods, nanosized fibers have also been extracted from various types of industrial bio-based residues worldwide, for example: wheat straw and soy hulls (Alemdar and Sain, 2008), rice straw and bagasse (Hassan et al., 2010), paper sludge (Jonoobi et al., 2012), orange peel (Hideno et al., 2014), and carrot residue (Siqueira et al., 2016). Residue materials can offer a reduced energy demand, owing to the already processed and partly separated raw material (Joonobi et al., 2014). Moreover, residues from plants with parenchyma cells, such as carrot, have shown further benefits from an efficiency point of view, where the accessibility of the nanofibers originates from their naturally less complex, robust structure (Figure 1.1).

The most common techniques used for the production of the nanofibers include homogenization (high-pressure homogenizer or microfluidizer) and ultrafine grinding. In addition, different pretreatments can be utilized before mechanical processes in order to facilitate the liberation of the nanofibers, hence reducing energy consumption, including oxidation mediated by the 2,2,6,6-tetramethylpiperidine-1-oxyl (TEMPO) radical (Saito et al., 2006), enzymatic pretreatment (Pääkkö et al., 2007) and carboxymethylation (Wågberg et al., 2008).

The aim of mechanical fibrillation is to go from fibers with widths in μm and lengths in mm scale to nanofibers with widths in the nanoscale (below 100 nm) and lengths of a couple of micrometers. The energy input needs to be high enough to break the interfibrillar bonding while avoiding extensive cutting that would reduce the length and, in turn, the aspect ratio. By applying high-pressure through a tiny gap (high-pressure homogenizer), or a thin chamber of specific geometry (microfluidizer), mechanical fibrillation through strong shearing forces is achieved. For a longer period an obstacle to commercial use of homogenization was the vast energy demand, which could reach about 70 kWh/kg (Eriksen et al., 2008). The current major challenge for industrial homogenization is the clogging of the system when long fibers are used (Spence et al., 2011). These issues have been addressed through pretreatments, significantly reducing the energy demand of the mechanical fibrillation, and to some extent the clogging. However, from a holistic and producers' perspective, the energy-intensive mechanical fibrillation part of the manufacturing is only the tip of the iceberg, where the overall environmental impact can be substantially higher for some combinations of pretreatments and homogenization (Arvidsson et al., 2015).

Mechanical fibrillation using ultrafine grinding was first used in the preparation of nanofibers by Taniguchi and Okamura, (1998). For instance, bleached kraft pulp in a water suspension with 5-10% fiber concentration was passed 10 times through the grinder in order to obtain

nanofibers of about 20-90 nm. The fibrillation to nanoscale progresses through shearing forces generated by two grindstones, one static and the other rotating, at a set speed. This setup allows a pulp suspension, without additional pretreatment or pre-refining, to be passed directly between the stones without the occurrence of clogging. From this perspective, ultrafine grinding has shown to be more energy-efficient method when compared to high-pressure homogenization (Spence et al., 2011). The output size is determined by setting the position of the lower grinding stone to control the clearance between the stones while adjusting the shearing forces through the rotor speed. Tuning process parameters such as rotor-speed processing time in relation to the energy demand has further been investigated by Jonoobi et al., (2012). Most commonly, a rotational speed of 1500 rpm or below has been applied as favorable from a process efficiency perspective. Depending on the application and intended function, a number of combinations with pretreatments and mechanical fibrillation can be employed with an aim to governing the output nanofiber characteristics.

Production of nanofibers has enormous potential to provide an important material platform for sustainable production in numerous product sectors and this emerging material is in the early stages of commercialization, with worldwide industrial development, mainly from the pulp and paper industry, using different approaches and involving countries such as Japan, China, Canada, Finland and Sweden. (Sharma et al., 2019) For example, Nippon Paper Industries in Japan has installed the world's largest facility of its kind for the commercial production of nanofibers from wood. This facility employs TEMPO-mediated oxidation of the pulp followed by homogenization and has a production capacity of 500-1500 ton per year (Isogai et al., 2018). However, the production process by chemical and/or mechanical means is still associated with a relatively high energy demand and production cost, key obstacles for use of the material in a wide range of applications (Delgado-Aguilar et al., 2015). The current cost is highly dependent on the method used, but a manufacturing cost in the range of \$40-100 per kg has been reported. (Isogai et al., 2018). A market analysis on bio-based nanomaterials (nanocrystals and nanofibers), made in 2014 by the US Forest Products Laboratory, estimated a market of 33 million metric tons for "high-volume products", including areas such as replacements for plastics, barriers and additives to cement (Shatkin et al., 2014; Cowie et al., 2014). For these rather rough, and optimistic estimates, the price needs to be in the range of about \$4-11 per kg (Cowie et al., 2014), a difficult task considering the average pulp price of more than \$1000 per ton during the last year (NRCAN, 2019).

1.4 NANOFIBERS IN BIOMATERIALS

Overall, the nanosized dimensions of the fibers provide favorable properties, such as high specific mechanical properties, aspect ratio and large surface area, which dramatically improves their uses as reinforcement in biomaterials over, for example, microscale reinforcements. Still, the size alone to which these materials are processed poses challenges in characterizing the material and, in turn, its commercialization and applications.

Characterization methods based on microscopy, light scattering, centrifugation, fractionation, viscosity (Moser et al., 2015), gel point (Raj et al., 2016) and water retention value (Gu et al.,

2018) have been used to follow the mechanical fibrillation process. In addition, nanopapers (dried nanofiber networks) are commonly prepared and their mechanical properties tested as an indication of the degree of fibrillation and reinforcing potential (Lee et al., 2014).

However, several factors affect the mechanical properties of the nanofiber network, one being the degree and to some extent the homogeneity of fibrillation (Lee et al., 2014). A significant improvement in mechanical properties has been reported upon fibrillation, associated with the porosity decrease, owing to the smaller fiber dimensions, which, in turn, results in the formation of more inter-fiber bonds (Nair et al. 2014), thus giving higher mechanical properties and denser nanofiber networks. The drawbacks of most of these methods are that they are time-consuming, lack standards, or are not applicable as online measurements and thus not industrially feasible. Still, the above mentioned attributes combined with characteristics such as biocompatibility and biodegradability offer an attractive material, alone or in combination with other natural polymers, for applications such as rheological modifiers, bio-material reinforcement, paper additives, tissue engineering and functional materials to mention a few (Österberg and Cranston, 2014). However, their inherent hydrophilicity limits their uses and dispersion in combination with hydrophobic polymer matrices. Although prospects for functionalization owing to their large surface area can be exploited for an improved compatibility, this it is not within the scope of the present work. On the other hand, the hydrophilic nature and network formation ability renders them capable of holding large amounts of water, which could instead be exploited as an advantage for materials such as natural hydrogels.

Hydrogels are hydrophilic polymer chains that can be crosslinked or entangled, capable of holding large amounts of water in their three-dimensional (3D) networks, without the loss of their structural integrity. The design of hydrogels based on natural polymers such as cellulose, alginates, lignin (Sipponen et al., 2019), and hemicelluloses (Alakalhunmaa et al., 2016) has attracted considerable interest. Hydrogels are widely available as commercial materials in hygiene products and wound dressing, yet commercial hydrogel products are still limited to several areas of application, due to some extent to their high production cost, in combination with their low mechanical properties (Caló et al., 2015). The mechanical properties of hemicellulose-based hydrogels have previously been combined with nanofibers for the formation of a reinforcing network (Alakalhunmaa et al., 2016). For alginate-based hydrogels, the addition of nanofiber has not only reinforced the structure (Abouzeid et al., 2018), but also enabled fabrication via 3D printing through increased viscosity combined with shear thinning behavior (Markstedt et al., 2015). Nanofibers have also shown to be beneficial for dimension stability and the presence of an entangled nanofiber network has further shown to significantly affect the material architecture due to the pore size (Siqueira et al., 2019).

1.5 RESEARCH GAP

In order to promote the production of nanofibers, low-cost, large-scale and sustainable production methods are required. Moreover, considerable research has been devoted to explore different means of reaching nanoscale and, as a result, a vast landscape of diverse materials

with different properties and qualities. It is easy to get lost in this jungle of qualities and it is only in the last couple of years that standards for characterization have emerged, among them, ISO, TAPPI and the Canadian Standard Association. Even so, more standardized protocols for the characterization of cellulose nanofibers need to be developed. Quality is a somewhat diffuse concept, where a precise definition is difficult to establish. "Quality" comes from the Latin word *qualitas*, which means properties or attributes. In the marketing terminology, quality is defined as: the degree to which a product fulfils its function, given the needs of the consumer (Box, 1983). A better understanding and assessment of the quality throughout the fibrillation process would enable optimization of the process. Establishing when a "sufficient" nanosize is reached would require fast, preferably online, methods that are simple to interpret. This is a key to reducing the energy consumption in the process. It is essential to quantify the process of separating the pulp into nanofibers by online characterization methods for quality control if industrial production of nanofibers and full potential and environmental benefits of these materials is to be realized. In addition, the nanofiber quality also needs to be related to application, such as their use as reinforcements in biomaterials, and/or tailoring of the production of nanofibers with specific qualities, since different applications will require widely differing qualities of nanofiber.

1.6 AIM OF STUDY

The main objective of this work was to prepare nanofibers from bio-based residues using the mechanical fibrillation process and to gain a deeper understanding of the process and the relationship between the process, raw materials, pretreatment, properties and potential uses. The specific aims can be summarized as follows:

- understand how to efficiently and with the least environmental impact disintegrate a raw material to its smallest structural component using mechanical fibrillation;
- develop an approach for online assessment of the nanofiber quality during the different stages of fibrillation;
- improve comprehension regarding scalable and energy-efficient production routes using bio-based residues as a raw material source and their further uses in biomaterials.

Figure 1.3 Summarizes the content of this thesis work.

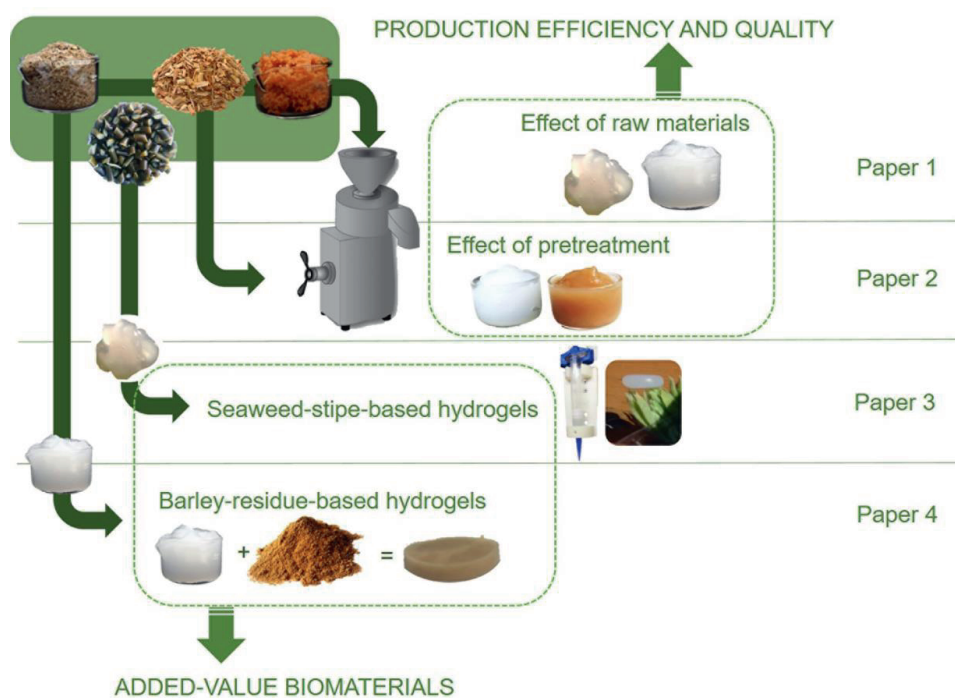


Figure 1.3 An overview of this thesis work according to the contents of the appended papers.

Chapter 2

Experimental work

2.1 RAW MATERIALS

The raw materials used in this work are mainly industrial bio-residues that currently are either burned or used for low-value products such as animal feed.

In Paper 1 the bio-residues included carrot residue, a by-product from carrot juice production, supplied by Brämhults Juice AB, (Brämhult, Sweden), and brewer's spent grain (BSG), a by-product from beer production, mainly the residue of barley after the malting and brewing process, obtained from a Finnish brewery.

Paper 2 focused on hardwood, namely birch (*Betula pendula*) as raw material in the form of chips, provided by the Natural Resources Institute Finland, (Luke). A commercial bleached kraft pulp provided by SCA Munksund AB (Munksund, Sweden) was used as reference material in both Papers 1 and 2.

In Paper 3 brown seaweed, (*Laminaria digitata*) cultivated in the North Atlantic Ocean, was kindly provided by The Northern Company Co. (Træna, Norway). The stipe (stem-like portion) of the seaweed is a by-product from the food industry.

For Paper 4 barley residues were used as raw material source, both for the BSG nanofibers (described above), but also for the hemicellulose; arabinoxylan (AX), originating from barley husk, and were purchased from Xylophane AB (Gothenburg, Sweden). The composition included; 48.5 wt% xylose, 11.7 wt% arabinose, 3.8 wt% glucose, 19.6 wt% lignin, 6.8 wt% protein, 4.2 wt% fats, 4.3 wt% ash and less than 1 wt% starch, as reported by the supplier.

In addition to the raw materials described above, four bio-residues were included in the section on nanofiber quality as supplementary materials for the evaluation. Rice straw was obtained from a farm in Qalubiyah Egypt, and was treated with neutral sulfite and xylanase to obtain a high-lignin containing pulp of about 13 wt.% lignin (14 wt.% for only neutral sulfite treated) (Hassan et al., 2018). Bleached banana rachis pulp was provided by the Pontifical Bolivarian University, (Medellin, Colombia) (Herrera et al., 2015). Reed Canary Grass (RCG) pulp was supplied by Swerea SICOMP (Öjebyn, Sweden). A mixture of fruit and vegetable residues (FVR) after juice processing was kindly provided by Prof. Kristiina Oksman.

2.2 PRETREATMENTS

In general, the received raw materials were first washed with distilled water at 85°C, and subsequently treated with an alkali (2% NaOH) solution at 80°C for 2 h. This low concentration of sodium hydroxide (NaOH) is expected to decrease the hemicellulose concentration but not remove it. To remove lignin, the materials were bleached with sodium chlorite NaClO₂ (1.7%) in an acetate buffer (pH 4.5) 80°C for 2 h under magnetic stirring, and subsequently washed until a neutral pH and a white pulp were obtained. This procedure was carried out once for carrot residue, but repeated three times for BSG (Paper 1) and RCG. Meanwhile, only the bleaching step was performed (once) for the seaweed stipe (Paper 3), and fruit and vegetable residue (FVR). For seaweed stipe, the bleaching aimed to remove pigments, while preserving the cellulose and alginate, obtained at 33 wt.%, and 45 wt.%, respectively, after bleaching.

As an alternative to the bleaching, switchable ionic liquids SIL (SO₂ switched DBU MEASIL), were evaluated as potential pretreatment of wood chips in Paper 2, and its synthesis is described in detail by Anugwom et al., (2011). The Short Time-High Temperature (STHT) approach (Anugwom et al., 2014) was applied and the wood chips were heated to 160°C at a weight ratio of 1:5:3 of wood: SO₂ DBU MEASIL: water for 2 h, without any stirring employed. The treated wood was subsequently subject to washing with a mixture of propanol and water until no visual evidence of the SIL could be found remaining in the solid fraction.

The reference kraft pulp had a chemical composition of 5 wt.% residual lignin, 21 wt.% hemicellulose and cellulose content of 70 wt.%. The SIL-treated pulp had a chemical composition of 5 wt.% residual lignin, 20 wt.% hemicellulose and cellulose content of 75 wt.%. The solid recovery was calculated as yield according to the following equation:

$$\text{Yield \%} = W_1/W_0 \times 100 \quad (\text{Eq. 1})$$

where W_1 indicates the dry weight of the sample after the chemical treatment and W_0 indicates the initial dry weight of the residue.

2.3 MECHANICAL FIBRILLATION

Mechanical fibrillation of the prepared pulps was conducted at a concentration between 1.5 - 2 wt.% using MKCA6-3, an ultrafine friction grinder from Masuko Sangyo Co., Ltd. (Kawaguchi, Japan). In addition, carrot residue pulp and kraft pulp were fibrillated using a pilot scale 10" MKZA 10-20J 15 kW ultrafine grinder.

Prior to the grinding the suspensions were dispersed using a shear mixer, Silverson L4RT Silverson Machine Ltd. (Chesham, UK), with the exception of seaweed stipe, which was in the form of intact structures after the bleaching and was passed directly through the grinder.

The fibrillation was conducted in contact mode upon initial feeding and gradually adjusted to 90 μm (negative) by setting the position of the lower grinding stone to control the clearance between the stones with a maintained rotor speed of 1500 rpm. Coarse silicon carbide grinding stones, which are non-porous standard stones for soft materials, were used in this process. The pulp is subjected to compression and shearing forces in the grinding process, which affects the fibrillation and thereby the size of the fibrillated material. An overview of the process from raw material to nanofibers is shown in Figure 2.1.

The determination of the energy consumption in the fibrillation process was based on the direct measurement of power using a Carlo Gavazzi EM24 DIN power meter (Belluno, Italy) and the processing time. The cumulative energy demand integrated over the whole fibrillation time was calculated from the following equation:

$$\text{Energy} = \text{power (W)} \times \text{time (h)} \quad (\text{Eq. 2})$$

The energy consumption for the grinding process was expressed as kilowatt hours per kilogram (kwh/kg) of dry weight of nanofibers.

The methodology for assessing the degree of fibrillation through online viscosity measurements was as follows: Viscosity measurements were taken at regular time intervals (10 to 20 min) during the grinding process using a Vibro Viscometer SV-10, A&D Company, Ltd. (Tokyo, Japan), at a constant shear rate. Periodical circulation of the sensor plates from zero to peak (sine-wave vibration), at a frequency of 30 Hz. Simultaneously, a polarizing microscope, Nikon Eclipse LV100N POL (Kanagawa, Japan) with imaging software NIS-Elements D 4.30 was used to study the microstructure during the disintegration. The fibrillation process was stopped when a plateau in viscosity was reached and no intact larger structures could be detected with an optical microscope. The samples were subsequently tested in room temperature to establish the reached plateau before being plotted as a function of the energy demand.



Figure 2.1 Process steps from raw material to nanofibers, with an example of OM images of wood pulp during the mechanical fibrillation and a photograph of the ultrafine lab-scale grinder with corresponding coarse grinding stones.

2.4 PREPARATION OF NANOPAPERS

Dried nanofiber networks referred to as “nanopapers” were prepared primarily for mechanical testing to get an indication of the degree of fibrillation at different processing times, where a smaller size (high aspect ratio) corresponds to an increase in strength and elastic modulus of the network. Four of the collected samples during fibrillation were selected for preparation of nanopapers; the starting point (corresponding to the pulp), a point between the starting and maximum viscosity, the maximum viscosity value, the final point, from which no further increase of viscosity had been observed. The nanopapers were also utilized for characterization of crystallinity index and contact angle. The setup for vacuum filtration and the nanopaper of different materials after drying is shown in Figure 2.2.

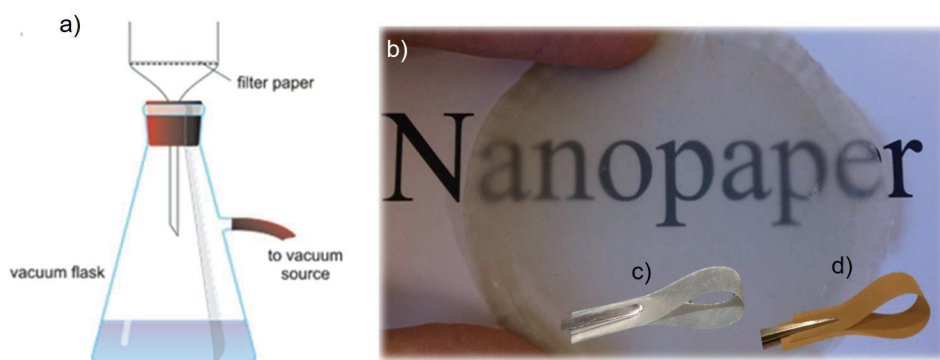


Figure 2.2 a) Setup for the preparation of nanopapers through vacuum-assisted filtration, b) representative photograph of nanopaper derived from wood or bio-residues after bleaching, fibrillation and drying, c) photograph of nanopaper strip from bleached kraft pulp after fibrillation, and d) photograph of nanopaper strip prepared from unbleached SIL treated pulp after the fibrillation process.

The suspensions were adjusted to a concentration of 0.2 wt.% and dispersed with a shear mixer, IKA T25, UltraTurrax, IKA-WerkeGmbH & Co. (Germany), at 10,000 rpm for 10 min followed by degassing before the suspensions were filtered using vacuum-assisted filtration with a membrane filter with a pore size of 0.45 μm and a glass filter support. The obtained wet cake was subsequently dried using hot pressing at 85°C using a Fortune press, LP300, Fontijne Grotnes (The Netherlands), under 30 kPa, based on the applied force and area of the sample, for about 40 min. This was the standard procedure for the nanopaper preparation used in this work; however, the nanopapers from the seaweed stipe were instead prepared using the solvent-casting method, where the dispersions were left to dry in petri dishes for about three days at room temperature ($22.6 \pm 2^\circ\text{C}$).

2.5 PREPARATION OF HYDROGELS

Figure 2.3 shows the preparation of hydrogels from seaweed stipe carried out using the gel obtained after fibrillation directly as an ink for 3D printing using the INKREDIBLE 3D bioprinter, CELLINK AB, (Gothenburg, Sweden); a pneumatic-based extrusion bioprinter, with a nozzle diameter of 0.5 mm, pressure of 5 kPa and dosing distance of 0.05 mm. The shape was designed in the CAD software 123D Design (Autodesk) and the created STL files were subsequently converted into g-code using Repetier-Host (Repetier Server) software before being printed into solid discs (10 mm diameter, 4 mm high, 10 layers) onto a petri dish. To form hydrogels, the structure was crosslinked with a 90 mM aqueous solution of CaCl_2 for 30 min prior to washing with deionized water.

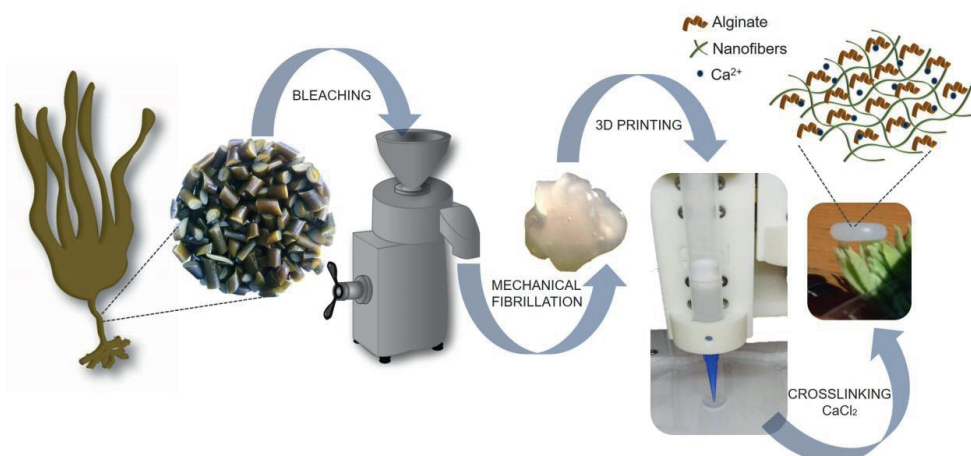


Figure 2.3 Schematic of the hydrogel preparation from the raw material, seaweed stipe. Adapted from Paper 3.

Aerogels and hydrogels of lignin-containing arabinoxylan, AX, with and without the addition of BSG nanofibers, were prepared and crosslinked with 5 wt.% citric acid (CA) to study the effect of nanofibers on the hydrogel properties, see Figure 2.4. AX and CA were mixed in distilled water, under magnetic stirring at 30°C, until the AX dissolved (1 h). The nanofibers were added, under continuous stirring, to obtain an AX/ nanofiber ratio of (1: 1). Both solutions were prepared at a solid content of 2 wt.% and dispersed using a dispersing instrument UltraTurrax, IKA T25, IKA®-Werke GmbH & Co. KG (Staufen, Germany) operated at 10,000 rpm for 10 min. They were subsequently freeze-casted using liquid nitrogen, with only the base of the mold (plastic petri dish) in contact for a bottom-up freezing direction. The samples were placed in a freezer (-20°C) for at least 24 h prior to freeze drying for 48 h using a freeze- dryer Alpha 2-4 LD plus CHRIST GmbH (Osterode am Harz, Germany), under a temperature of -40°C, followed by 3 h in an oven (120°C) for activation of the CA crosslinker. The obtained aerogels were placed in water for hydrogel formation.

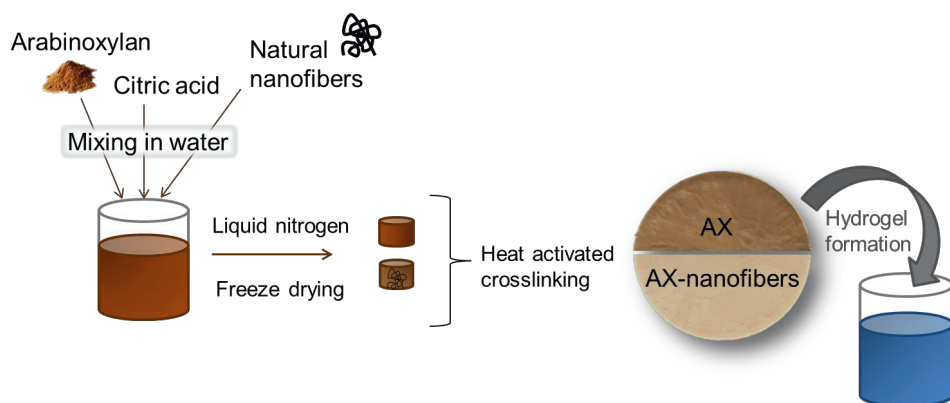


Figure 2.4 Schematic representation of the procedure used to prepare AX- and AX-nanofiber hydrogels. Adapted from Paper 4.

2.6 CHARACTERIZATION

In this section the techniques that were used for the characterization of the raw materials, the pretreated materials, the fibrillated nanofibers and the prepared hydrogels are described.

Scanning electron microscopy (SEM)

A SEM JEOL JSM-IT300 (Tokyo, Japan), was used to image the cell wall structure of the raw materials as well as the fracture surfaces along the freezing direction of the AX samples, with and without the addition of nanofibers, in order to study their effect on the pore structure, at an acceleration voltage of 15 kV. The morphologies of the bio-residues were studied before and after the fibrillation process using Carl Zeiss Merlin field emission FE-SEM (Oberkochen, Germany) at an acceleration voltage of 5 kV. The nanofibers were dried in acetone to reduce their tendency to aggregate and all samples were sputter coated with either tungsten or gold to prevent charging.

Atomic force microscopy (AFM)

The morphology and dimensions of the nanofibers were analyzed using a Veeco Multimode Scanning Probe atomic force microscope (Santa Barbara, USA) in tapping mode in air with a tip model TESPA (antimony (n) doped silicon) Bruker (Camarillo, USA). Prior to imaging the suspensions (0.01 wt.%) were dispersed, and then deposited by spin coating onto a clean mica and left to dry at 22-23°C. The measurements of the nanofiber width were conducted from height images using Nanoscope V software and the average values and deviations presented were based on 40-50 different measurements.

Mechanical properties

The mechanical properties of the prepared nanopapers after different processing times were tested to provide an indication of the degree of fibrillation. Strips were manually cut with a razor (40 mm × 5 mm) and attached to paper frames to facilitate the mounting in the tensile machine. The tests were conducted using universal tensile testing equipment; AG X, (Shimadzu, Japan) equipped with 1 kN load cell. The tests were conducted at an extension rate of 2 mm/min and gauge length of 20 mm. All samples were conditioned at 50 ± 2.0% relative humidity at 23 ± 1.0°C for at least 24 h prior to testing. The average values presented are based on at least eight sets of measurements.

X-ray diffraction (XRD)

A PANalytical Empyrean X-ray diffractometer (Almelo, The Netherlands) equipped with a PIXcel^{3D} detector and Cu-K_α radiation source ($\lambda=0.154$ nm) was used to evaluate the crystallinity from the nanopapers prepared before and after fibrillation. The X-ray generator was operating at 45 kV and 40 mA. A baseline correction was used (Sonneveld and Visser, 1975) before the crystallinity index (CI) was estimated according to the peak height method (Segal et al., 1959):

$$CI = [(I_{002} - I_{am}) / I_{002}] \times 100 \quad (\text{Eq. 3})$$

where I_{002} is the intensity of the crystalline peak and I_{am} refers to the intensity of the amorphous peak.

Contact angle

The nanopapers were further used to evaluate the wettability of the nanofibers using water contact angle measurements with an EASYDROP measuring system, drop shape analysis control (DSA1) and evaluation software Krüss GmbH (Hamburg, Germany). A 4 μL water drop was placed onto the samples and the contact angle was calculated using the sessile drop technique. The reported values were the average of five measurements for each sample.

Rheology

The seaweed stipe nanofibers were characterized according to its rheological behavior to evaluate suitability as an ink for 3D printing using Discovery HR-2 rheometer TA Instruments (Elstree, UK) at 25°C. The shear viscosity was measured at shear rates from 0.01–1000 s^{-1} , using a cone-plate (20 mm). In addition, the crosslinking of the ink was evaluated by adding a 1 mL drop of 90 mM CaCl_2 solution causing it to gel, meanwhile simultaneously measuring the storage and loss modulus with a plate-plate configuration (8 mm, gap 500 μm). The oscillation frequency measurements were conducted at 0.1% strain, based on oscillation amplitude sweeps to establish the linear viscoelastic region, and at a frequency of 1 Hz for 10 min.

X-ray microtomography

To study the internal architecture of the 3D printed and crosslinked seaweed stipe ink a sample (4 x 4 x 4 mm) was scanned using a Zeiss Xradia 510 Versa Carl Zeiss (Pleasanton CA, USA) with a 20x objective, a field of view of 0.56 mm and voxel size of 0.56 μm . The scanning was carried out with an X-ray tube voltage of 50 kV, an output effect of 4 W, without any X-ray filters. 2401 projections were acquired with an exposure time of 6 s, resulting in a scan time of 6 h. The tomographic reconstruction was carried out using filtered back projection within Zeiss Scout-and-Scan Reconstructor software (version 11.1). The 3D visualization and analysis were performed with Dragonfly Pro Software (ORS). Prior to analysis the sample had been frozen (-20°C) for at least 24 h and freeze dried (-40°C), using a freeze dryer Alpha 2-4 LD plus CHRIST GmbH (Osterode am Harz, Germany), for 48 h.

Swelling properties

The AX and AX-nanofiber samples in dry state (aerogels) were immersed in distilled water at room temperature for hydrogel formation and to determine their functionality in terms of swelling behavior. The swollen hydrogels were gently blotted in filter paper to remove any excess water before being weighed at regular intervals until an equilibrium state was reached. The average values are based on three measurements. The equilibrium swelling ratio was calculated using the following equation:

$$\text{Swelling ratio (g/g)} = [(W_H - W_A) / W_A] \quad (\text{Eq. 4})$$

where W_A and W_H denote the mass of the sample under the aerogel state and the swollen hydrogel state, respectively.

Compression properties

Uniaxial compression tests were performed on the prepared AX and AX-nanofiber samples in hydrogel state to evaluate the effect of nanofibers on the mechanical behavior using a dynamic mechanical analyzer DMA Q800, TA Instruments (New Castle, USA) at 25°C. The samples with dimensions of 15 × 15 mm and a height of 10 mm were preloaded using a load of 0.05 N and compressed up to a strain of 100% at a strain rate of 10 % min⁻¹. The hydrogels were compared by the stress ($\sigma_{50\%}$) and tangent modulus ($E_{50\%}$) at a 50% compressive strain level, based on eight tests for each sample.

Nanofibers and functional biomaterials from bio-based residues

In this chapter a summary of the main results obtained in this thesis work are presented and more detailed information of the results can be found in the appended Papers 1 to 4. The influence of choice of raw material (Papers 1, 2 and 3) and pretreatments (Paper 2) on the process efficiency are reported for the fibrillation of residues and wood into nanofibers using mechanical fibrillation via ultrafine grinding. Furthermore, an approach for online evaluation of the fibrillation process through viscosity measurements, along with key characteristics, is summarized (Papers 1, 2, 3 and 4). In addition, the utilization of mechanically fibrillated residue-based nanofibers for functional biomaterials is summarized from Papers 3 and 4.

3.1 EFFECT OF RAW MATERIAL

In this section the effect of raw material when going from bio-based residues to nanofibers is summarized from Papers 1, 2 and 3. To study the effect of raw materials on process efficiency the process was evaluated in terms of yield and energy consumption of the ultrafine grinding process. The output quality is discussed more in detail in section 3.3. During the fibrillation process, the degree of fibrillation is studied using online viscosity measurements in combination with OM. The goal of the fibrillation process is to reach a viscosity plateau implying a stronger network formation connected to the disintegration of fibrils which promotes the fibril-to-fibril bonding. When using OM, the absence of the larger structures was considered as an indication of the fibrillation progress. In addition, the morphology was studied using SEM and the mechanical properties of the prepared nanopapers were tested.

Four raw materials originating from four different categories, namely forestry (wood pulp), root vegetable crop (carrot), cereal crop (barley), and seaweed (brown seaweed stipe), are included and shown in Figure 3.1. The wood pulp, a commercial kraft pulp, was chosen as a reference material. The three other categories are industrial residues from the juice industry in the form of carrot residue and brewer's spent grain (BSG), which is an industrial residue of barley after the brewing and malting process for beer production. The brown seaweed is mostly used for production of alginate, though the blades also can be used in the food industry, where the stipe is considered a residue that is discarded.

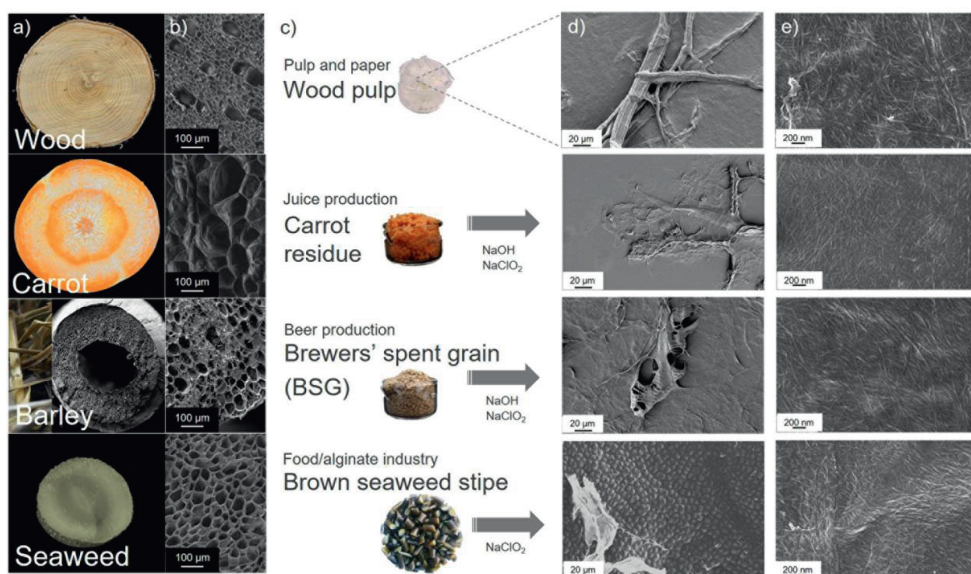


Figure 3.1 a) Photographs and micrograph barley of the cross section of the plant stem and b) their cells, c) photographs of the already bleached wood pulp and the residues before bleaching. d) before fibrillation and e) after fibrillation of the raw materials; wood pulp, carrot residue, BSG, and seaweed stipe respectively (in descending order). Adapted from Paper 1 and 3.

The raw materials were studied according to their inherent cell wall structure and their morphology before (as pulp) and after the fibrillation process using SEM. Figure 3.1 shows the cross section of the different material stems (a), and the SEM images of the cell wall (b), the raw materials (c), pulp (d) and nanofibers (e) derived from the four different raw materials. Moreover, the corresponding OM images before and after fibrillation are presented in Figure 3.2, together with the viscosity measurements and elastic modulus and strength of the nanopapers from samples taken during fibrillation.

The yields of the residues after bleaching are 32%, 22%, and 71% for carrot residue, BSG, and seaweed stipe, respectively (Figure 3.1). However, it should be noted that the yield more than doubled when carrot residue was directly bleached, without the alkali step (Berglund et al., 2019), owing to the higher non-cellulosic content. The high yield of seaweed stipe is also attributed to high non-cellulosic content in form of alginate, present in a higher amount than cellulose (Paper 3). Furthermore, the bleaching of carrot residue and seaweed stipe requires less chemical use in comparison to both BSG and wood.

The higher magnification SEM images show separated nanofibers from wood pulp, carrot, BSG and seaweed residues, respectively, after the fibrillation process (Figure 3.1e). However, the nanofibers from seaweed stipe were embedded in alginate, and not many areas of the examined sample surface, where they were easily distinguished. In addition, the OM images displayed the absence of intact micro-sized structures after the fibrillation process (Figure 3.2a).

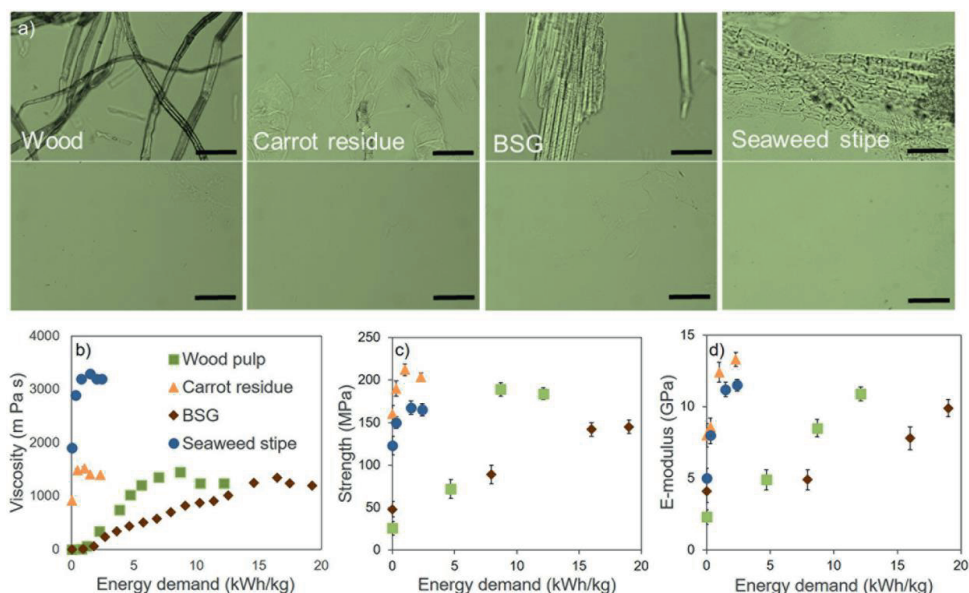


Figure 3.2 a) OM images of the pulp and nanofibers derived from the four raw material sources, scale bar: 100 μm , b) the viscosity measurements (in 22-23°C) as a function of the energy demand from samples taken during the mechanical fibrillation process. c) The corresponding strength, and d) the elastic modulus of the prepared nanopapers from the samples, tested in tensile. All samples were processed at 2 wt.%

The increased viscosity during the fibrillation process, connected to the disintegration of fibrils, forming a stronger network was apparent for all materials (Figure 3.2b). The viscosity was higher for seaweed stipe, in part owing to its high alginate content, which is known for its gel-forming ability (Peteiro et al., 2017). The plateau in viscosity was further observed for all materials; however, the difference in energy consumed in order to reach this plateau distinguishes the materials. Moreover, the corresponding network properties, as tested from the nanopaper, showed an obtained plateau in strength (Figure 3.2c), during the fibrillation, while the elastic modulus appeared to still be increased (Figure 3.2d). This behavior was observed for all the materials. Carrot residue reached the highest mechanical network properties upon fibrillation, and with the least amount of energy consumed, in part owing to the initially higher properties of carrot residue pulp (Figure 3.2c, d). Altogether, the microscopy techniques combined with network characteristics indicate an overall comparable degree of fibrillation and show that what mainly distinguishes the raw materials is how much effort is required to reach nanoscale.

The efficient separation of carrot residue and seaweed stipe into nano-sized fibers can be attributed to the more accessible fiber in the inherently less complex cell wall structures (Figure 3.1a), which after the bleaching is already partially disintegrated (Figure 3.2a), in agreement with the initial high viscosity along with the mechanical properties of the carrot pulp. BSG pulp displayed initially larger structures, consuming more energy to be separated, which might have been further influenced by the heterogeneity and drying of the material before pulping. This suggests that the structural differences of the cells, and hence the choice

of raw material, plays an important role for the process efficiency of nanofibers. In addition, an important factor for the process efficiency is the chemical composition, since the amount of non-cellulosic components such as lignin, hemicelluloses, and alginate affects the fibrillation into nanofibers. Though the composition of cellulose, hemicellulose, lignin and alginate is source-dependent, it is to a greater extent process-dependent in terms of the pretreatments performed prior to fibrillation that in turn will influence its efficiency.

3.2 EFFECT OF PRETREATMENT

In this section the effect of pretreatment when going from wood to nanofibers is summarized from Paper 2. The starting materials for separation of nanofibers have generally been bleached cellulose pulps. In addition to saving costs and reducing pollution resulting from the bleaching processes, fibrillation from unbleached pulp could provide an alternative approach to improve environmental performance. The potential of an alternative method to enable efficient delignification without bleaching was performed using SIL (Paper 2). The potential of SIL was investigated as pretreatment for delignification of wood prior to fibrillation, using commercially bleached kraft pulp as a reference material. Furthermore, to highlight the effect of pretreatments and subsequent chemical composition and its role on the fibrillation process, and network properties, high-lignin-containing rice straw pulps were used for comparison (Hassan et al., 2018).

On one hand, a high yield promotes a higher efficiency in terms of use of chemicals, water and energy (Berglund et al., 2019); on the other hand, the chemical composition of a fiber influences how it is disintegrated. Consequently, non-cellulosic components such as hemicellulose and lignin are present in a higher amount after pretreatments with high yields.

After the SIL treatment of wood chips, a yield of 60% was obtained. The SIL treatment displayed a comparable delignification efficiency to that of commercially bleached kraft pulp (5 wt.% residual lignin), while preserving the hemicellulose content (20 wt.%). Hemicellulose present during fibrillation using ultrafine grinding have showed to play an important role in the ease of fibrillation (Iwamoto et al., 2008). An overview of the route from raw material to nanofibers applying the different pretreatments is shown in Figure 3.3, together with the viscosity measurement at different processing times throughout the fibrillation.

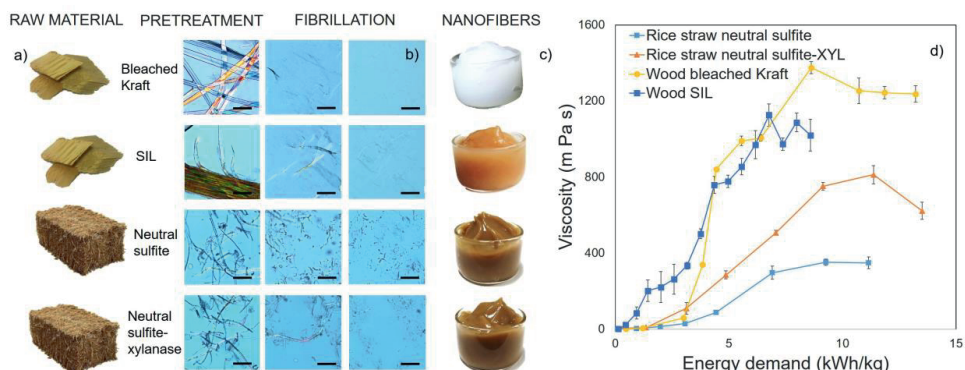


Figure 3.3 a) Photographs of the raw materials b) OM after pretreatments, after 50 min fibrillation and after finalized fibrillation, c) photographs of the fibrillated nanogel. d) Viscosity measurements (in 22.5-23°C) as a function of the energy demand during the mechanical fibrillation process. Scale bar corresponds to 100µm. Adapted from paper 2 and 3.

From Figure 3.3, the different raw materials (a) and pretreatments resulted in gels with varying colors (c). The viscosity increase upon fibrillation and how fast the viscosity plateau is reached differs between the pulps, and further dictates how much energy the process consumes. The initiation of the fibrillation of SIL treated wood was comparable to that of the bleached reference pulp. However, the viscosity plateau was reached at a lower energy demand for SIL-treated pulp, despite the initial larger structures of the pulp (Figure 3.3 b,d) requiring separation before gel formation was induced, namely 9 kWh/kg compared to 13 kWh/kg. Notable is the lower viscosity increase and plateau value of the higher lignin-containing rice straw pulps (Figure 3.3d), signifying the role of lignin, present to a high extent, which hinders the fibrillation process and the network formation. This is also observed from OM images (b), where the intact structures are apparent throughout the fibrillation process, compared to those with lower lignin content.

SIL pretreatment could be an alternative approach to the commercially bleached pulp, with a demonstrated effective delignification, while preserving the hemicellulose, suitable for applications where color is not of importance.

3.3 QUALITY OF MECHANICALLY FIBRILLATED NANOFIBERS

In this section different approaches to characterize the quality output are discussed and compared, along with steps toward industrial production using ultrafine grinding, summarized from Papers 1, 2, 3, and 4. Different approaches to characterize the quality output are discussed and compared. Online quality assessment using viscosity measurements for optimization of process efficiency and a consistent quality output are discussed for several different raw materials and pretreatments. Furthermore, the use of viscosity measurements as an indication of the degree of fibrillation down to nanoscale and its correlation to the strength of the nanopaper is included. In addition, the scalability and potential of ultrafine grinding combined with online assessment for large-scale production is addressed through both lab-scale and pilot-scale production. In addition, widths, crystallinity index and contact angle of the

nanofibers were characterized and are summarized in Table 3.1. The AFM height images of nanofibers after fibrillation from where the widths are measured are shown in Figure 3.4.

XRD measurements for the materials in Table 3.1 were made to evaluate the effect of the mechanical fibrillation on the crystallinity of the materials. The estimated crystallinity indexes were in the range of 59 to 87% (Table 3.1), where the variation could be assigned to the different raw material sources, and pretreatments, and in turn their chemical composition. In addition, before and after the fibrillation the crystallinity indexes were within the same range. These results showed that ultrafine grinding as a fibrillation technique appears to isolate the nanofibers without affecting their inherent structure.

The wettability of the nanofibers is an important parameter for intended use in various applications. From Table 3.1, all nanofibers displayed a hydrophilic behavior with contact angles below 90°, where the difference in the wettability can be assigned to differences in chemical composition and, in addition, to variation in surface roughness (Papers 2).

Table 3.1 List of the different fibrillated nanofibers and the corresponding paper, including raw materials, their pretreatments, their codes, crystallinity index before and after fibrillation, their average widths measured from AFM, and their contact angles.

Involved papers	Raw material	Pretreatment	Sample code	CI _{pulp} (%)	CI _{nanofibers} (%)	Contact angle (°)	Width (nm)
Paper 1,4	Carrot residue	Alkali, chlorite bleaching	CARROT	76	77	68 ± 2	12 ± 8
	Brewer's spent grain	Alkali, chlorite bleaching	BSG	72	74	61 ± 3	24 ± 6
Paper 2	Wood	Bleached kraft	WOOD-KRAFT	82	80	62 ± 2	14 ± 6
	Wood	SIL	WOOD-SIL	87	86	60 ± 3	15 ± 8
	Wood	SIL, chlorite bleaching	WOOD-SIL-B	85	82	54 ± 2	12 ± 6
Paper 3	Brown seaweed stipe	Chlorite bleaching	SEAWEED	-	-	58 ± 1	7 ± 3
Other studies	Carrot residue	Alkali, chlorite bleaching	CARROT-PILOT	75	74	71 ± 3	10 ± 4
	Wood	Bleached kraft	WOOD-KRAFT-PILOT	85	86	63 ± 2	13 ± 5
	Rice straw	Neutral sulfite, xylanase	RICE STRAW-NS-XYL	61	64	64 ± 2	14 ± 7
	Banana rachis	Alkali, chlorite bleaching	BANANA	70	73	60 ± 2	14 ± 5
	Reed canary grass	Alkali, chlorite bleaching	RCG	80	75	65 ± 3	15 ± 7
	Fruit and vegetable residue	Alkali, chlorite bleaching	FVR	68	64	74 ± 4	12 ± 5

Atomic force microscopy (AFM) is a commonly used technique for studying the morphology of nanofibers. The AFM height images of the bio-based nanofibers are presented in Figure 3.5. From these height scans it is possible to measure the width of the nanofibers (Table 3.1), where the measured average widths show an overall narrow range of the various nanofibers.

Considering the size of the nanofibers in the final nanofiber gels, when inspected on this scale, it can be tentatively concluded that the different raw materials, pretreatments and initial scales, can be fibrillated into nanofiber with comparable dimensions. However, from Figure 3.5, the AFM height images of the nanofibers displayed larger and apparently intact structures. Furthermore, for AFM measurement, the field of view visualized is restricted and thus even larger structures are often overlooked, leading to a highly limited representative overview of the entire material (Kvien et al., 2005). Although a combination of microscopic techniques with image analysis can provide information on nanomaterial width (Kvien et al., 2005), it is more difficult to determine nanofiber length because the fibers are entangled and it is difficult to identify both ends of individual nanofibers (Henriksson et al., 2008). Furthermore, it is common that sample preparation in most microscopic techniques involves drying of the sample prior to characterization. Thus, the larger structures seen in all samples might represent nonfibrillated material or agglomerations of the nanofibers as a result of drying.

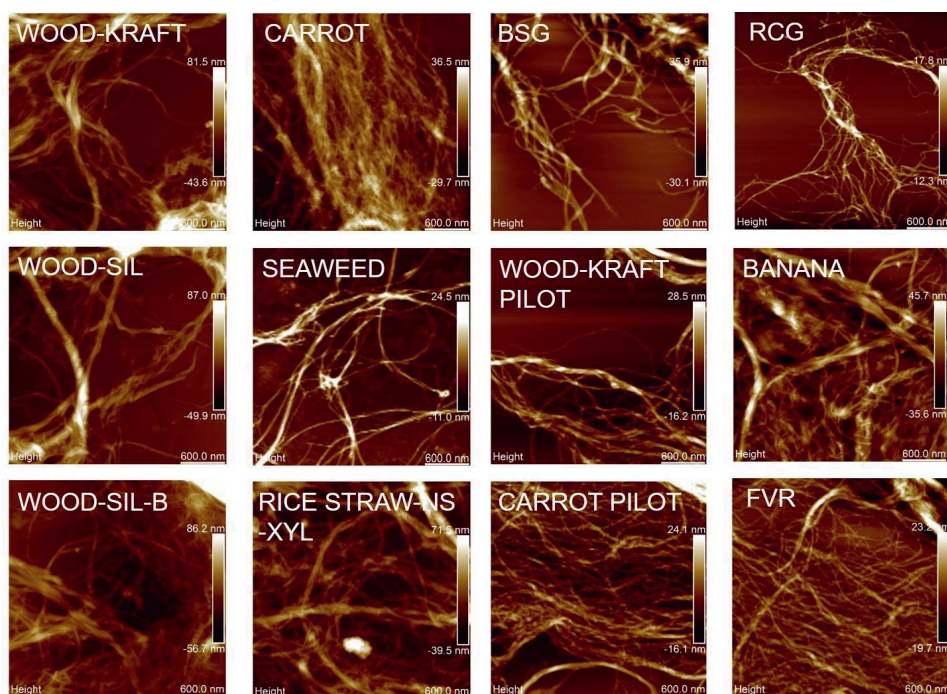


Figure 3.5 AFM height images of 12 bio-based nanofibers derived from different raw materials, pretreatments after fibrillation using ultrafine grinding (all in lab-scale grinder unless marked otherwise).

The mechanical properties of nanofiber networks are commonly used as an indirect measure of the efficiency of the separation process, where the smaller fiber size, without an extensive

length reduction (high aspect ratio), results in higher amounts of entanglements and contact points, in turn leading to stronger networks (Jonoobi et al., 2012). However, the preparation and tensile testing of the network also introduces several parameters to take into consideration when comparing values in different studies, such as drying and measurement procedures, and relative humidity, to mention a few (Österberg et al., 2013).

At a certain point during the fibrillation with ultrafine grinding, further processing does not result in further enhancement in mechanical properties of the network. A peak in network strength was observed during fibrillation, as discussed in section 3.1, along with a reached viscosity plateau for the different materials during fibrillation.

The materials of this work are summarized in Figure 3.6, showing the strength (a), elastic modulus (b), and viscosity (c) of the networks before fibrillation and the maximum value obtained during fibrillation. Furthermore, the relationship between the energy demand taken at the viscosity plateau and the energy demand at the maximum network strength is also presented in Figure 3.6 (d).

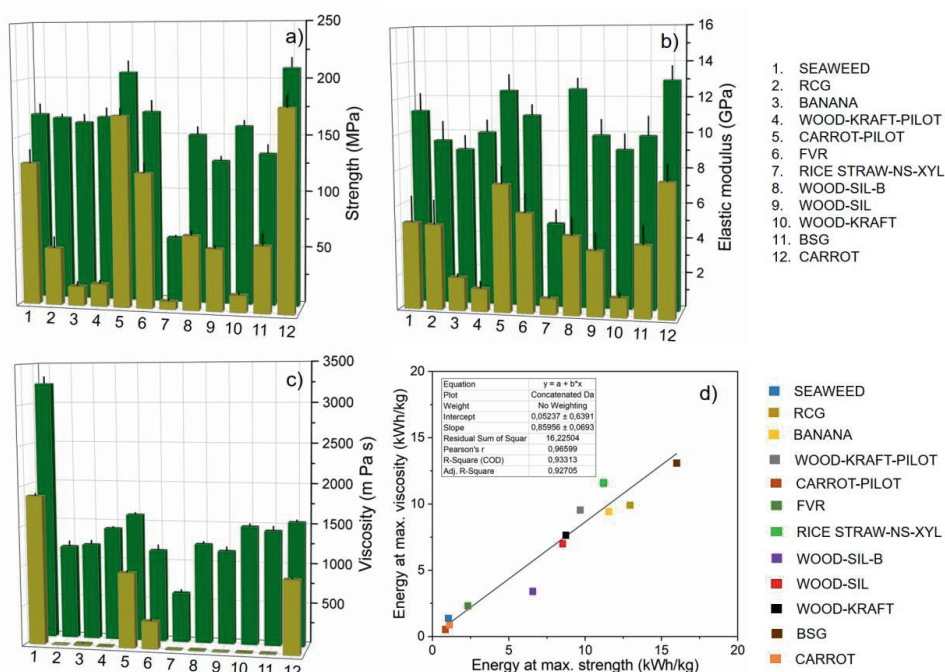


Figure 3.6 a) The strength, and b) elastic modulus of the pulp paper and the maximum value obtained during the fibrillation process. c) The viscosity measurements of the pulp and the maximum viscosity obtained during the fibrillation process for the different raw materials and pretreatments. All materials, where no specific pretreatments are denoted refer to alkali and chlorite bleached pulps. d) The energy demand at the maximum viscosity as a function of the energy measured at the maximum strength.

From Figure 3.6 (a,b), fibrillation to nanosized fibers had positive impact on strength and modulus of all materials. This behavior was also observed for the viscosity of all fibrillated pulps, as discussed in previous sections. The behavior of increased viscosity with the fibrillation process has been described in an earlier study by Lahtinen et al., (2014). Furthermore, a strong gel formation by disintegrated fibrils is typical of high aspect nanofibers (Pääkkö et al., 2007). The increase in fiber network connectivity upon separation into nanofibers has been shown to affect the mechanical properties of nanopapers, particularly their elastic modulus (Kulachenko et al. 2012), while the high aspect ratio is advantageous and contributes to the high strength of the fibrillated network structures. For the rice straw nanofibers, the high lignin content may explain the overall lower values (Figure 3.6 a,b,c) that constitute a barrier that reduces the fiber connectivity (Shao and Li 2007). Notable is the overall higher viscosity and mechanical properties of the carrot residue (lab and pilot), fruit and vegetable residue (FVR), and seaweed stipe before fibrillation, compared to the other materials. This implies a strong network formation already after pretreatment both in wet and dry state.

In Figure 3.6 (d) the relationship between the energy measured at the maximum viscosity and at the maximum strength of the nanofiber network is summarized for the different raw materials and pretreatments fibrillated to nanosize. The most efficient processing was observed for raw material sources such as carrot residue both in lab and pilot scale, seaweed stipe, followed by FVR with their inherent thin cell wall structures. This is in agreement with the initial high viscosity and mechanical values of partially separated fibers already after pretreatment, requiring less effort to fibrillate to nanosize. A cluster of a wide range of materials such as wood and agricultural residues is seen around 10 kWh/kg of energy consumed, yet SIL-combined bleaching provided a more efficient fibrillation of wood, thus lowering the energy demand. BSG was the most energy intense material to fibrillate. The linear relationship is close to being directly proportional (Figure 3.6 d), i.e., that energy at max viscosity, $J_{\mu_{max}}$, equals the energy at max strength, $J_{\sigma_{max}}$, which would mean that the ability of network formation measured in wet state represented by the maximum viscosity value is strongly correlated to the strength of the network in dry state. Thus, the equation of the linear least squares fit,

$$J_{\sigma_{max}} = 0.9 J_{\mu_{max}} + 0.1 \quad (\text{Eq. 5})$$

can be used to predict the energy necessary to reach the maximum network strength from online viscosity measurements of nanofiber suspensions, using ultrafine grinding and at the given processing parameters. In a larger perspective it would enable processing with significantly less energy demand, presenting a more environmentally friendly option for the processing routes in order to promote industrial production of nanofibers and their subsequent use for functional biomaterials, where the material depends on a strong network formation.

In summary, the bio-based nanofibers produced by ultrafine grinding can be monitored for a consistent quality output for a wide range of raw material sources and pretreatments using online viscosity measurements for both lab and pilot scale. Furthermore, production using

ultrafine grinding does not affect the inherent structure upon fibrillation with maintained crystallinity index after the process. Nanofibers between 10 and 24 nm are fibrillated from the different materials, with hydrophilic behavior and strong network formation, in wet and dried state, respectively. These properties could be advantageous in the preparation of membranes and/or hydrogels for various applications.

3.4 ADDED-VALUE BIOMATERIALS FROM MECHANICALLY FIBRILLATED BIO-RESIDUES

In this section three-dimensional (3D) hydrogels based on lignin-containing arabinoxylan (AX) and nanofibers were prepared, both from barley residues. Freeze-casted citric acid (CA) crosslinked hydrogels were formed using the lignin-containing AX, where water and nanofibers were used as a solvent and as reinforcing building blocks, respectively. The effects of nanofibers on the hydrogel properties were evaluated and summarized from Paper 4. The fibrillated nanofibers from seaweed stipe having a high alginate content were evaluated, as produced after fibrillation, as an ink. The ink was evaluated in terms of printability and shape fidelity by 3D printing discs, followed by crosslinking with CaCl_2 to form functional hydrogels that were further studied according to microstructural features (Paper 3).

Barley-residue-based functional biomaterial

The rehydration of the aerogels for the hydrogel formation and their degree of swelling was the initial assessment in terms of maintaining structural stability in contact with water, thus reflecting the crosslinking. The compression properties of the hydrogels as a function of their equilibrium swelling degree, representative stress and strain curves, and their SEM fracture surfaces along the freezing direction are shown in Figure 3.7.

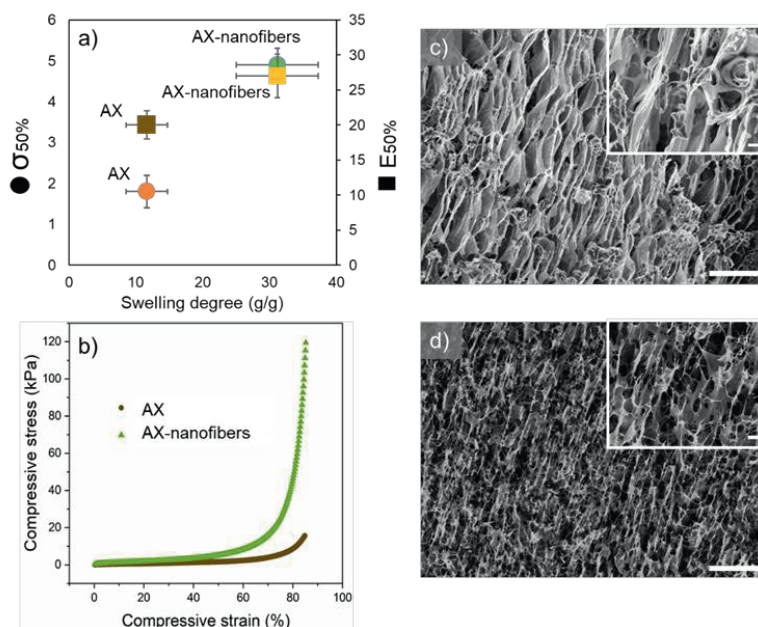


Figure 3.7 a) Compressive strength and modulus at 50% strain as a function of equilibrium swelling degree for CA content 5 wt%, b) representative stress and strain curves, SEM fracture surfaces along the freezing direction for c) AX, and d) AX with the addition of nanofibers. Scale bar: 100 μm . Scale bar, inset: 10 μm . Adapted from Paper 4.

Both samples appeared to have been successfully crosslinked after the heat-activated crosslinking reaction at 5 wt%, thus maintaining their structural integrity in water (Paper 4). The AX hydrogels displayed a more than 50% increase in the degree of swelling with the addition of nanofibers, as well as a moderate increase in compressive strength and modulus when compared at 50% strain (Figure 3.7a). At higher strain a more significant increase was apparent, as shown in Figure 3.7(b). From Figure 3.7(c), an oriented, channel-like structure dominates the inner architecture of the AX sample owing to the initial liquid-nitrogen freezing process, where ice crystals are formed and grow in the direction parallel to the temperature gradient. The formation of a network structure with open interconnected pores was promoted when the nanofibers were introduced as a component; this possibly contributed to the improved absorption ability of the sample. However, the crystal growth direction appeared to have been impeded by the introduction of nanofibers; thus, a less oriented structure is displayed in comparison to that of AX (Figure 3.7 c,d).

The hydrophobic nature of lignin, compared to cellulose is likely an influential factor on hydrogel behavior acting to reduce the swelling (Figure 3a). The introduction of nanofibers is favored by its inherent characteristics, the hydrophilic behavior and reinforcement of the AX structure, through a network formation, thus promoting an effective usage of sustainable resources obtained from inexpensive underutilized barley residues.

Seaweed-stipe-based functional biomaterial

To evaluate the fibrillated brown seaweed stipe as an ink its suitability was studied in terms of its rheological behavior, crosslinking, printability and shape fidelity by 3D printing discs, followed by crosslinking with CaCl_2 to form functional hydrogels, as shown in Figure 3.8.

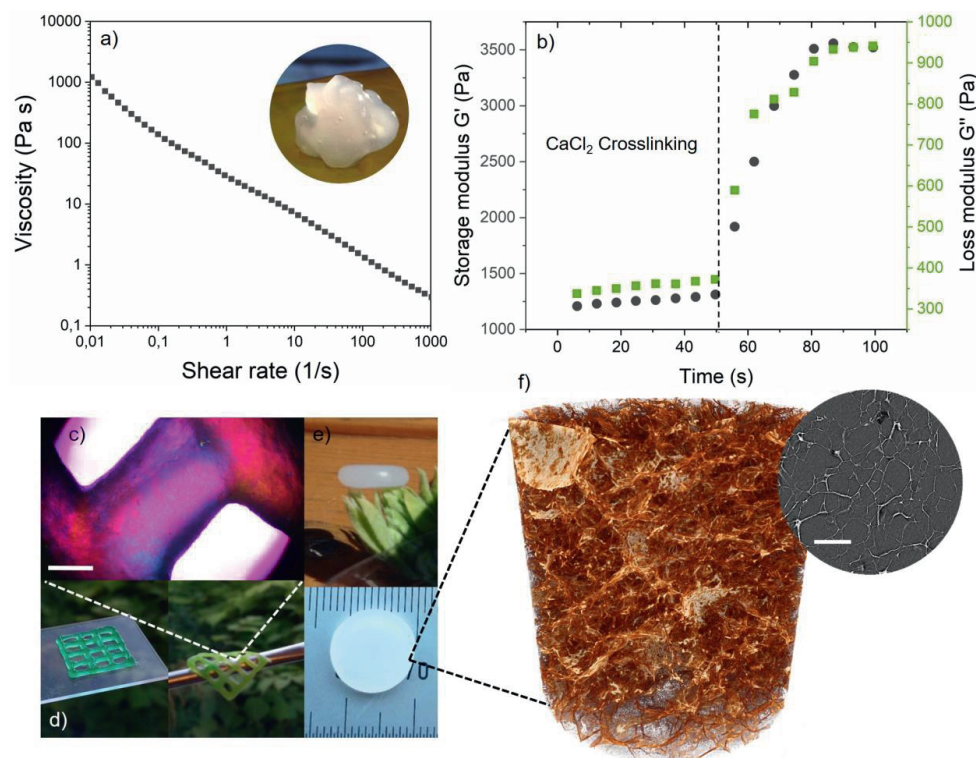


Figure 3.8 a) Flow curves of the ink at 2 wt.% (inset photograph of the gel), b) storage modulus G' , and loss modulus G'' measured over time where the CaCl_2 solution was added 50s after the measurement was started, c) OM image of grid after printing, scale bar: 500 μm , d) Photographs of the printed grid, before (to the left) and after crosslinking (to the right), e) Photographs of the 3D printed disc after crosslinking, and f) x-ray micro tomography of the disc after freeze drying, scale bar: 100 μm .

From Figure 3.8(a) a shear-thinning behavior was observed, comparable to previously reported behavior of commercial alginate mixed with nanofibers (Abouzeid et al., 2018), as well as nanofibers alone (Markstedt et al., 2015). The high viscosity at low shear rates and the shear thinning behavior with increasing shear rates provides shape fidelity during printing; however, to maintain the structural integrity after printing, crosslinking of the alginate is required. Hence, the gelling behavior of the hybrid-ink was studied by measuring the loss- and storage modulus as a function of time while crosslinking with CaCl_2 (Figure 3.8 b). Both the storage modulus d) and loss modulus e) displayed an instant increase upon addition of CaCl_2 solution at 50 s, and become gradually linear after a further 50 s.

As a proof of concept and to study the printing, shape fidelity and crosslinked structures, the ink was 3D printed, as fibrillated at 2 wt.% into a grid structure and discs, followed by CaCl_2 crosslinking. The grid displayed somewhat rounded corners after crosslinking, and the shape fidelity could likely be further improved by optimizing the solid content and printing parameters further. Still, 3D discs were successfully printed (Figure 3.8 e), displaying an interconnected network architecture upon freeze drying (Figure 3.8 f). 3D-printability and crosslinking enables the use of inks in a wide range of applications such as wound dressing (Leppiniemi et al., 2017), or even 3D-printing for tissue engineering (Markstedt et al., 2015), where the crosslinking ability of alginate with the shear thinning behavior of nanofibers from seaweed stipe was combined in the formulated ink to form a functional biomaterial.

Chapter 4

Conclusion and future work

With this work several different types of bio-based nanofibers from different sources and with varying energy input and pretreatments have been produced through mechanical fibrillation. This has resulted in a platform for mechanically fibrillated nanofibers and their overall characteristics. The implication is that several factors need to be considered, including the energy consumption, quality and intended function for a competitive production.

The main conclusions from this work are listed below:

- The choice of raw material is decisive for the efficiency of fibrillation process of nanofibers, where the bio-residues with a thin cell wall structure can be disintegrated with less energy.
- SIL pretreatment could be an alternative approach to the commercially bleached pulp, with a demonstrated effective delignification, while preserving the hemicellulose, in turn promoting efficient fibrillation, and is suitable for applications where color is not of importance.
- Online viscosity measurements can be used to monitor the mechanical fibrillation process for a consistent quality output with a high aspect ratio for a wide range of raw material sources and pretreatments at lab and pilot scale. It is furthermore useful to predict the energy necessary to reach the maximum network toughness when using ultrafine grinding and at the given processing parameters.
- Mechanically fibrillated nanofibers derived from bio-residues, and processed to their viscosity plateau, can be used for value-added biomaterials with enhanced functional behavior in terms of mechanical properties, swelling, processability and favorable network structure.

Although promising results were obtained, it would be of interest to adapt the use of online viscosity measurements further by evaluating the functional properties of different raw materials and degrees of fibrillation in the preparation of biomaterials. This would provide a better understanding of how nanofibers from different raw materials actually perform in applications and help to identify how bio-based resources should be processed, depending on their function in specific applications. It would be highly interesting to look even closer at the fibrillation of the raw materials that were promising from an energy efficient point of view and further develop their processing and their use in functional biomaterials.

References

- Abouzeid R.E., Khiari R., Beneventi D., Dufresne A., **2018**. Biomimetic mineralization of three-dimensional printed alginate/TEMPO-oxidized cellulose nanofibril scaffolds for bone tissue engineering. *Biomacromolecules*, 19(11), 4442-4452.
- Alakalhunmaa S., Parikka K., Penttilä P.A., Cuberes M.T., Willför S., Salmén L., Mikkonen K.S. **2016**. Softwood-based sponge gels. *Cellulose*, 23, 3221-3238.
- Alemdar A., Sain M., **2008**. Isolation and characterization of nanofibers from agricultural residues: wheat straw and soy hulls. *Bioresour Technol.*, 99(6), 1664-1671.
- Anugwom I., Mäki-Arvela P., Virtanen P., Damlin P., Sjöholm R., Mikkola J.P., **2011**. Switchable ionic liquids (SILs) based on glycerol and acid gases. *RSC Adv.*, 1, 452-457.
- Anugwom I., Eta, V., Mäki-Arvela P., Virtanen P., Hedenström M., Yibo M., Hummel M., Sixta H., Mikkola J.P., **2014**. Towards optimal selective fractionation for Nordic woody biomass using novel amine-organic superbase derived switchable ionic liquids (SILs). *Biomass Bioenergy*, 70, 373-381.
- Arvidsson R., Nguyen D., Svanström M., **2015**. Life cycle assessment of cellulose nanofibrils production by mechanical treatment and two different pretreatment processes. *Environ. Sci. Technol.*, 49, 6881-6890.
- Berglund L., Breedveld L., Oksman K., **2019**. Toward eco-efficient production of natural nanofibers from industrial residue: Eco-design and quality assessment. Submitted to *J. Cleaner prod.*
- Box J.M.F., **1983**. Product quality assessment by consumers — the role of product information. *Industrial Management & Data Systems*, 83 (3/4), 25-31.
- Brown R.C., **2003**. The biorenewable resource base, in: Singhanian, R., Brown, R.C. (Eds.), *Biorenewable resources engineering new products from agriculture*. Blackwell publishing company, Iowa, pp 60-61.
- Caló E., Khutoryanskiy V.V., **2015**. Biomedical applications of hydrogels: A review of patents and commercial products. *Eur. Polym. J.*, 65, 252-267.
- Cowie J., Bilek T., Wegner T.H., Shatkin J.A., **2014**. Market projections of cellulose nanomaterial-enabled products - part 2: Volume estimates, *Tappi J.*, 13 (5), 57-69.
- Delgado-Aguilar M., Tarrés Q., Pèlach M.À., Mutjé P., Fullana-i-Palmer P., **2015**. Are cellulose nanofibers a solution for a more circular economy of paper products? *Environ. Sci. Technol.*, 49, 12206-12213.
- ECS, **2014**. Bio-based products – Vocabulary, European standard EN 16575, European Committee for Standardization.

- Eriksen O., Syverud K., Gregersen O., **2008**. The use of microfibrillated cellulose produced from kraft pulp as strength enhancer in TMP paper. *Nord. Pulp Pap. Res. J.*, 23(3), 299–304.
- Gibson L.J., **2012**. The hierarchical structure and mechanics of plant materials review. *J. Royal Soc. Interface*, 9, 2749–2766.
- Gierer J., **1980**. Chemical aspects of kraft pulping. *Wood Sci. Technol.*, 14(4), 241–266.
- Gu F., Wang W., Cai Z., Xue F., Jin Y., Zhu J.Y., **2018**. Water retention value for characterizing fibrillation degree of cellulosic fibers at micro and nanometer scales. *Cellulose*, 25, 2861–2871.
- Hamad, W.Y., **2002**. Native cellulosic fibers: structure and composition in: Hamad W.Y. (Ed.), *Cellulosic materials: fibers, networks and composites*. Springer Science & Business Media, New York, pp 1-24.
- Hassan M., Berglund L., Hassan E., Abou-Zeid R., Oksman K., **2018**. Effect of xylanase pretreatment of rice straw unbleached soda and neutral sulfite pulps on isolation of nanofibers and their properties. *Cellulose*, 25(5), 2939-2953.
- Hassan M.L., Mathew A.P., Hassan E.A., El-Wakil N.A., Oksman K., **2010**. Nanofibers from bagasse and rice straw: process optimization and properties. *Wood Sci. Technol.*, 46, 193–205.
- Henriksson M., Berglund L.A., Isaksson P., Lindström T., Nishino T., **2008**. Cellulose nanopaper structures of high toughness. *Biomacromolecules*, 9, 1579-1585.
- Herrera N., Mathew A.P., Oksman K., **2015**. Plasticized polylactic acid/cellulose nanocomposites prepared using melt-extrusion and liquid feeding: Mechanical, thermal and optical properties. *Comp. Sci. Technol.*, 106, 149–155.
- Hiden A., Abe K., Yano H., **2014**. Preparation using pectinase and characterization of nanofibers from orange peel waste in juice factories. *J. Food Sci.*, 79, 1218–1224.
- Huppes G., Ishikawa M.A., **2005**. Framework for quantified eco-efficiency analysis. *J. Ind. Ecol.*, 9(4), 25–41.
- ICCT, **2013**. International Council on Clean Transportation: Availability of cellulosic residues and wastes in EU. https://www.theicct.org/sites/default/files/publications/ICCT_EUcellulosic-waste-residues_20131022.pdf (accessed September 2019).
- ISO, **2015**. <https://www.iso.org/obp/ui/#iso:std:iso:ts:80004:-1:ed-2:v1:en> (accessed September 2019)
- Isogai A., **2018**. Present situation and future prospects of nanocellulose R&D in Japan. TAPPI International Conference on Nanotechnology for Renewable Materials. 11-14 June, Madison, Wisconsin, USA.

- Iwamoto S., Abe K., Yano H., **2008**. The effect of hemicelluloses on wood pulp nanofibrillation and nanofiber network characteristics. *Biomacromolecules*, 9(3), 1022-1026.
- Jonoobi M., Mathew A.P., Oksman K., **2012**. Producing low-cost cellulose nanofiber from sludge as new source of raw materials. *Ind. Crops Prod.*, 40, 232–238.
- Klemm D., Heublein B., Fink H., Bohn A., **2005**. Cellulose: Fascinating biopolymer and sustainable raw material, *Angew. Chem. Int. Ed.*, 44(22), 3358–3393.
- Kulachenko A., Denoyelle T., Galland S., Lindström S.B., **2012**. Elastic properties of cellulose nanopaper. *Cellulose*, 19(3), 793-807.
- Lahtinen P., Liukkonen S., Pere J., Sneek A., Kangas H., **2014**. A comparative study of fibrillated fibres from different mechanical and chemical pulps. *Biores.*, 9, 2115-2127.
- Lee K.Y., Aitomäki Y., Berglund L.A., Oksman K., Bismarck A., **2014**. On the use of nanocellulose as reinforcement in polymer matrix composites. *Compos. Sci. Technol.* 105, 15–27.
- Leppiniemi J., Lahtinen P., Paajanen A., Mahlberg R., Metsä-Kortelainen S., Pinomaa T., Pajari H., Vikholm-Lundin I., Pursula P., Hytönen V.P., **2017**. 3D-printable bioactivated nanocellulose–alginate hydrogels. *ACS Appl Mater Interfaces*, 9(26), 21959-21970.
- Markstedt K., Mantas A., Tournier I., Martínez Ávila H., Hägg D., Gatenholm, P., **2015**. 3D bioprinting human chondrocytes with nanocellulose–alginate bioink for cartilage tissue engineering applications. *Biomacromolecules*, 16, 1489– 1496.
- McHugh D. J., **2003** A guide to seaweed industry. FAO Fisheries and Aquaculture Department, Rome.
- Moser C., Lindström M.E., Henriksson G., **2015**. Toward industrially feasible methods for following the process of manufacturing cellulose nanofibers, *BioRes.*, 10(2), 2360-2375.
- Nair S.S., Zhu J.Y., Deng Y., Ragauskas A.J., **2014**. Characterization of cellulose nanofibrillation by micro grinding. *J. Nanopart. Res.*, 16, 2349–2359.
- NRCAN, **2019**. <https://www.nrcan.gc.ca/our-natural-resources/domestic-international-markets/current-lumber-pulp-panel-prices/13309#pulp> (accessed September 2019)
- Peteiro, C., **2017**. Alginates and their biomedical applications, Rehm, B.; Moradali, M. (Eds.), *Springer Series in Biomaterials Science and Engineering Vol 11*; Springer, Singapore, pp 27-58.
- Pääkkö M., Ankerfors M., Kosonen H., Nykänen A., Ahola S., Österberg M., Ruokolainen J., Laine J., Larsson P.T., Ikkala O., Lindström T., **2007**. Enzymatic hydrolysis combined with mechanical shearing and high-pressure homogenization for nanoscale cellulose fibrils and strong gels. *Biomacromolecules*, 8(6), 1934-1941.

- Raj P., Mayahi A., Lahtinen P., Varanasi S., Garnier G., Martin D., Batchelor W., **2016**. Gel point as a measure of cellulose nanofibre quality and feedstock development with mechanical energy. *Cellulose*, 23, 3051–3064.
- Saito T., Kimura S., Nishiyama Y., Isogai A., **2007**. Cellulose nanofibers prepared by TEMPO-mediated oxidation of native cellulose. *Biomacromolecules*, 8(8), 2485-2491.
- Schniewind A.P., Cahn R.W., Bever M.B., (Eds.), **1989**. Wood and wood-based materials - Concise Encyclopedia. Pergamon Press Plc, Headington Hill Hall, Oxford, England.
- Segal L., Creely J.J., Martin A.E., Conrad C.M., **1959**. An empirical method for estimating the degree of crystallinity of native cellulose using the X-Ray diffractometer. *Text. Res. J.*, 29, 786–794.
- Shao Z., Li K., **2007**. The effect of fiber surface lignin on inter fiber bonding. *J. Wood Chem. Technol.*, 26, 231–244.
- Sharma A., Thakur M., Bhattacharya M., Mandal T., Goswami S., **2019**. Commercial application of cellulose nano-composites – A review. *Biotechnology Reports*, 21, 1-15.
- Shatkin J. A., Wegner T. H., Bilek T., Cowie J., **2014**. Market projections of cellulose nanomaterial-enabled products - part 1: Applications. *Tappi J.*, 13(5), 9–16.
- Sipponen M.H., Lange H., Crestini C., Henn A., Österberg M., **2019**. Lignin for nano- and microscaled carrier systems: applications, trends, and challenges. *ChemSusChem.*, 12, 2039-2054.
- Siqueira G., Oksman K., Tadokoro S.K., Mathew A.P., **2016**. Re-dispersible carrot nanofibers with high mechanical properties and reinforcing capacity for use in composite materials. *Compos. Sci. Technol.*, 123, 49–56.
- Siqueira P., Siqueira É., de Lima A. E., Siqueira G., Pinzón-Garcia A.D., Lopes A.P., Cortés Segura M.E., Isaac A., Vargas Pereira F., Botaro V.R., **2019**. Three-dimensional stable alginate-nanocellulose gels for biomedical applications: towards tunable mechanical properties and cell growing. *Nanomaterials*, 9(1), 78-100.
- Sonneveld E.J., Visser J.W., **1975**. Automatic collection of powder data from photographs. *J. Appl. Crystallogr.*, 8, 1–7.
- Spence K.L., Venditti R.A., Rojas O.J., Habibi Y., Pawlak J.J., **2011**. A comparative study of energy consumption and physical properties of microfibrillated cellulose produced by different processing methods. *Cellulose*, 18, 1097–1111.
- Staffas L., Gustavsson M., McCormick K., **2013**. Strategies and policies for the bioeconomy and bio-based economy: an analysis of official national approaches. *Sustainability*, 5, 2751-2769.
- Taniguchi T., Okamura K., **1998**. New films produced from microfibrillated natural fibres. *Polym. Int.*, 47, 291-294.

- Turbak A.F., Snyder F.W., Sandberg K.R., **1983**. Microfibrillated cellulose, a new cellulose product: properties, uses, and commercial potential. *J. Appl. Polym. Sci. Appl. Polym. Symp.*, 37, 815-827.
- UN, **2019**. The Sustainable Development goals report 2019. <https://unstats.un.org/sdgs/report/2019/The-Sustainable-Development-Goals-Report-2019.pdf> (accessed September 2019).
- Wågberg L., Decher G., Norgren M., Lindström T., Ankerfors M., Axnäs K., **2008**. The build-up of polyelectrolyte multilayers of microfibrillated cellulose and cationic polyelectrolytes. *Langmuir*, 2008 24(3), 784-795.
- Österberg M., Vartiainen J., Lucenius J., Hippi U., Seppälä J., Serimaa R., Laine J. A., **2013**. Fast method to produce strong NFC films as a platform for barrier and functional materials. *ACS Appl. Mater. Interfaces*, 5, 4640-4647.
- Österberg M., Cranston E.D., **2014**. Special issue on nanocellulose – Editorial. *Nord. Pulp Pap. Res. J.*, 29(1), 4-5.

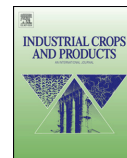
Appended publications

PAPER 1

Production potential of cellulose nanofibers from industrial residues:
efficiency and nanofiber characteristics

Berglund L., Noël M., Aitomäki Y., Öman T., Oksman K.

Indus. Crops. Prod., 92 (2016) 84-92.
<https://doi.org/10.1016/j.indcrop.2016.08.003>



Production potential of cellulose nanofibers from industrial residues: Efficiency and nanofiber characteristics



Linn Berglund, Maxime Noël, Yvonne Aitomäki, Tommy Öman, Kristiina Oksman*

Division of Materials Science, Luleå University of Technology, 97187, Luleå, Sweden

ARTICLE INFO

Article history:

Received 13 May 2016

Received in revised form 31 July 2016

Accepted 2 August 2016

Keywords:

Bio-residues

Cellulose nanofibers

Mechanical separation

Energy consumption

Nanofiber characteristics

ABSTRACT

The aim of this study was to evaluate the production potential of cellulose nanofibers from two different industrial bio-residues: wastes from the juice industry (carrot) and the beer brewing process (BSG). The mechanical separation of the cellulose nanofibers was by ultrafine grinding. X-ray diffraction (XRD) and Raman spectroscopy revealed that the materials were mechanically isolated without significantly affecting their crystallinity. The carrot residue was more easily bleached and consumed less energy during grinding, using only 0.9 kWh/kg compared to 21 kWh/kg for the BSG. The carrot residue also had a 10% higher yield than the BSG. Moreover, the dried nanofiber networks showed high mechanical properties, with an average modulus and strength of 12.9 GPa and 210 MPa, respectively, thus indicating a homogeneous nanosize distribution. The study showed that carrot residue has great potential for the industrial production of cellulose nanofibers due to its high quality, processing efficiency, and low raw material cost.

© 2016 Elsevier B.V. All rights reserved.

1. Introduction

From an environmental and economic perspective, it can be of great benefit to reuse industrial residues. The production of beverages on an industrial level leads to a considerable quantity of solid residues, mainly regarded as waste or low-value by-products, and the brewing industry alone generates approximately 21–26 billion kilos of spent grains annually. Brewer spent grains (BSG) are the most abundant brewing by-product, corresponding to approximately 85% of the total solid waste generated (FAO, 2003; EC, 2006). Numerous attempts at feasible uses for BSG have been investigated, but it still is regarded as a low-value by-product, despite being rich in cellulose, non-cellulosic polysaccharides and lignin (Mussatto et al., 2006).

The juice industry is another example where considerable quantities of residues can be found. Juice processing generates approximately 5.5 billion kilos of solid waste annually in European industries (Panouillé et al., 2007). Ideally, the amount of waste could be decreased by its use as a raw material for the production of materials with high value such as cellulose nanofibers thus increasing the value of the crops.

Cellulose nanofibers have been isolated from various types of industrial residues, for example, bagasse (Hassan et al., 2010), pineapple leaves (Cherian et al., 2011), mandarin peel (Hiasa et al., 2014), orange peel (Hideno et al., 2014), and carrot (Siqueira et al., 2016). Although the isolation of cellulose nanofibers has been carried out by different means from residues, there are very few reports focusing on the energy consumption and process efficiency of the separation process of these cellulosic material sources.

Cellulose nanofibers can be separated through mechanical treatment such as high-pressure homogenization (Henriksson et al., 2007; Jonoobi et al., 2010; Spence et al., 2011) or ultrafine grinding (Iwamoto et al., 2008; Spence et al., 2011; Jonoobi et al., 2012). Mechanical separation as a production process is, however, associated with high-energy consumption, as demonstrated by Spence et al. (2011). The same study concluded that ultrafine grinding is the most efficient approach in terms of consumed energy. Pretreatments such as enzymatic treatment (Henriksson et al., 2007) and TEMPO oxidation (Isogai et al., 2011) are efficient ways to reduce the energy demand. The drawback of both these pre-treatments is their relatively high cost. In addition, shortened fiber length due to degradation of the fibers during TEMPO oxidation has been reported (Hassan et al., 2015), as has a decrease in their thermal stability following this pretreatment (Fukuzumi et al., 2009).

For industrial production and utilization of nanofibers, as, for example, reinforcements in polymer composites (Lee et al., 2014), an economical as well as energy-efficient production is required.

* Corresponding author.

E-mail address: kristiina.oksman@ltu.se (K. Oksman).

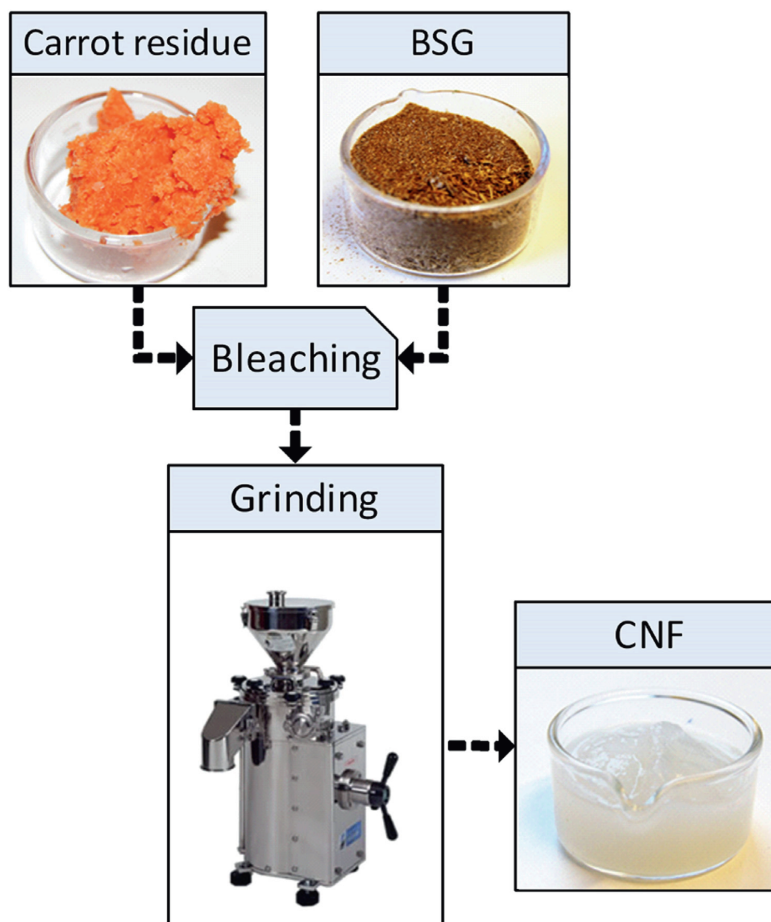


Fig. 1. Schematic of the separation process of the cellulose nanofibers from the two different residues.

The ease of separation of nanocellulose and yield of the process are dependent on the cell wall structure and composition and, hence, the raw material source (Jonoobi et al., 2014).

Cellulose nanofibrils found in the cell walls of plants are embedded in a matrix of hemicellulose, lignin and pectin. The geometrical structure of plant cells varies from the mostly honeycomb-like cells of wood to the foam-like thin parenchyma cells found in fruits and vegetables (Gibson, 2012). The thin parenchyma cell walls are believed to facilitate the separation of nanofibers (Jonoobi et al., 2014; Siqueira et al., 2016). The role of hemicelluloses in the separation of cellulose nanofibers has shown to be beneficial, and features such as decreased hornification and higher mechanical strength have been observed (Arola et al., 2013; Iwamoto et al., 2008). Siqueira et al. (2016) showed that carrot nanofibers were redispersed after drying, likely due in part to the presence of pectin (Siqueira et al., 2016). Pectin's influence on the fibrillation process is, however, less understood, though it has been suggested that both pectin and hemicellulose should be reduced to a certain extent to enable the separation of the nanofibrils (Hideno et al., 2014; Hiasa et al., 2014).

Jonoobi et al. (2012) showed the importance of a raw material source and processing parameters for the process efficiency of nanofibers using ultrafine grinding. In their study, less than 2 kWh/kg was used to produce nanofibers from sludge – a low-value or waste residue from special pulp production. The use of residues as raw material sources for cellulose nanofiber production is not only beneficial for reducing industrial waste but could also lead the way towards more energy-efficient processes for nanocellulose production, hence making it more commercially competitive.

The main goal of this study was to evaluate the production potential of cellulose nanofibers from two different industrial residues using a mild pretreatment and ultrafine grinding. The process is evaluated in terms of yield, energy efficiency and output quality, and thus, the potential for scaling up is assessed. To study the effect of the raw material source on the fibrillation process, measurements of the viscosity and microstructure were performed during the grinding process. The mechanical properties of the dried fiber networks were used as an indirect measurement of the degree of separation. In addition, the morphology was studied using SEM

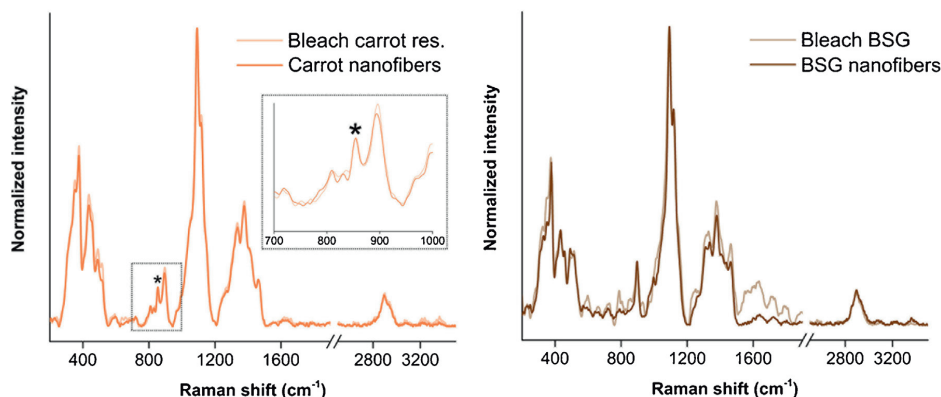


Fig. 2. Raman spectra of bleached carrot residue and its nanofibers (left) and bleached BSG and its nanofibers (right), showing the structural differences between them. The range between 1900 and 2600 cm^{-1} , where no peaks of materials of interest can be observed, is omitted for clarity. The asterisk in the carrot spectra indicates the peak from pectin.

and AFM and the crystallinity with both XRD and Raman spectroscopy.

2. Materials and methods

2.1. Raw materials

Both raw materials are residues with low values for energy recovery and the food industry. The carrot (*Daucus carota*) residue was supplied by Bråmhults Juice AB, (Sweden), and is a by-product from carrot juice production. The residue from beer production (BSG; full malt) was obtained from a large Finnish brewery. The BSG is mainly the residue of barley (*Hordeum vulgare*) after the malting and brewing process. A commercial bleached birch pulp provided by SCA Munksund AB (Sweden) was used as reference to the residues for evaluation of the production potential, using equivalent processing conditions. A schematic diagram of the process going from a raw material to cellulose nanofibers (CNF) is shown in Fig. 1.

2.2. Bleaching

Carrot residue and BSG were purified following the procedure described elsewhere by Siqueira et al. (2016) and briefly reported here. The residues were first washed with distilled water at 85 °C. Thereafter, the pulp was treated with an alkali (2% NaOH) solution at 80 °C for 2 h. This low concentration of NaOH is expected to decrease the hemicellulose concentration but not remove it. To remove lignin, both materials were bleached with NaClO_2 (1.7%) in an acetic buffer (pH 4.5) 80 °C for 2 h. For the carrot, bleaching resulted in a white pulp, while it was necessary to perform the bleaching procedure three times for the BSG. After bleaching, the materials were washed until a neutral pH was reached. The solid recoveries were calculated as yields according to the following equation:

$$\text{Yield\%} = W_1/W_0 \times 100 \quad (1)$$

where W_1 indicates the dry weight of the sample after the chemical treatment and W_0 indicates the initial dry weight of the residue.

2.3. Ultrafine grinding

Bleached pulps from the carrot residue and BSG were ground using a super mass colloid MKCA6-3, Masuko Sangyo, (Japan). Both suspensions were ground at a consistency of 1.5%. Prior to the grinding, the suspensions were dispersed using a shear mixer, Silverson L4RT Silverson Machine Ltd. (England). The grinding was operated in the contact mode immediately after initial feeding of the suspension, and the rotor speed was set to 1500 rpm. The gap between the stones was gradually adjusted to 70 μm (negative). The grinding stones used were coarse silicon carbide (SiC), which are non-porous standard stones for soft materials. The bleached carrot residue was processed over 20 min, and the processing time for the BSG was 170 min. The energy consumption for the mechanical separation was based on the direct measurement of power, using a power meter, Carlo Gavazzi, EM24 DIN (Italy) and the processing time. The energy demand was calculated from

$$\text{Energy} = \text{power (W)} \times \text{time (h)} \quad (2)$$

The energy consumption for the grinding process is expressed as kWh per kg of the nanofibers dry weight. To assess the grinding process, samples of the suspension were characterized through viscosity measurements and an optical microscope, taken at regular intervals of the grinding process. The grinding process was terminated when a plateau in viscosity was reached and no larger structures could be detected by polarized microscopy.

2.4. Characterization

The chemical compositions of both raw materials were determined following a procedure published by Moubasher et al. (1982). In brief, the procedure was as follows: 2 g of each raw material was boiled in ethanol for 15 min, and this was repeated four times. The materials were then washed with distilled water and kept in the oven overnight (80 °C) to dry. Dry materials were weighed and divided into two equal parts in which one part was considered fraction A. The second part of the residues was treated with 24% KOH for 4 h at 25 °C. After that, it was washed thoroughly with distilled water and dried at 80 °C overnight. The dry weight was taken as fraction B. The same sample was treated with 72% H_2SO_4 for 3 h (to hydrolyze the cellulose) and then refluxed in H_2SO_4 (5%) for 2 h. It was washed with distilled water and dried at 80 °C in the oven overnight. The dry weight was taken as fraction C. The cellulose

Table 1

Yield calculations of carrot residue and BSG after each step of the chemical pre-treatment process.

Materials	Residue (starting weight) [g]	Washed [g]	Weight after alkali treatment [g]	Weight after bleaching [g]	Total yield [%]
Carrot residue	100	79	52	32	32
BSG	100	85	45	22	22

Table 2

The chemical composition of the carrot and BSG residues displayed before and after the pretreatment. The crystallinity indexes of the bleached residues and nanofibers using XRD and Raman methods are displayed in the last two columns.

Materials	Cellulose (%)	Hemicellulose (%)	Lignin (%)	CI _{XRD} (%)	CI _{Raman} (%)
Carrot residue	45	26	11		
Carrot bleached	88	10	0.2	76	89
Carrot nanofibers				77	85
BSG	17	29	21		
BSG bleached	70	23	4.2	72	81
BSG nanofibers				74	82

content is the difference between B and C, the hemicellulose content is the difference between A and B, and the lignin content is C.

The microstructure was studied during the disintegration process to assess the degree of fibrillation using a polarizing microscope, Nikon Eclipse LV100N POL (Japan).

The measurement of viscosity was performed during the grinding process to assess the rheological behavior for the materials during fibrillation. The measurements were conducted using a Vibro Viscometer SV-10, A&D Company, Ltd. (Japan), at a constant shear rate. The velocity (shear rate) of the sensor plates keeps periodically circulating from zero to peak because sine-wave vibration is utilized, at a frequency of 30 Hz. The viscosity measurements were repeated at room temperature ($22.5 \pm 1.0^\circ\text{C}$) to validate the time of the start of the plateau because the viscosity measurements made during fibrillation were at a higher temperature as a result of the temperature increase generated by the compression and abrasive shearing forces during the process. The presented values are based on three measurements for each sample.

The crystallinity was measured with X-ray diffraction (XRD) using a PANalytical Empyrean X-ray diffractometer (The Netherlands) equipped with a PIXcel^{3D} detector and Cu K α radiation ($\lambda = 0.154\text{ nm}$). The X-ray generator was operated at 45 kV and 40 mA. The crystallinity index (CI) was calculated based on Segal et al. (1959), such that

$$\text{CI} = I_{002} - I_{\text{am}} / I_{002} \times 100. \quad (3)$$

where I_{002} is the intensity of the crystalline peak and I_{am} is the intensity of the amorphous peak. A baseline correction based on Sonneveld and Visser (1975) was used.

Raman spectroscopy measurements were performed on a Bruker Senterra Dispersive Raman microscope equipped with an Olympus 20 \times objective, Bruker Optik GmbH (Germany). Spectra were collected with a 785 nm laser at a power of 100 mW for 1 min with a resolution of 5 cm^{-1} . Several spots of sample were studied to ensure the reproducibility of the measurements and thus present typical spectra.

The morphologies of the carrot and BSG residues were studied before and after the isolation process using field emission scanning electron microscopy FE-SEM Merlin (Zeiss, Germany) at an acceleration voltage of 5 kV. The fibers were dried in acetone to reduce their tendency to aggregate and coated with gold to avoid charging. The nanofiber size distribution (width) was based on 100 measurements for each sample measured from the SEM images using SemAfore software.

Atomic Force Microscopy (AFM), Veeco Multimode Scanning Probe (USA), was used to further study the size distribution

of the separated nanofibers. The scanning was performed in tapping mode, and the samples were prepared with spin coating of nanofiber suspension on freshly cleaved mica plate. The nanofiber width/diameter were measured from height images using Nanoscope V software, and the average values and standard deviations presented are based on 40 different measurements.

The fiber networks were prepared for tensile testing taken after different processing times to give an indication of the degree of fibrillation. The suspension was adjusted to 0.2% consistency and dispersed with a shear mixer, IKA T25, UltraTurrax, IKA-Werke GmbH & Co. (Germany), at 10,000 rpm for 10 min. Degassing was carried out before the suspension was filtered using vacuum-assisted filtration with a membrane filter with a pore size of $0.45\text{ }\mu\text{m}$ and a glass filter support. The obtained wet cake was dried for approximately 12 h at room temperature followed by hot-pressing at 85°C , using Fortune presses, LP300, Fontijne Grotnes (The Netherlands), under 30 kPa for 40 min.

Mechanical properties of the networks were measured using a Shimadzu AG-X (Japan) universal testing machine using 1 kn load cell. The tests were conducted at an extension rate of 2 mm/min, and the gauge length was 20 mm. Prior to testing, the samples were conditioned at 50% RH and 23°C .

3. Results and discussion

Both residues were investigated as potential raw materials for cellulose nanofiber production. The calculated yield of the process from the residues is presented in Table 1.

The majority of the material loss was seen in the alkali and bleaching steps of the process, and the higher total yield observed for carrot residue of 32%, compared to the BSG yield of 22%, might be attributed to the repeated bleaching steps required for the BSG.

The yields of the residues are comparable to the reported yields of orange peel waste, which lie between 15 and 31% based on solid recoveries for various pre-treatments (Hideno et al., 2014).

The chemical composition before and after the pretreatment of the raw materials is presented in Table 2. The estimated crystallinity index using XRD and Raman is shown before and after the mechanical treatment in the table. The chemical composition showed a considerable amount of cellulose for carrot residue prior to the chemical treatment, with 45% compared to 17% for BSG.

Cellulose and hemicellulose constitute the greatest composition of the carrot residue; have been found to constitute between 52 and 92% on a dry weight basis (dietary fiber) in a previous study (Marlett, 1992). The same study reported a lignin content of 4%, whereas Nawirska and Kwasniewska (2005) have reported the composition of the dietary fiber constituents of carrot residue

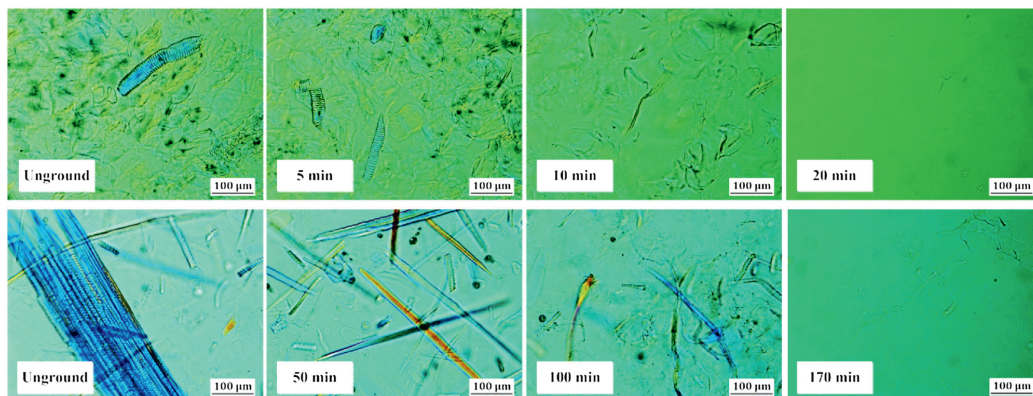


Fig. 3. Polarized microscopy images of the carrot (above) and BSG (below) residues. Size and structural changes taken at different time intervals during the grinding process.

as pectin at approximately 4%, hemicellulose at 12%, cellulose at 52% and lignin as high as 32%. For BSG, the reviewed values range between 16 and 25% cellulose, 28 and 35% hemicellulose, and 7 and 28% lignin based on brewery waste analyzed from dry matter (Aliyu and Bala, 2011).

The reported values in the literature vary considerably with regard to fiber values, likely as a result of different methods of fiber analysis (Marlett, 1992). Additionally, the harvesting and the different industrial processing conditions likely contribute to the variety found. The hemicellulose content was slightly reduced by the mild sodium hydroxide treatment, and the lignin content was considerably decreased after bleaching.

XRD measurements were made to evaluate the effect of the mechanical treatment on the crystallinity of the materials. As expected, a typical cellulose I appearance was observed for both materials in the XRD spectra (not reported here) (Mondragon et al., 2014). The crystallinity index was calculated to be 76% for the bleached carrot residue and 77% for the carrot nanofibers. For BSG, calculated crystallinity indexes of 72% and 74% were obtained before and after the grinding, respectively. These results showed that the grinding appears to isolate the nanofibers without affecting their inherent structure. The crystallinity index was also determined from Raman spectra (Agarwal et al., 2010). The spectra for the materials are displayed in Fig. 2. The results were qualitatively in accordance with the indices calculated from the XRD spectra: for

the carrot, the crystallinity indexes were higher in value, with 89% before grinding and 85% after the process, while for the BSG residue, the indexes were found to be somewhat lower, at 81% and 82%, respectively. The Raman measurements also provided information about the structural differences between the two materials and the influence of grinding. Both the bleached carrot and BSG spectra displayed typical peaks for cellulose, i.e., at 1095 cm^{-1} in the range of $300\text{--}520\text{ cm}^{-1}$, at 1120 cm^{-1} in the range of $1260\text{--}1470\text{ cm}^{-1}$ and at 2897 cm^{-1} (Wiley and Atalla, 1987; Schenzel and Fischer, 2001). However, a feature from the cellulose that appeared differently is the peak at 1295 cm^{-1} , which had a significantly higher intensity in the bleached carrot spectrum than in the bleached BSG spectrum. The differences in peak intensities and ratios translate to differences in the structural properties of these materials. However, the main difference in the spectra between the two residues was a sharp peak with medium intensity at 860 cm^{-1} that can be seen only in the carrot sample and is characteristic for pectin (Mathlouthi and Koenig, 1986). This confirmed the presence of pectin after the pretreatment. The spectra of the samples after grinding were similar to those of the bleached samples, especially in the case of carrot, where almost no changes in the spectra can be seen. In the case of BSG, some slight alterations in the structure of cellulose can be presumed because changes in the intensity of the peaks associated with cellulose can be observed, especially between 1260 and 1470 cm^{-1} . An intensity difference was observed around 1600 cm^{-1} in the bleached BSG in comparison with the BSG nanofibers. This difference was attributed to background noise, appearing at a high level of intensity due to the weaker cellulose signal found in the bleached BSG compared to the BSG nanofibers. Thus, the ratio of cellulose to noise signals is lower for the bleached BSG in the normalized spectra.

Polarized micrographs of samples of the materials were taken at regular intervals during the grinding process, and selected intervals are shown in Fig. 3. These show the effect of grinding on the large micro-sized particles. The bleached carrot residue displayed micro-sized structures constituting mainly fragments of parenchyma cells, while the micro-sized structures in the bleached BSGs were mainly fibers. The disintegration occurred faster for the bleached carrot residue, and the absence of larger structures was seen already after 20 min of processing. After 50 min of fibrillation of bleached BSG, larger structures of various sizes are still observed, and a processing time of 170 min was required to separate these into the nanosize, rendering it a less-efficient process.

It was also seen that the viscosity of the cellulose suspensions increased continuously during the grinding process, as shown in

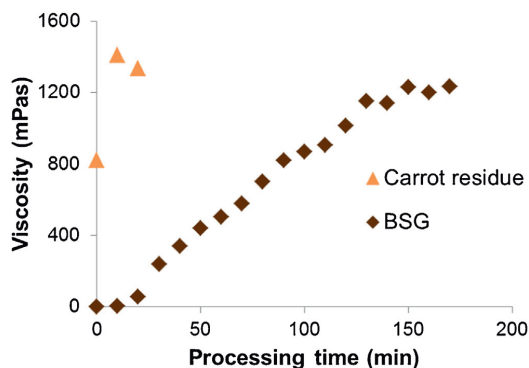


Fig. 4. The viscosity change as a function of the fibrillation process time for carrot and BSG residues.

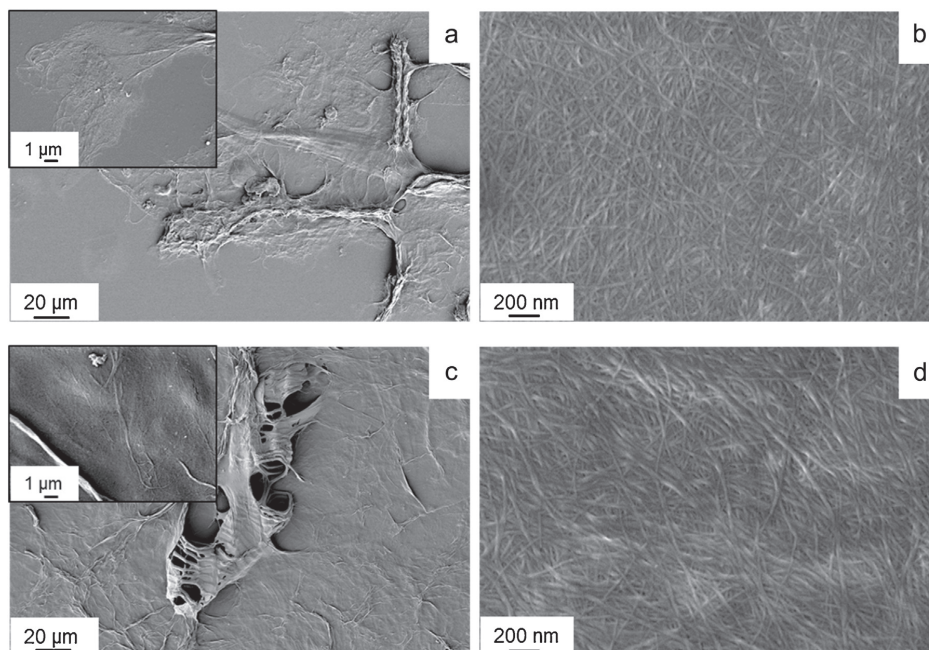


Fig. 5. Scanning electron microscopy images of the residues after bleaching and grinding of (a, b) carrot and (c, d) BSG.

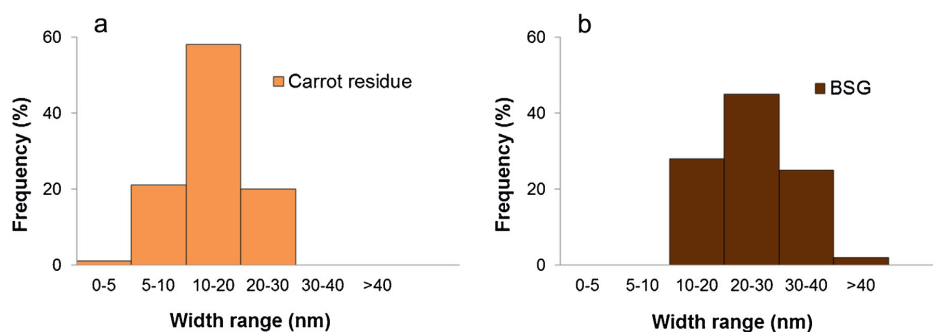


Fig. 6. Size distribution measured from SEM images for the widths of (a) carrot nanofibers and (b) BSG nanofibers.

Table 3

Mechanical properties of the fiber networks before and after the fibrillation process, the energy consumed during the grinding process, and the density of the networks.

Residue	E-modulus (GPa)	Strength (MPa)	Strain (%)	Energy (kWh/kg)	Density (kg/m ³)
Carrot bleached	7.6 ± 1.2	178 ± 11	6.9 ± 1.7	–	1.11 ± 0.03
Carrot nanofibers	12.9 ± 0.9	210 ± 9	6.0 ± 0.4	0.9	1.16 ± 0.04
BSG bleached	4.1 ± 1.1	59 ± 12	2.1 ± 0.2	–	1.10 ± 0.02
BSG nanofibers	9.9 ± 1.9	135 ± 8	5.1 ± 1.9	21	1.21 ± 0.03

Fig. 4. Measurements were performed with regular intervals with the intent to provide an assessment of the degree of separation, which is applicable as an online measurement. The disintegration process was carried out until a plateau in the viscosity was observed. The increased viscosity in the fibrillation process, connected to the disintegration of fibrils, is forming a stronger network, has been described in an earlier study by Lahtinen et al. (2014).

Prior to the grinding process, the initial viscosity of the bleached carrot residue was measured as 822 mPa. The highest viscosity of 1411 mPa was obtained after just 10 min of processing, showing a strong gel formation by disintegrated fibrils as is typical of nanocellulose (Gong et al., 2011). The plateau viscosity of BSG is similar at 1237 mPa, but the starting value was much lower and the time taken to reach this was much longer at 150 min. When comparing these viscosity values to commercial wood pulp, the viscosity

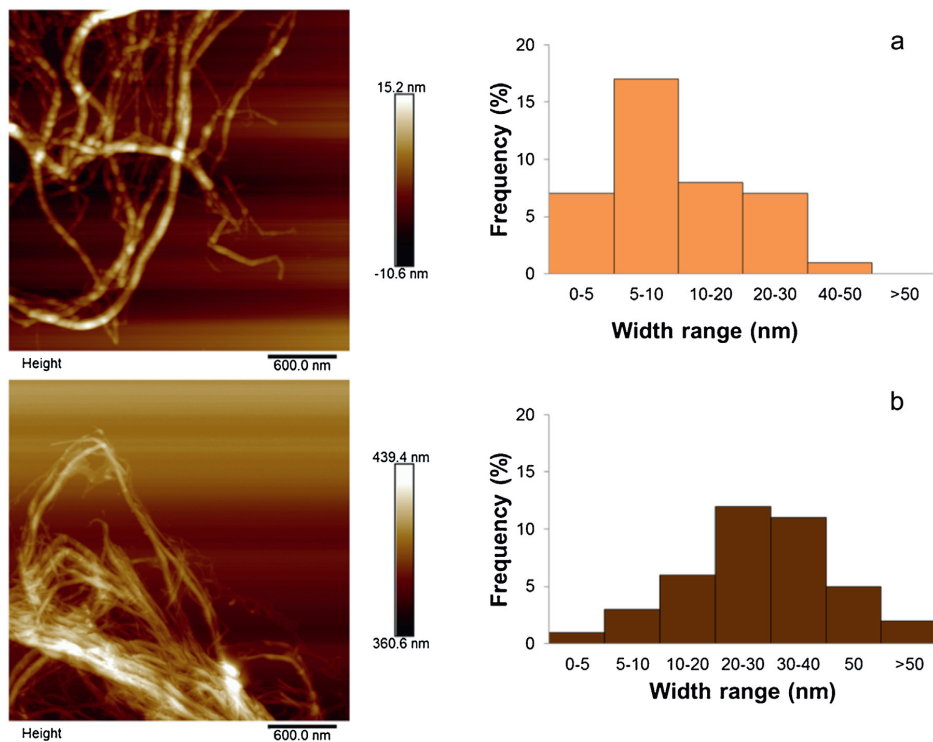


Fig. 7. AFM height images and size distributions of the nanofibers of (a) carrot residue and (b) BSG.

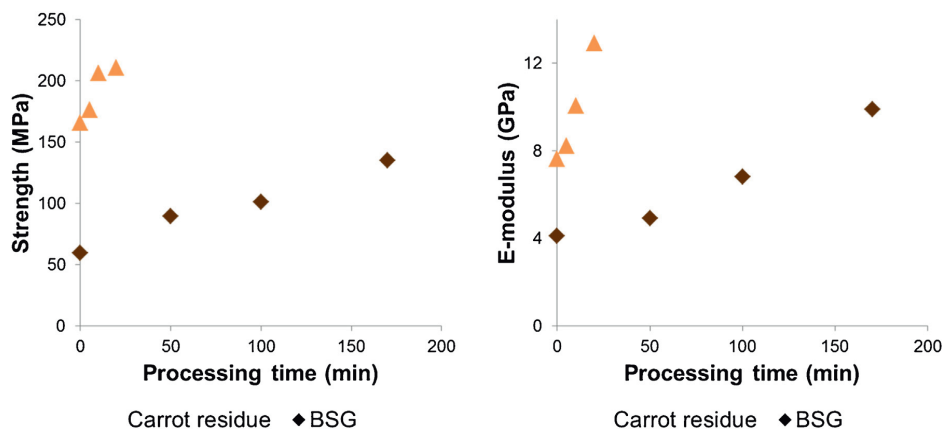


Fig. 8. Strength and stiffness of the fiber networks as a function of grinding processing time.

plateau at 1275 mPa is reached after 90 min grinding, showing that this is similar to the BSG material.

The morphology of the residues was investigated with SEM before and after the mechanical separation. Fig. 5 shows both residues in their bleached and ground states. Larger structures are observed for bleached residues, carrot (a) and BSG (c), with nanofibers primarily associated within the cell wall.

The higher magnification SEM images (b) and (d) show the separated nanofibers from carrot and BSG residues, respectively, after

the mechanical isolation. The width distribution measured from the SEM images after mechanical isolation is illustrated in Fig. 6.

The size distribution histogram of the isolated carrot nanofibers (a) showed that the majority of the nanofibers were measured in the range of 5–30 nm. For the BSG (b) the corresponding range lies between 10 and 40 nm. The size of the nanofibers was also measured from AFM height images and is shown together with their size distribution in Fig. 7. The width of the carrot nanofibers (a) was 12 ± 8 nm, and the BSG nanofibers (b) were more than twice

the size of carrot with a width of 30 ± 13 nm. The measured dimensions were in agreement with the values measured from the SEM images.

The mechanical properties of the fiber networks, their densities, and energy demand of the fibrillation process are summarized in Table 3.

Although many factors, such as the porosity, number of bonds, orientation, etc., affect the fiber network properties, the mechanical properties indicate the degree of fibrillation. The fiber network of the bleached carrot residue had strength of 178 MPa, which is high compared to the bleached BSG at 59 MPa. The modulus of the bleached carrot residue network is increased significantly with the grinding process from 7.6 to 12.9 GPa and the final strength was also very high at 210 MPa. Also a considerable increase in the mechanical properties was observed for BSG after the fibrillation process, the strength increased from 59 to 139 MPa and the modulus from 4.1 to 9.9 GPa. The maximum strain of the nanofiber networks was slightly decreased with the fibrillation for the carrot nanofibers but increased for the BSG network. However the carrot nanofiber network showed higher strain than the BSG network.

If comparing these mechanical properties to nanofibers from wood pulp, the carrot nanofiber properties are altogether higher. The modulus of wood nanofiber network is similar to that of the BSG (9.9 GPa) but with a better strength (174 MPa) and strain (6%).

These results, together with the initial high viscosity of the bleached carrot residue, indicated that the parenchyma cells of the carrot might be partially fibrillated already in the bleaching process, allowing greater interaction between these cells and hence forming a stronger network than that found in the more stable microfibrils of the bleached BSG.

The measured energy consumption was, remarkably lower for the fibrillation of carrot, 0.9 kWh/kg compared to that of the BSG 21 kWh/kg (see Table 3). The grinding of carrot to the nanofiber size is very energy efficient, the energy consumption of commercial wood pulp requires 13 kWh/kg in the similar grinding process. The process efficiency was also evaluated in terms of the strength and modulus of the networks as a function of the grinding time, as shown in Fig. 8. The increased strength and stiffness observed with the process time signified a more efficient separation of nanofibers from the bleached carrot residue, supporting the trends found in the viscosity during processing, where a peak was reached after only 10 min of grinding.

The efficient separation of bleached carrot residue into nanosized fibers can be attributed to the more accessible fiber in the inherently thin carrot cell wall. This shows that the structural differences of the cells, and hence the choice of raw material, has an important role for the efficient production of cellulose nanofibers. The remaining hemicellulose may have acted to facilitate the fibrillation. However, a higher amount of hemicellulose alone did not improve the process efficiency, as shown in the bleached BSG, where the disintegration is a more gradual process, at more than double the hemicellulose content compared to the bleached carrot residue. The presence of the remaining lignin could also have been a contributing factor to reduce the process efficiency for the separation of BSG.

It has been suggested that the removal of non-cellulosic polysaccharides such as pectin is important for the separation of nanofibers (Hideno et al., 2014). Nevertheless, in this study, the pectin, which is only found in the carrot residue, does not seem to negatively affect the nanofibrillation of carrot residue.

4. Conclusions

In this study, we demonstrate that two different residues, namely carrot and BSG, can be separated into nanofibers with only

a simple bleaching pretreatment prior to the mechanical separation. The nanosized fibers of the carrot residue were produced using only 0.9 kWh/kg, which is approximately 24 times lower than the 21 kWh/kg required to produce nanofibers from BSG and approximately 14 times lower than commercial wood pulp. An energy consumption of 0.9 kWh/kg for the carrot residue indicates that this type of residue has the potential for large-scale production of cellulose nanofibers.

The carrot nanofibers characterized with SEM and AFM showed separated nanofibers. The fibrillation using ultrafine grinding was accomplished without altering the inherent structure of the nanofibers. Furthermore, the carrot nanofiber network showed high mechanical properties, with a strength of 210 MPa and modulus of 13 GPa, indicating a high degree of separation.

For the BSG, the SEM and AFM also displayed nanosized fibers, yet the mechanical properties indicate that even after a 8-fold longer grinding time, a lower degree of fibrillation was obtained. The process efficiency is also high because the carrot residue needs only to be bleached once.

Thus, it can be concluded that the carrot residue from the juice industry has a great potential for the industrial production of cellulose nanofibers due to its high quality and processing efficiency combined with its low raw material cost.

Competing interests

The authors declare that they have no competing interests.

Acknowledgements

The authors gratefully acknowledge the financial support of the European Commission under INCOM EC FP7, Grant Agreement No: 608746. The authors are grateful for the technical support from Anders Dahlqvist at Bergius, as well as Alejandro Leiro at Luleå University of Technology for his assistance with high-resolution electron microscopy.

References

- Agarwal, U.P., Riner, R.S., Ralph, S.A., 2010. Cellulose I crystallinity determination using FT-Raman spectroscopy: univariate and multivariate methods. *Cellulose* 17, 721–733.
- Aliyu, S., Bala, M., 2011. Brewer's spent grain: a review of its potentials and applications. *Afr. J. Biotechnol.* 10, 324–331.
- Arola, S., Malho, J.M., Laaksonen, P., Lille, M., Linder, M.B., 2013. The role of hemicellulose in nanofibrillated cellulose networks. *Soft Matter* 9, 1319–1326.
- Cherian, B.M., Leão, A.L., de Souza, S.F., Costa, L.M.M., de Olyveira, G.M., Kottaisamy, M., Nagarajan, E.R., Thomas, S., 2011. Isolation of nanocellulose from pineapple leaf fibres by steam explosion. *Carbohydr. Polym.* 86, 1790–1798.
- European Commission, 2006. European Integrated Pollution Prevention and Control Bureau (EIPPCB). Reference document on best available techniques (BAT) in the food, drink and milk industries. EIPPCB, Seville.
- FAO, 2003. Food and agriculture organisation of the united nations, 2003. 2000–2002 world beer production. *BIOS Int.* 8, 47–50.
- Fukuzumi, H., Saito, T., Iwata, T., Kumamoto, Y., Isogai, A., 2009. Transparent and high gas barrier films of cellulose nanofibers prepared by TEMPO-mediated oxidation. *Biomacromolecules* 10, 162–165.
- Gibson, L.J., 2012. The hierarchical structure and mechanics of plant materials a review. *J. Royal Soc. Interface* 9, 2749–2766.
- Gong, G., Mathew, A.P., Oksman, K., 2011. Strong aqueous gels of cellulose nanofibers and nanowhiskers isolated from softwood flour. *Tappi J.* 10, 7–14.
- Hassan, M.L., Mathew, A.P., Hassan, E.A., El-Wakil, N.A., Oksman, K., 2010. Nanofibers from bagasse and rice straw: process optimization and properties. *Wood Sci. Technol.* 46, 193–205.
- Hassan, M.L., Bras, J., Mauret, E., Fadel, S.M., Hassan, E.A., El-wakil, N.A., 2015. Palm rachis microfibrillated cellulose and oxidized-microfibrillated cellulose for improving paper sheets properties of unbeaten softwood and bagasse pulps. *Ind. Crops Prod.* 64, 9–15.
- Henriksson, M., Henriksson, G., Berglund, L.A., Lindstrom, T., 2007. An environmentally friendly method for enzyme-assisted preparation of microfibrillated cellulose (MFC) nanofibers. *Eur. Polym. J.* 43, 3434–3441.
- Hiasa, S., Iwamoto, S., Endo, T., Edashige, Y., 2014. Isolation of cellulose nanofibrils from mandarin (*Citrus unshiu*) peel waste. *Ind. Crop. Prod.* 62, 280–285.

- Hideno, A., Abe, K., Yano, H., 2014. Preparation using pectinase and characterization of nanofibers from orange peel waste in juice factories. *J. Food Sci.* 79, 1218–1224.
- Isogai, A., Saito, T., Fukuzumi, H., 2011. TEMPO-oxidized cellulose nanofibers. *Nanoscale* 3, 71–85.
- Iwamoto, S., Abe, K., Yano, H., 2008. The effect of hemicelluloses on wood pulp nanofibrillation and nanofiber network characteristics. *Biomacromolecules* 9, 1022–1026.
- Jonoobi, M., Harun, J., Mathew, A., Hussein, M., Oksman, K., 2010. Preparation of cellulose nanofibers with hydrophobic surface characteristics. *Cellulose* 17, 299–307.
- Jonoobi, M., Mathew, A.P., Oksman, K., 2012. Producing low-cost cellulose nanofiber from sludge as new source of raw materials. *Ind. Crops Prod.* 40, 232–238.
- Jonoobi, M., Mathew, A.P., Oksman, K., 2014. Natural resources and residues for production of biomaterials. In: Oksman, K., Mathew, A.P., Bismarck, A., Rojas, O., Sain, M. (Eds.), *Handbook of green materials*, vol. 1. World Scientific Publishing Co. Pte. Ltd., Singapore, pp. 19–33.
- Lahtinen, P., Liukkonen, S., Pere, J., Sneek, A., Kangas, H., 2014. A comparative study of fibrillated fibers from different mechanical and chemical pulps. *Bioresources* 9, 2115–2127.
- Lee, K.-Y., Aitomäki, Y., Berglund, L.A., Oksman, K., Bismarck, A., 2014. On the use of nanocellulose as reinforcement in polymer matrix composites. *Compos. Sci. Technol.* 105, 15–27.
- Marlett, J.A., 1992. Content and composition of dietary fiber in 117 frequently consumed foods. *J. Am. Diet. Assoc.* 92, 175–186.
- Mathlouthi, M., Koenig, J.L., 1986. Vibrational spectra of carbohydrates. *Adv. Carbohydr. Chem. Biochem.* 44, 7–89.
- Mondragon, G., Fernandes, F., Retegi, A., Peña, C., Algar, I., Eceiza, A., Arbelaiz, A., 2014. A common strategy to extracting cellulose nanoentities from different plants. *Ind. Crop. Prod.* 55, 140–148.
- Moubasher, M.H., Abdel-Hafez, S.I.I., Abdel-Fattah, H.M., Mohanram, A.M., 1982. Fungi of wheat and broad-bean straw composts. *Mycopathologia* 78, 169–176.
- Mussatto, S.I., Dragone, G., Roberto, I.C., 2006. Brewers' spent grain: generation, characteristics and potential applications. *J. Cereal Sci.* 43, 1–14.
- Nawirska, A., Kwasniewska, M., 2005. Dietary fiber fractions from fruit and vegetable processing waste. *Food Chem.* 91, 221–225.
- Panouillé, M., Ralet, M.C., Bonnin, E., Thibault, J.F., 2007. Recovery and reuse of trimmings and pulps from fruit and vegetable processing). In: Klemens, J., Perry, S.J., Waldron, K. (Eds.), *Handbook of Waste Management and Co-Product Recovery in Food Processing*, vol. 1. Woodhead Publishing Ltd, Cambridge, pp. 417–447.
- Schenzel, K., Fischer, S., 2001. NIR FT Raman spectroscopy – a rapid analytical tool for detecting the transformation of cellulose polymorphs. *Cellulose* 8, 49–57.
- Segal, L., Creely, J.J., Martin, A.E., Conrad, C.M., 1959. An empirical method for estimating the degree of crystallinity of native cellulose using the X-Ray diffractometer. *Text. Res. J.* 29, 786–794.
- Siqueira, G., Oksman, K., Tadokoro, S.K., Mathew, A.P., 2016. Re-dispersible carrot nanofibers with high mechanical properties and reinforcing capacity for use in composite materials. *Compos. Sci. Technol.* 123, 49–56.
- Sonneveld, E.J., Visser, J.W., 1975. Automatic collection of powder data from photographs. *J. Appl. Crystallogr.* 8, 1–7.
- Spence, K.L., Venditti, R.A., Rojas, O.J., Habibi, Y., Pawlak, J.J., 2011. A comparative study of energy consumption and physical properties of microfibrillated cellulose produced by different processing methods. *Cellulose* 18, 1097–1111.
- Wiley, J.H., Atalla, R.H., 1987. Band assignments in the Raman spectra of celluloses. *Carbohydr. Res.* 160, 113–129.

PAPER 2

Switchable ionic liquids enable efficient nanofibrillation of wood pulp

Berglund L., Anugwom I., Aitomäki Y., Mikkola JP., Oksman K.

Cellulose 24 (2017) 3265
<https://doi.org/10.1007/s10570-017-1354-2>

Switchable ionic liquids enable efficient nanofibrillation of wood pulp

Linn Berglund · Ikenna Anugwom · Mattias Hedenström · Yvonne Aitomäki · Jyri-Pekka Mikkola · Kristiina Oksman 

Received: 23 February 2017 / Accepted: 25 May 2017 / Published online: 6 June 2017
© The Author(s) 2017. This article is an open access publication

Abstract Use of switchable ionic liquid (SIL) pulp offers an efficient and greener technology to produce nanofibers via ultrafine grinding. In this study, we demonstrate that SIL pulp opens up a mechanically efficient route to the nanofibrillation of wood pulp, thus providing both a low cost and chemically benign route to the production of cellulose nanofibers. The degree of fibrillation during the process was evaluated by viscosity and optical microscopy of SIL treated, bleached SIL treated and a reference pulp. Furthermore, films were prepared from the fibrillated material

for characterization and tensile testing. It was observed that substantially improved mechanical properties were attained as a result of the grinding process, thus signifying nanofibrillation. Both SIL treated and bleached SIL treated pulps were fibrillated into nanofibers with fiber diameters below 15 nm thus forming networks of hydrophilic nature with an intact crystalline structure. Notably, it was found that the SIL pulp could be fibrillated more efficiently than traditional pulp since nanofibers could be produced with more than 30% less energy when compared to the reference pulp. Additionally, bleaching reduced the energy demand by further 16%. The study demonstrated that this switchable ionic liquid treatment has considerable potential in the commercial production of nanofibers due to the increased efficiency in fibrillation.

Electronic supplementary material The online version of this article (doi:10.1007/s10570-017-1354-2) contains supplementary material, which is available to authorized users.

L. Berglund · Y. Aitomäki · K. Oksman (✉)
Division of Materials Science, Composite Center Sweden,
Luleå University of Technology, 97187 Luleå, Sweden
e-mail: kristiina.oksman@ltu.se

I. Anugwom · M. Hedenström · J.-P. Mikkola
Technical Chemistry, Department of Chemistry,
Chemical-Biological Centre, Umeå University, Umeå,
Sweden

I. Anugwom · J.-P. Mikkola
Laboratory of Industrial Chemistry and Reaction
Engineering, Johan Gadolin Process Chemistry Centre,
Åbo Akademi University, Turku, Finland

K. Oksman
Fibre and Particle Engineering, University of Oulu, Oulu,
Finland

Keywords Switchable ionic liquids (SIL) · Efficient fibrillation · Wood pulp · Cellulose nanofiber · Ultrafine grinding

Introduction

The utilization of the cellulose component of wood in various industrial processes would be greatly enhanced by the development of greener approaches to its fractionation. One such approach is the development of greener solvents for the extraction processes, such as deep eutectic solvents (Selkälä et al.

2016) and ionic liquids (Pang et al. 2016) to mention but a few. ‘Traditional’ ionic liquids (ILs) are a subclass of molten salts composed of mainly organic cations and inorganic as well as organic anions, and frequently demonstrate melting points below the boiling point of water. More recently many families of more advanced ILs such as ‘switchable’ ILs have emerged (Anugwom et al. 2014b). Ionic liquids are interesting due to their tunable properties, rendering them suitable as solvents in many applications. Moreover, multitude of ionic liquids has high chemical and thermal stabilities and a wide liquidus range (Wasserscheid and Welton 2006). Several papers can be found in the literature that describes the use of conventional ionic liquids (ILs) in the fractionation of wood. Examples of such ionic liquids include 1-butyl-3-methylimidazolium chloride [C₄MIM][Cl], (Swatloski et al. 2002) and 1-ethyl-3-methylimidazolium acetate [E₂MIM][OAc], which in ionic liquid-mediated technology, have been reported as powerful when used to produce cellulose nanocrystals directly from wood (Abushammala et al. 2015).

However, the limitations associated with the use of conventional ionic liquids for biomass treatment are high cost, the use of precursors originating from fossil resources, multi-step industrial protocols and ambiguous recycling protocols for many of the formulations. These issues thus rendering them unattractive in large-scale processes. A typical drawback with them is the high viscosity of the wood-IL systems after dissolution, which makes recycling, recovery, and reuse of the ionic liquids less viable. Several recovery methods for ionic liquids used for biomass dissolution have been reported. These methods mainly involve the addition of an anti-solvent. The dissolved material can be precipitated out and the anti-solvent removed from the spent ionic liquid by evaporation (D’Andola et al. 2008; Varanasi et al. 2008). Switchable ionic liquids (SILs), on the other hand, are capable of ionic/non-ionic switching, for example, molecular-to-ionic switching by the addition or removal of a so called “trigger compound” (Anugwom et al. 2011; Jessop et al. 2005). It has been demonstrated in our earlier studies that SILs are potential novel solvents for fractionating lignocellulosic material into its various constituents (Anugwom et al. 2012a; Eta et al. 2014a, b). The power of SILs as solvents for biomass deconstruction was further strengthened when a new

protocol, the short time high temperature (STHT) approach (Anugwom et al. 2014b) was carried out for delignification of lignocellulose biomass. The STHT approach was shown to be an efficient way to remove biomass lignin whereupon heavily diluted, aqueous solutions of switchable ionic liquids (SIL) as solvents were used to achieve an impressive delignification efficiency of 95 wt% (Anugwom et al. 2011). Further, the process was operated at low temperatures with a very short treatment time and at low wood-to-ionic solvent ratios. The solvent’s capacity for biomass deconstruction is the key to increasing process efficiency of the following mechanical processing of the pulp such as in the disintegration of the cellulose fibers to the nanoscale. Ultra-fine grinding techniques have been recognized as the most efficient approach in terms of energy consumed (Spence et al. 2011), and thus has great potential for the commercial, scaled-up production of nanofibers, since reduction of the processing energy is one of the most important prerequisites for industrial production. The aim of this study is to evaluate the use of switchable ionic liquids as a rapid, effective and chemical benign route to producing nanofibers from wood chips using ultrafine grinding.

Firstly, the fibrillation process of SIL treated wood pulp and a bleached SIL treated wood pulp to nanofibers is assessed and compared to that the fibrillation to nanofibers from a reference pulp, in this case a birch Kraft pulp. Secondly, the quality of the nanofibers produced was assessed by a comparison of their characteristics. To assess the fibrillation process, viscosity measurements and optical microscopy (OM) were used during the grinding process and mechanical properties of the films prepared from the fibrillated suspension were tested to evaluate the degree of separation. The energy consumption was also measured during the grinding process. The quality assessment of the nanofibers comprised of a study of the nuclear magnetic resonance spectroscopy (NMR) of the pulps before and after the treatment; the crystallinity of the materials before and after the fibrillation; the water contact angle and surface roughness the wood nanofiber films and the size distribution of the nanofibers characterized using atomic force microscope (AFM). Further to this, a chemical composition of the ionic liquid, SO₂ switched DBU MEASIL derived birch pulp was studied before and after the treatment.

Experimental section

Materials

Hardwood birch (*Betula pendula*) in the form of chips was used as raw material for production of nanofibers and was provided by the Natural Resources Institute Finland, (Luke). The reference material was a commercial birch Kraft pulp provided by SCA (Munk-sund, SE). Used, as received, were the SIL precursors, 1,8-diazabicyclo-[5.4.0]-undec-7-ene (DBU, 99%) and monoethanol amine (MEA, 99%) from Sigma Aldrich and the SO₂ (99.998%, H₂O < 3 ppm) provided by AGA Oy (Linde group, Finland). The isopropyl alcohol (2-propanol) (Merck, 99%, USA) that was applied as the anti-solvent and for washing of the fractions. This was also used as received.

Synthesis of the switchable ionic liquid

The SIL (SO₂ switched DBU MEASIL) was prepared from DBU, MEA, and SO₂ by methods described previously in detail (Anugwom et al. 2011; Jessop et al. 2005). An equimolar mixture of DBU and MEA was added into a three-necked flask and the flask was placed in a cooling bath to control the temperature as an exothermic reaction occurs upon the addition of the acidic gas. After that, SO₂ was bubbled through the mixture under rigorous stirring. The reaction in the mixture was allowed to proceed freely upon sparging until the formation of the SIL was completed, (Fig. 1). After this, the SIL was kept in a freezer to prevent its decomposition until it was needed. The molar ratio of the amidine (DBU) to hydroxyl containing compound (MEA) was determined based on the number of hydroxyl groups in the alcohol/hydroxyl-containing compound.

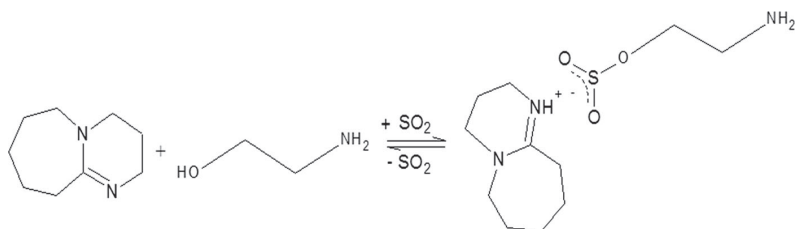
Ionic liquid treatment of woody biomass in a non-stirred batch reactor

A 300 ml capacity batch autoclave (Parr Inc., USA) with an electric heater and an internal thermocouple was used in this study. 50 g of birch chips (approx. 2.3 cm × 8 cm), together with 250 g of SO₂ switched DBU MEASIL and 150 ml of water were placed into the reactor to give a weight ratio of 1:5:3 of wood: SO₂ DBU MEASIL: water. This was heated to 160 °C (433 K) for 2 h. No stirring was employed in order to avoid mechanical fibrillation of the chips during the treatment and consequent a low mixture viscosity could be maintained thus facilitating washing. It should also be mentioned that our earlier studies have shown that the process works well even in the absence of stirring. Upon completion of the treatment, the treated wood was subject to washing with a mixture of propanol and water until no visual evidence of the SIL could be found remaining in the solid fraction. This was further verified by testing for traces of sulphate ion in the filtrate using 10 vol% barium chloride. The SIL pulp samples were subsequently bleached and used for cellulose nanofiber production or used directly without bleaching. In neither case were the samples dried before use.

Bleaching procedure

Bleaching of the SIL treated biomass was performed using acid chlorite bleaching following a previously described procedure by Anugwom et al. (2014a). Briefly a sample of 1 g was bleached with 0.8 g NaClO₂ and 0.16 g AcOH in 40 ml water, at 75 °C for 2 h and the chemicals were added in two portions.

Fig. 1 Synthesis of DBUMEASO₂ SIL. Adapted from Anugwom et al. (2014a)



Fibrillation process

The SIL treated pulp was diluted to 2 wt% concentration, and the bleached SIL pulp and reference pulp were diluted to 1.5 wt% solids respectively, before the fibrillation. Prior to grinding, the suspensions were dispersed using a shear mixer Silverson L4RT, (Silverson Machine Ltd., England). The materials were processed using an MKCA6-3 Supermasscolloider ultrafine friction grinder (Masuko Sangyo Co. Japan), see Fig. 2. Coarse silica carbide (SiC), non-porous standard stones for soft materials were used in the grinding. The grinding was operated in contact mode with a gap between the two disks set to $-60\text{ }\mu\text{m}$, at 1500 rpm, for the initial fibrillation stage, and further adjusted to $-90\text{ }\mu\text{m}$, for the remainder of the grinding process.

The SIL treated pulp was ground for a total duration of 150 min, compared to the bleached SIL pulp, which was processed for 70 min. The processing time in case

of the reference pulp was 100 min. The energy consumption for the grinding process was established on the direct measurement of power using a power meter, Carlo Gavazzi, EM24 DIN (Italy) and the processing time. The energy demand was calculated from the product of power and time and expressed as MWh per dry weight ton of the nanofibers.

The samples were collected at regular intervals during the fibrillation process and characterized by viscosity measurements together with the optical microscope in order to assess the degree of fibrillation. The grinding process was stopped when a plateau in viscosity was reached and no larger structures could be observed by polarized microscope.

Preparation of films

Films containing various degrees of mechanical disintegration were prepared to assess the degree of fibrillation. After the grinding, the suspensions were adjusted to 0.2 wt% concentration and dispersed with a shear mixer, IKA T25, UltraTurrax, (IKA-Werke GmbH & Co., Germany), operated at 10,000 rpm for 10 min. The suspensions were then degassed and subsequently filtered with a membrane filter; pore size $0.45\text{ }\mu\text{m}$, with a glass filter support. The wet cakes obtained were dried by hot pressing at $85\text{ }^{\circ}\text{C}$, using Fortune presses, LP300, (Fontijne Grotnes, The Netherlands), under 30 kPa for 40 min.

Characterization

Chemical analysis: cellulose and hemicellulose content The carbohydrate content of the samples was analyzed by gas chromatography (GC) after acid methanolysis, followed by silylation and acid hydrolysis followed by silylation to determine the hemicellulose and cellulose content of the sample, respectively (Sundberg et al. 1996; Willför et al. 2005; Anugwom et al. 2012b). For GC analysis, approximately $2\text{ }\mu\text{l}$ of the silylated sample was injected through a split injector ($260\text{ }^{\circ}\text{C}$, split ratio 1:5) into a capillary column coated with dimethyl polysiloxane (HP-1, Hewlett Packard). The column length, internal diameter and film thickness were 30 m, 320 and $0.17\text{ }\mu\text{m}$, respectively. The temperature program applied was a $4\text{ }^{\circ}\text{C}/\text{min}$ ramp from 100 to $175\text{ }^{\circ}\text{C}$ followed by $12\text{ }^{\circ}\text{C}/\text{min}$ ramp from 175 to $290\text{ }^{\circ}\text{C}$. The detector (FID) temperature was $290\text{ }^{\circ}\text{C}$.



Fig. 2 Diagram and visual appearance of the materials during the process starting from birch wood chips to final SIL treated wood nanofiber gels. The diagram includes the reference material

and hydrogen was used as the carrier gas. GC–MS (mass spectrometry) was used to identify the different peaks prior to the GC analysis.

Lignin content determination The lignin content was determined using a modified method similar to the Klason lignin method but in which an autoclave treatment at 125 °C and 1.4 bar for 90 min is used to complete hydrolysis of polysaccharides instead of boiling for 4 h (Anugwom et al. 2012a; Schwanninger and Hinterstoisser 2002).

Nuclear magnetic resonance spectroscopy (NMR) ^{13}C cross-polarization magic angle spinning (CP/MAS) experiments were performed on a Bruker 500 MHz Avance III spectrometer operating at a ^{13}C frequency of 125.75 MHz and equipped with a 4 mm MAS probe. The SIL treated- and the reference pulp were analyzed as non-dried pulp but due to the high water content, the bleached SIL pulp was air-dried before analysis. 1 ms contact time was used and 4096 scans were collected for each sample at a spin rate of 10 kHz. The spectral data was processed with Topspin 3.2 software (Bruker Biospin, Germany) using a Gaussian window function. All spectra were recorded at ambient temperature.

Optical microscopy (OM) The lateral dimensions of the raw materials, before the grinding process, were measured using a polarizing microscope, Nikon Eclipse LV100N POL (Japan) and the imaging software NIS-Elements D 4.30. The average values reported are based on 60 measurements of different fibers. The microstructure was also evaluated during the mechanical disintegration process.

Viscosity Viscosity measurements were performed during the grinding using a Vibro Viscometer SV-10, (A&D Company, Ltd, Japan), at a constant shear rate. The velocity (shear rate) of the sensor plates is periodic and based on a sine-wave vibration with a frequency of 30 Hz and amplitude of <1 mm. The viscosity measurements were repeated once the temperature of the samples had been stabilized to 22.7 ± 1.0 °C to confirm that a plateau in viscosity had been reached during fibrillation. The presented values are an average of three measurements for each sample, where the samples were stirred between the measurements.

Atomic force microscopy (AFM) The nanostructure was studied after the mechanical fibrillation for all

samples using an Atomic Force Microscopy. The fibrillated sample suspension (0.01 wt%) was dispersed and deposited by spin coating onto a mica plate for imaging. The measurements were performed on a Veeco Multimode Scanning Probe, USA in tapping mode, with a tip model TESPA [antimony (n) doped Si], Bruker, USA. The nanofiber size (width) was measured from the height images using the Nanoscope V software and the size distribution presented are based on 40 different measurements for each sample. The size distributions were obtained by drawing a line across the height image and subsequently measuring all isolated nanofibers alongside this line. The procedure was repeated for several captured height images until 40 measurements were collected. AFM was also used for characterization of topographical features of the nanofiber films. The root-mean square roughness RMS values were measured from the height images. The images were flattened before the measurements to delete low frequency noise and remove tilt; no other image processing was performed. The values reported are the average of five different measurements on the surface area of $25 \mu\text{m}^2$. All measurements were conducted in air at room temperature.

Density and porosity The density of the films was calculated by determining the weight, area, and thickness of the dried network. The weight was determined using an analytic balance, and the thickness was the average of ten different measurements at different locations measured with a micrometer gauge. The porosity, P , was estimated from the density of the dried cellulose network, ρ_b , by assuming that the density of the nanofiber is $\rho_f = 1.5 \text{ g/cm}^3$ (Eichhorn et al. 2010), such that:

$$P = 1 - [\rho_b / \rho_f] \quad (1)$$

Scanning electron microscopy (SEM) The morphologies of the films fracture surfaces were studied by SEM, JEOL, and JSM-IT300LV (USA) at an acceleration voltage of 10 kV. The samples were coated prior to the scanning using Bal-Tec MED 020 Coating system with a tungsten target to avoid charging.

Mechanical properties The mechanical properties of the films networks structures, isolated after different processing times, were tested to provide an indication of the degree of fibrillation. Film samples cut to

40 mm in length and 5 mm in width were attached to paper frames to facilitate the mounting in the tensile machine. The tests were conducted using universal tensile testing equipment; AG X, (Shimadzu, Japan) equipped with 1 kN load cell. The tests were conducted at extension rate of 2 mm/min and the gauge length used was about 20 mm. Prior to experiments, all the samples were conditioned at $50 \pm 2.0\%$ relative humidity at 23 ± 1.0 °C for at least 24 h. The results are the average of at least eight sets of measurements.

X-ray diffraction (XRD) The diffraction patterns were obtained using XRD technique and the instrument used was a PANalytical Empyrean X-ray diffractometer (The Netherlands) equipped with a PIXcel^{3D} detector and Cu Ka radiation ($\lambda = 0.154$ nm). The X-ray generator was operating at 45 kV and 40 ma, respectively. The crystallinity index (CI) was calculated based on the Segal empirical method (Segal et al. 1959):

$$CI = [(I_{200} - I_{am})/I_{200}] \times 100 \quad (2)$$

where I_{200} is the intensity of the crystalline peak and I_{am} refers to the intensity of the amorphous peak. A baseline correction based on Sonneveld and Visser (1975) was used.

Contact angle measurements The water contact angle of the nanofibers films was measured using an EASYDROP contact angle measuring system with drop shape analysis DSA1 control and evaluation software (Krüss, Germany). A 4 µl drop of water was placed onto the sample and the software of the instrument calculated the contact angle over time with a sessile drop technique; the contact angle was determined immediately after a stable drop was formed on the sample surface and used for comparison of the nanofiber networks. The reported values are the average based on five measurements.

Results and discussion

Chemical composition of the DBUMEASO₂SIL treated materials

After the SIL treatment using the Short Time-High temperature (STHT) approach (Anugwom et al. 2014b), a ~40 wt% reduction of the original weight

was recorded after washing. The bleached and unbleached woody material after the SIL treatment was subjected to chemical analysis to determine its lignin, cellulose and hemicellulose contents, respectively. The result of the chemical analysis is given in Online Resource 1, together with the results for the reference pulp. The SIL treatment reduced the lignin content by 91 wt% compared to the total amount in the untreated wood, resulting in marginally lower lignin content than the reference pulp. The bleaching cycle further reduced the lignin content of the SIL treated wood to less than 2 wt%, thus half that of the lignin content of the SIL treated- and reference pulp. As shown previously, the SIL used was selective towards lignin dissolution (Anugwom et al. 2012a). The results of removal of hemicelluloses were similar in both the SIL treated- and the reference pulp. Bleaching combined with the SIL treatment further decreased the hemicellulose content (see Online Resource 1). In addition, the SIL treatment successfully removed over 90 wt% of the pectins and uronic acids from the wood.

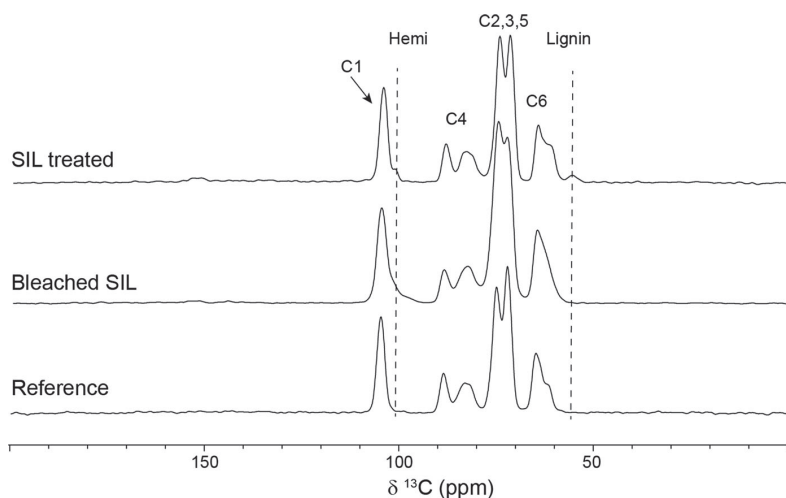
Nuclear magnetic resonance spectroscopy (NMR) analysis

¹³C CP/MAS NMR spectra of SIL treated and bleached SIL pulps were compared to the reference pulp to further elucidate the effect of the SIL treatment on the woody material. Signals from cellulose appear in the region between 60 and 110 ppm, annotated C1–C6 in Fig. 3. The signal at 89 ppm originates from C-4 of the highly ordered cellulose of the crystallite interiors while the broader up-field signal at 84 ppm is assigned to the C-4 of disordered cellulose (Larsson et al. 1999).

Lignin peaks usually appear in the region of 125–160 ppm with the exception of the methoxyl peak, which is located at 56 ppm. Signals from hemicelluloses overlap to a large extent with the cellulose peaks but presence of hemicellulose can be observed as a hump on the up-field side of the C1 peak from cellulose (Liitiä et al. 2003). Comparing the peak intensities of the different materials, it is clear that only small amounts of lignin and hemicellulose fractions are present, leaving only the cellulose peaks as the dominating features of the spectra (Fig. 3).

These results confirm the results from chemical analysis showing the SIL treated and bleached SIL contain minor amounts of hemicellulose. In addition,

Fig. 3 ^{13}C CP/MAS spectra of SIL treated pulp, bleached SIL pulp and the reference



it is evident that the lignin still present after the SIL treatment gives rise to methoxyl resonances, which are no longer present after the subsequent bleaching process confirming the reduction in lignin. The presence of lignin in the reference material is not clearly seen in the spectra possibly reflecting the accuracy of NMR in detecting low lignin levels.

Microstructure

The optical micrographs of the samples obtained before and during the fibrillation at different processing times in the ultrafine grinder are presented in Fig. 4. The raw materials size was measured for the wood pulps prior to the mechanical disintegration. The Fig. 4 depicts that the SIL treated material appears as larger bundles and had an average width of $89 \pm 27 \mu\text{m}$ and that the bleaching treatment resulted in decreased dimensions to around $31 \pm 9 \mu\text{m}$, which is similar to the reference material at $27 \pm 7 \mu\text{m}$. The larger initial size of the SIL material is likely to be due to the fact that the SIL treatment was carried out in the absence of any stirring whereas the reference pulp was subjected to considerable shearing forces during the industrial bleaching process. The subsequent bleaching of the material also involves a stirring albeit with relatively low shear forces. As intended, the grinding process further reduced the size of fibers to the nanoscale in all pulps but with considerable differences in the time taken depending on the raw material

and its treatment. No intact fibers were observed after the grinding, though remaining fragments from the cell wall structure could be seen.

The larger woody structures observed for the SIL treated unground material appeared to require further a processing time of approximately 40 min to separate them before internal fibrillation could be initiated. However, in the bleached SIL, the initiation of internal fibrillation appeared much earlier and fibrillation was observed at the fiber ends after only 20 min of processing. After 40 min, comprehensive disintegration was observed for the bleached SIL. At 40 min, the reference material appears to be at a further stage of the disintegration than the SIL but not as advanced as the bleached SIL material.

The more rapid fibrillation for the bleached SIL pulp could be attributed to the combination of initially smaller fiber dimensions and lower lignin content. For the SIL treated and reference, the lignin may act to maintain the structural integrity of the fiber, thus resulting in a more gradual disintegration process, compared to the bleached SIL.

Atomic force microscopy (AFM) was used for characterizing the nanoscaled material after the grinding process. The captured phase and height images are shown together with the size distribution based on measurements from the height images in Fig. 5.

The AFM confirmed that the fibril dimensions were decreased from micro- to nanoscale upon the grinding process, though bundles of wood nanofibers also were

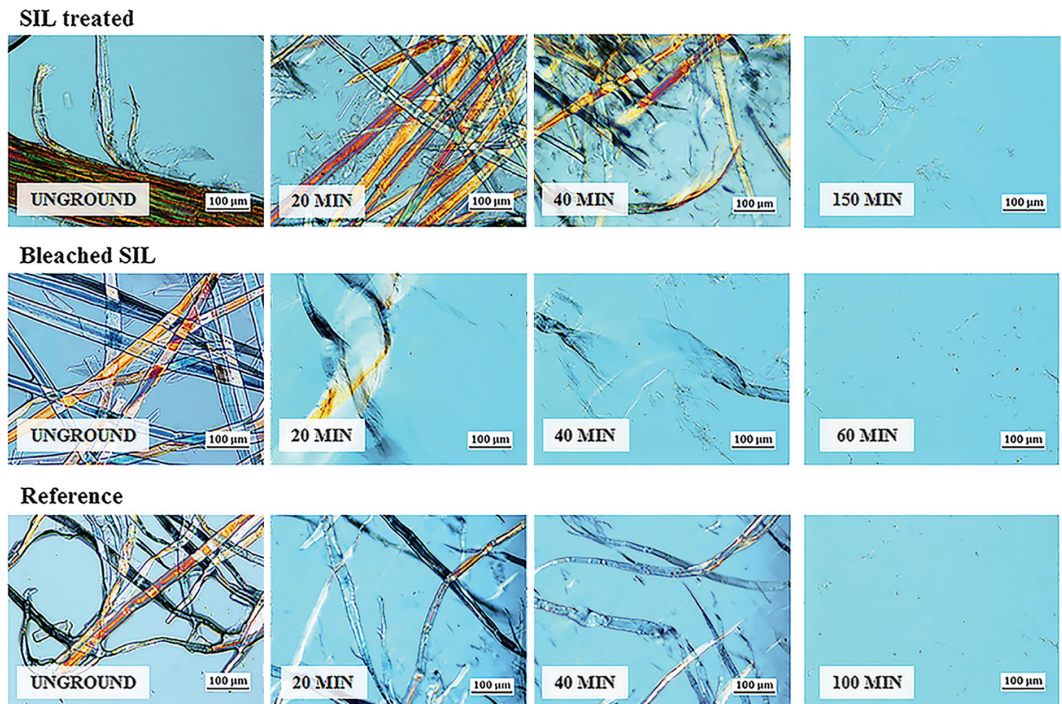


Fig. 4 Fibrillation process of SIL treated pulp, bleached SIL pulp and reference pulp shown with optical microscopy images obtained at different mechanical processing times

observed in all materials. The height measurements of the isolated nanofibers was used to measure the widths of the nanofibers and had averaged values of 15 ± 8 nm for the SIL treated nanofibers, 12 ± 6 nm for the bleached SIL, and in case of the reference 14 ± 6 nm was measured. Thus, no significant differences could be confirmed in the size of the nanofibers in the final nanofiber gels when inspected on this scale and it can be tentatively concluded that the different processing routes and resulting different chemical composition appeared to have minor, if any effect on the nanofiber sizes. However, it should be noted that in AFM measurement, the field of view visualized is restricted and thus larger structures are often overlooked (Chinga-Carrasco 2013).

Viscosity

Figure 6 shows the measured viscosity during the grinding process from samples taken every ten minutes and carried out until a plateau in the viscosity was

reached. The viscosity is shown as function of the energy consumption during the fibrillation process.

The viscosity of the suspensions increased significantly during the mechanical separation and a gel formation was observed. This increase in viscosity is due to the fibrillation process leading to a greater exposure of the surface area of swollen fibrils, promoting more fibril-to-fibril bonding and this, in turn, implies a higher degree of fibrillation. The apparent increase in the viscosity with the progress of the fibrillation process could be seen of all pulps and has been previously reported for grinding of different wood pulps (Lahtinen et al. 2014). The viscosity increase in case of the bleached SIL pulp occurs almost immediately. The gradient is substantially lower for the SIL treated and reference pulp, yet the reference shows the highest maximum viscosity value. The lower gradient observed for the SIL treated pulp despite the fact that the concentration was in fact higher for this pulp. This is best explained by the breakdown of larger structures before gel formation was induced.

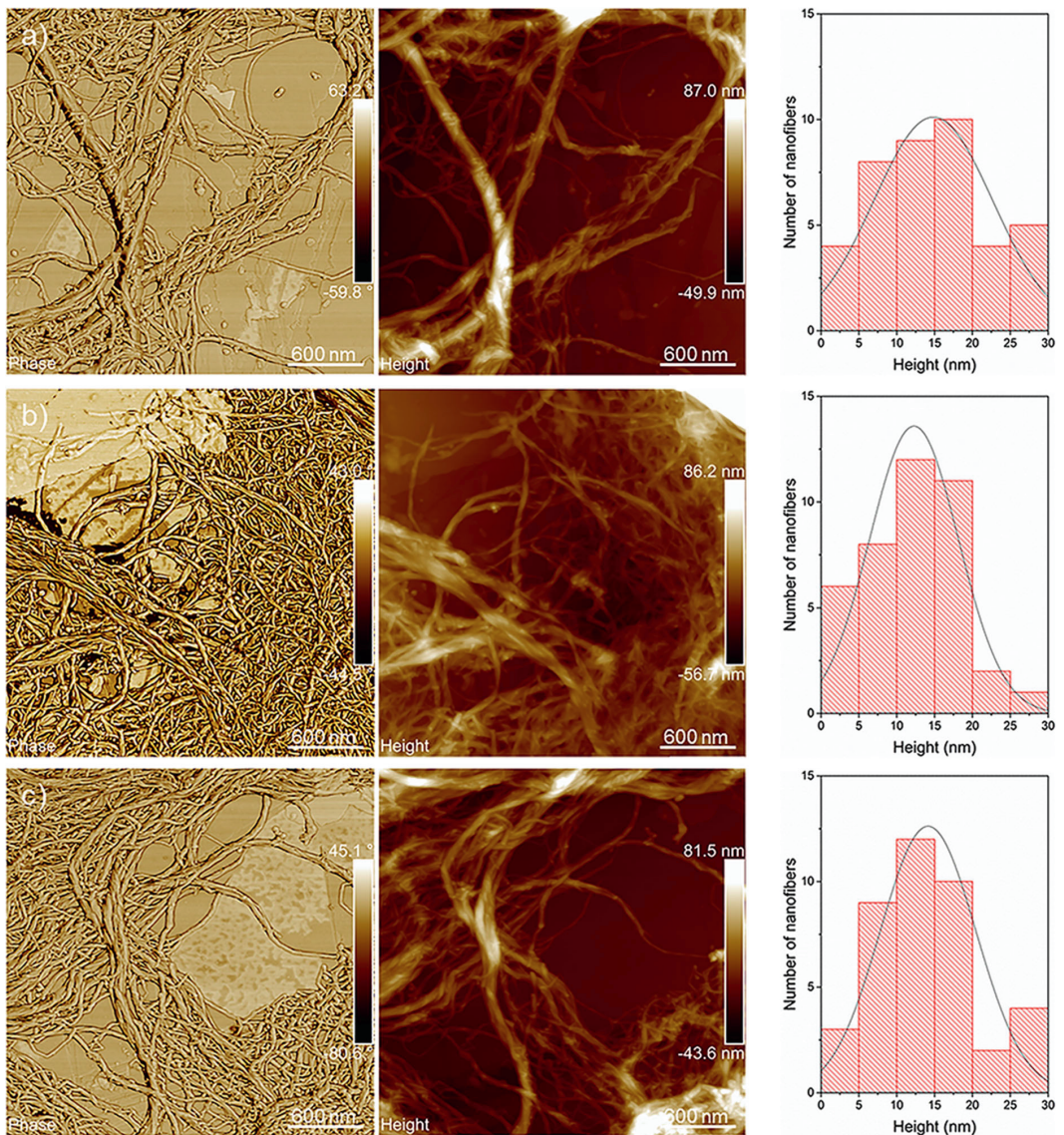


Fig. 5 AFM phase and height images together with the size distribution (from left to right) after fibrillation of **a** SIL treated-, **b** bleached SIL-, and **c** reference nanofibers

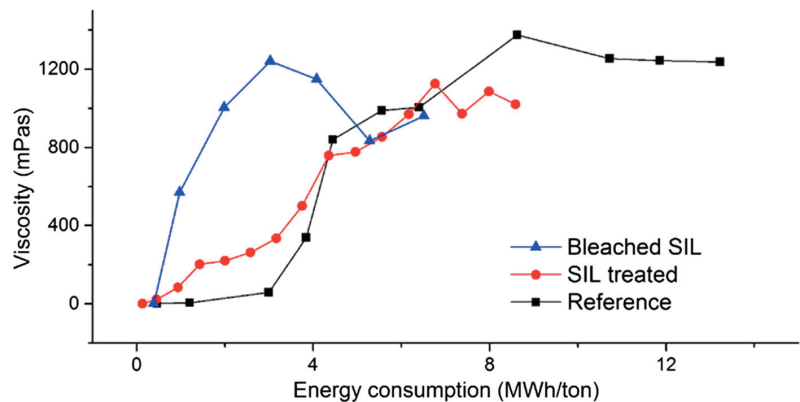
Fiber film characteristics

The films obtained before and after the mechanical fibrillation are presented in Fig. 7, and were characterized in terms of density, porosity, morphology,

mechanical properties, crystalline structure, topography and wetting behavior.

Large structures were clearly seen in the film from unground SIL treated pulp and the resulting porosity was 53 vol%. It also had a brown color, which we

Fig. 6 Viscosity as function of the energy consumption during grinding



presume was from the remaining lignin in the SIL treated material. After fibrillation, the films of the material decreased in porosity to 21 vol% as the nanofibers pack closer than the larger microfibrils, which was observed by SEM of the film fracture surface. The unground bleached SIL pulp films had a porosity at 46 vol% and thus lower than is unbleached counterpart. After fibrillation, the bleached SIL film porosity decreased to 19 vol% which is in similar to both the unbleached and reference nanofiber materials, the latter having a porosity of 59 vol% of the unground film and a final film porosity of 22 vol%. The slightly lower porosity obtained for the bleached SIL film was consistent with the more transparent appearance of the film. The porosity was decreased by about 70 wt% for all films upon the fibrillation process and their morphology showed more closely packed layered structures.

The typical stress–strain curves from testing of the films in uniaxial tension before and after the fibrillation process is presented in Fig. 8. Several factors affect the network mechanical properties of the films and one of these is the degree and to some extent the homogeneity of fibrillation (Aitomäki et al. 2015; Sehaqui et al. 2011).

Both SIL treated samples reached a remarkably higher stress region and the bleaching resulted in further improvement of strain-to-failure compared to the reference material. An increase in the mechanical properties could be seen for all the fibrillated wood pulps, associated with the porosity decrease, owing to the smaller fiber dimensions which, in turn, results in the formation of more inter-fiber bonds (Nair et al. 2014) thus giving higher strength wood nanofiber

networks. The SIL nanofibers do not reach the strength or strain-to-failure of the bleached materials. The remaining lignin may constitute a barrier for the formation of hydrogen bonds between cellulose molecules, mainly due to its more hydrophobic nature compared to cellulose (Shao and Li 2007), this would thus reduce the inter-fiber bonding and lower the strength for the SIL films. However, the results of the reference material which have nearly equivalent amount of both lignin and hemicellulose do not support this as it displayed a network with 20% higher strength, and 30% higher strain-to-failure than the network of SIL nanofibers. This suggests other reasons for reduced inter-fiber bonding in the SIL nanofiber networks such as either the material is less fibrillated or that the residual lignin yielding the brown color has a different effect on the network properties i.e. there is a difference in its surface chemistry compared to the remaining lignin in the reference material. The two possibilities are supported by the results of the bleached SIL nanofibers which displayed a 10% higher strength and about 20% increase in the strain-to-failure, and has a reduced lignin content of about 60 wt% compared to the SIL nanofibers and a rapid disintegration of the larger wood structures in the fibrillation process.

The fibrillation occurring upon ultrafine grinding is a result of complex phenomena that are affected by the concentration of the suspensions, gap between the grinding stones (Wang et al. 2012), speed of rotation of the grinding stones (Jonoobi et al. 2012), and the processing time (Nair et al. 2014), all of which contribute to the energy consumption of the process and the quality of the nanofibers. Hence, in terms of

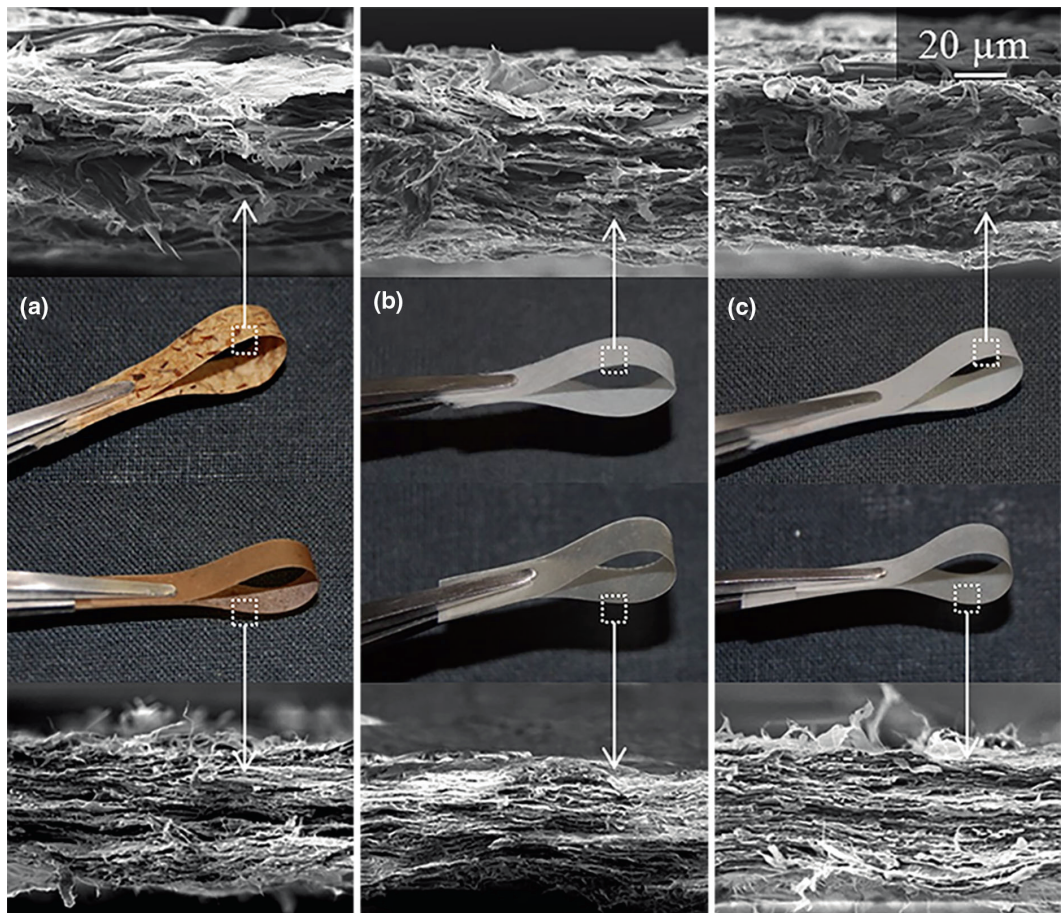
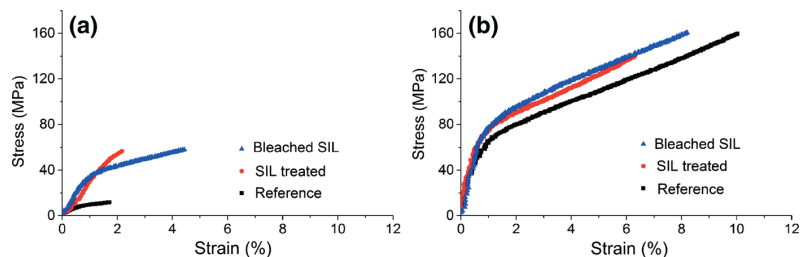


Fig. 7 Photographs and SEM fracture surfaces of the films before (*above*) and after fibrillation (*below*) of **a** SIL treated-, **b** bleached SIL-, and **c** reference pulp

Fig. 8 Typical stress–strain curves for the films from **a** wood pulp, and **b** nanofibers



evaluating the efficiency of a process, the strength, stiffness, strain and density at different fibrillation times, was plotted against the energy consumed during the grinding, shown in Fig. 9.

For the fibrillation process of the wood pulps into nanofibers, the amount of energy consumed (see Fig. 9) for the SIL treated pulp was 9 MWh/ton and, after bleaching, the energy consumption was further

lowered to only 7 MWh/ton. The energy demand for the processing of the reference pulp was measured as 13 MWh/ton. Thus, the bleached SIL pulp could be fibrillated with almost half of the energy demand required for the reference material. In addition, the initial fibrillation appears more efficient for the bleached samples, an observation that may be attributed to the larger structures observed in the non-bleached SIL pulp, which require more energy to be disintegrated.

Interestingly, a more than 20% higher elastic modulus (Fig. 9b) was obtained in case of the bleached SIL nanofiber network with shortest processing time (1 h). Furthermore, a plateau appeared to have been reached for strength Fig. 9a, strain Fig. 9c and density Fig. 9d of the bleached SIL films. Nair et al. (2014) observed a similar behaviour of a plateau when grinding bleached softwood; however, this was reached after 4 h of grinding for strength and strain and 6 h for the density. A plausible explanation for the

Table 1 The crystallinity index of wood pulp and nanofibers, respectively

	Wood pulp (%)	Nanofibers (%)
SIL treated	87	86
Bleached SIL	85	82
Reference	82	80

bleached SIL treated pulp resulting in the most efficient fibrillation is that the large structures remaining in the SIL treated pulp are separated during the bleaching as the remaining lignin is removed, thus enabling a more direct fibrillation in the beginning of the ultrafine grinding process.

In addition to the mechanical properties, the crystalline structure of the films was evaluated before and after the mechanical fibrillation procedure. The crystallinity index (Table 1) was estimated from the X-ray diffraction (XRD) spectra. The diffraction patterns (Online Resource 2) indicated cellulose I

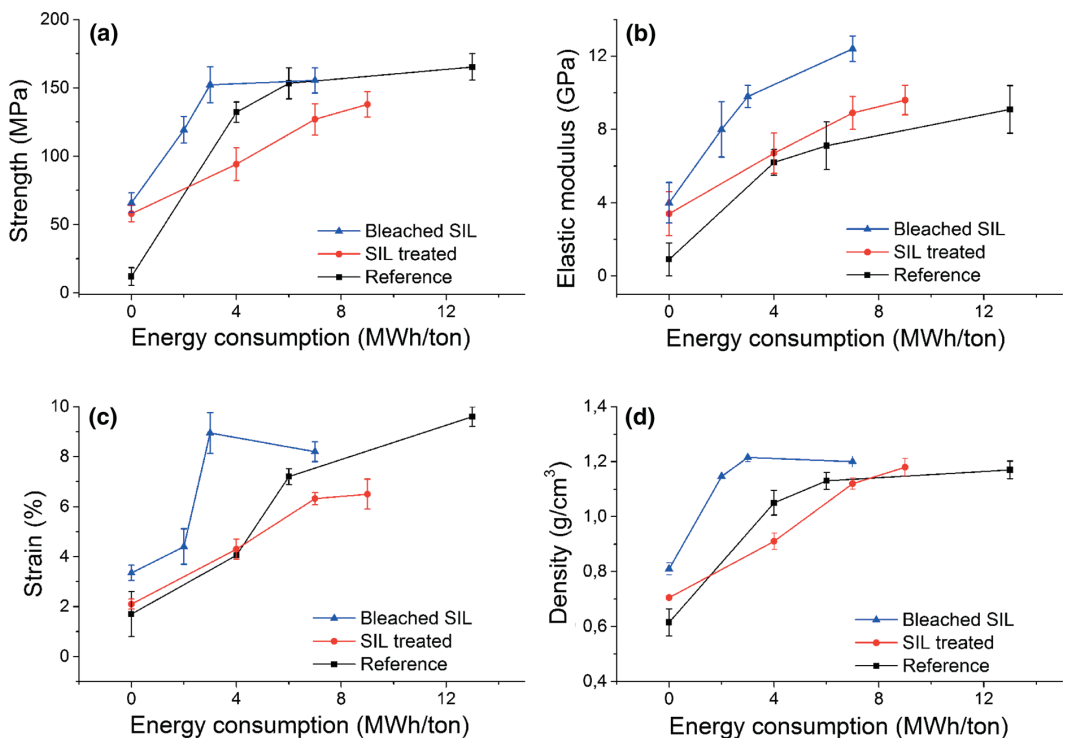
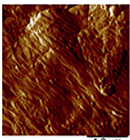
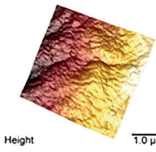
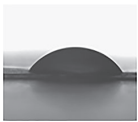
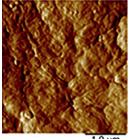
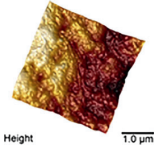
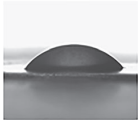
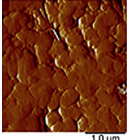
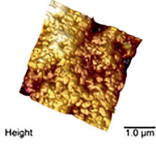
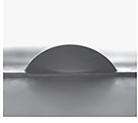


Fig. 9 Mechanical and physical properties of the films at different processing times showing **a** strength-, **b** elastic modulus-, **c** strain-, and **d** density as a function of the energy consumption

Table 2 AFM amplitude images the nanofibers films derived from SIL-, bleached SIL-, and reference pulps

Nanofiber network		RMS roughness (nm)		Contact angle (°)	
SIL treated		81 ± 5.6		60 ± 3.0	
Bleached SIL					
Reference					

The root-mean square roughness value and the AFM 3D height images of the surface roughness, and the water contact angle respectively

structure with the characteristic 2θ diffraction angles close to 14.5° , 16.3° (overlapping peaks) and 22.5° for all pretreated pulps.

The use of different techniques for the determination of the crystallinity index renders it difficult to compare results with between studies since large variations between the use of different methods and baseline corrections has been shown (Park et al. 2010). Still, the values estimated in this study before and after the fibrillation are slightly lower to values reported, namely 86 and 90% for wood pulp and nanofibers, respectively, when fibrillated using grinding (Panthapulakkal and Sain 2012). However, it should be noted that the peak height method used in this study for estimation of the crystallinity index has been shown to underestimate the amorphous proportion, hence overestimating the relative amount of crystalline cellulose (Park et al. 2010). For this reason, the crystallinity index values in Table 1 should only be used for comparison between the samples. The results indicate that no dissolution of cellulose occurred during the SIL treatment, displaying cellulose I crystalline structure. The crystallinity index values were comparable to each other further indicating that neither the SIL treatment nor the grinding degrades the crystalline

structures of the cellulose nanofibers with the processing conditions used in this study.

Water contact angle measurement was used to evaluate any differences of the nanofiber film surfaces and the results are shown in Table 2 together with the surface root-mean square roughness values obtain from measurements with the AFM.

All the nanofibers showed hydrophilic nature with contact angles lower than 90° . Spence et al. (2010) showed that an increased contact angle value is associated with higher lignin content in wood pulps. Since lignin is less hydrophilic than cellulose, higher contact angles of the wood nanofibers films from SIL- and reference pulp were expected. The results did indeed follow this behavior and higher contact angles were found for SIL nanofibers and reference nanofibers, namely 60° and 62° respectively, compared to 54° for the bleached SIL nanofibers which has the lowest lignin content. It is also known that the water contact angle correlates with the topographical structure of the surface (Herrera et al. 2014). However, in this case any influence that the surface roughness has on the contact angle cannot be distinguished as significant, when the standard deviations are taken into account.

Conclusions

Switchable ionic liquid (SIL) processing was demonstrated as having a high commercial potential for pulping wood prior to mechanical fibrillation into nanofibers.

The SIL treatment drastically reduced the energy demand of obtaining nanofibers with diameters measured below 15 nm and intact crystalline structures with ultrafine grinding.

Furthermore, the porosity of the films made from the materials decreased by 70 wt% after fibrillation and an associated increase in the network strength was observed. In addition, a high elastic modulus was shown for the SIL nanofiber films at 9.6 and 12.4 GPa for the bleached SIL films. Bleached SIL nanofiber films have strength matching that of other nanofiber materials from ultrafine grinding. However, SIL nanofiber films were found to have a slightly lower strength.

The reduced energy demand (more than 30%) was achieved when SIL treated pulp was used compared to the reference pulp upon fibrillation through grinding. Additionally, bleaching reduced the energy consumption a further 16%.

Thus, bleached SIL pulp can yield nanofibers with virtually half the energy consumption compared to the bleached reference pulp, which together with the benign nature of the chemicals and the potential ease of solvent recycling render the commercial operations for the production of nanofibers much more realistic.

Acknowledgments The authors would like to acknowledge the financial support under Bio4Energy—a strategic research environment appointed by the Swedish government, Wallenberg Wood Science Center (WWSC) and Nordic Forest research (SNS) WoodPro.

Compliance with ethical standards

Conflicts of interest The authors declare that they have no conflict of interest.

Open Access This article is distributed under the terms of the Creative Commons Attribution 4.0 International License (<http://creativecommons.org/licenses/by/4.0/>), which permits unrestricted use, distribution, and reproduction in any medium, provided you give appropriate credit to the original author(s) and the source, provide a link to the Creative Commons license, and indicate if changes were made.

References

- Abushammala H, Krossing I, Laboire MP (2015) Ionic liquid-mediated technology to produce cellulose nanocrystals directly from wood. *Carbohydr Polym* 134:609–616
- Aitomäki Y, Moreno-Rodriguez S, Lundström S, Oksman K (2015) Vacuum infusion of nanocellulose networks of different porosity. In: Proceedings of the 20th international conference on composite materials, Copenhagen, Denmark
- Anugwom I, Mäki-Arvela P, Virtanen P, Damlin P, Sjöholm R, Mikkola JP (2011) Switchable ionic liquids (SILs) based on glycerol and acid gases. *RSC Adv* 1:452–457
- Anugwom I, Mäki-Arvela P, Virtanen P, Willför S, Damlin P, Hedenström M, Mikkola JP (2012a) Treating birch wood with a switchable 1,8-diazabicyclo-[5.4.0]-undec-7-ene-glycerol carbonate ionic liquid. *Holzforschung* 66:809–815
- Anugwom I, Mäki-Arvela P, Virtanen P, Willför S, Sjöholm R, Mikkola JP (2012b) Selective extraction of hemicelluloses from spruce using switchable ionic liquids. *Carbohydr Polym* 87:2005–2011
- Anugwom I, Eta V, Mäki-Arvela P, Virtanen P, Hedenström M, Hummel M, Sixta H, Mikkola JP (2014a) Switchable ionic liquids as delignification solvents for lignocellulosic materials. *Chemsuschem* 7:1170–1176
- Anugwom I, Eta V, Mäki-Arvela P, Virtanen P, Hedenström M, Yibo M, Hummel M, Sixta H, Mikkola JP (2014b) Towards optimal selective fractionation for Nordic woody biomass using novel amine–organic superbase derived switchable ionic liquids (SILs). *Biomass Bioenergy* 70:373–381
- Chinga-Carrasco G (2013) Optical methods for the quantification of the fibrillation degree of bleached MFC materials. *Micron* 48:42–48
- D'Andola G, Szarvas L, Massonne K, Stegmann V (2008) Ionic liquids for solubilization of polymers. WO Patent 2008/043837
- Eichhorn SJ, Dufresne A, Aranguren M, Marcovich NE, Capadona JR, Rowan SJ et al (2010) Review: current international research into cellulose nanofibres and nanocomposites. *Mater Sci* 45:1–33
- Eta V, Anugwom I, Virtanen P, Eränen K, Mäki-Arvela P, Mikkola JP (2014a) Loop vs. batch reactor setups in the fractionation of birch chips using switchable ionic liquids. *Chem Eng J* 238:242–248
- Eta V, Anugwom I, Virtanen P, Mäki-Arvela P, Mikkola JP (2014b) Enhanced mass transfer upon switchable ionic liquid mediated wood fractionation. *Ind Crops Prod* 55:109–115
- Herrera MA, Mathew AP, Oksman K (2014) Gas permeability and selectivity of cellulose nanocrystals films (layers) deposited by spin coating. *Carbohydr Polym* 112:494–501
- Jessop PG, Heldebrandt DJ, Xiaowang L, Eckert CA, Liotta CL (2005) Green chemistry: reversible nonpolar-to-polar solvent. *Nature* 436:1102
- Jonoobi M, Mathew AP, Oksman K (2012) Producing low-cost cellulose nanofiber from sludge as new source of raw materials. *Ind Crops Prod* 40:232–238
- Lahtinen P, Liukkonen S, Pere J, Sneek A, Kangas H (2014) A comparative study of fibrillated fibers from different

- mechanical and chemical pulps. *BioResources* 9: 2115–2127
- Larsson PT, Hult EL, Wickholm K, Pettersson E, Iversen T (1999) CP/MAS ¹³C-NMR spectroscopy applied to structure and interaction studies on cellulose I. *Solid State Nucl Magn Reson* 15:31–40
- Liitiä T, Maunu SL, Hortling B, Tamminen T, Pekkala O, Varhimo A (2003) Cellulose crystallinity and ordering of hemicelluloses in pine and birch pulps as revealed by solid-state NMR spectroscopic methods. *Cellulose* 10:307–316
- Nair SS, Zhu JY, Deng Y, Ragauskas AJ (2014) Characterization of cellulose nanofibrillation by micro grinding. *J Nanopart Res* 16:2349–2359
- Pang Z, Dong C, Pan X (2016) Enhanced deconstruction and dissolution of lignocellulosic biomass in ionic liquid at high water content by lithium chloride. *Cellulose* 23: 323–338
- Panthapulakkal S, Sain M (2012) Preparation and characterization of cellulose nanofibril films from wood fibre and their thermoplastic polycarbonate composites. *Int J Polym Sci* 2012:1–6
- Park S, Baker J, Himmel M, Parilla P, Johnson D (2010) Cellulose crystallinity index: measurement techniques and their impact on interpreting cellulase performance. *Biotechnol Biofuels* 3:1–10
- Schwanninger M, Hinterstoesser B (2002) Klason lignin: modifications to improve the precision of the standardized determination. *Holzforschung* 56:161–166
- Segal L, Creely JJ, Martin AE, Conrad CM (1959) An empirical method for estimating the degree of crystallinity of native cellulose using the X-ray diffractometer. *Text Res J* 29:786–794
- Sehaqui H, Zhou Q, Ikkala O, Berglund LA (2011) Strong and tough cellulose nanopaper with high specific surface area and porosity. *Biomacromol* 12:3638–3644
- Selkälä T, Sirviö JA, Lorite GS, Liimatainen H (2016) Anionically stabilized cellulose nanofibrils through succinylation pretreatment in urea-lithium chloride deep eutectic solvent. *Chemsuschem* 9:3074–3083
- Shao Z, Li K (2007) The effect of fiber surface lignin on interfibrer bonding. *J Wood Chem Technol* 26:231–244
- Sonneveld EJ, Visser JW (1975) Automatic collection of powder data from photographs. *J Appl Crystallogr* 8:1–7
- Spence KL, Venditti RA, Rojas OJ, Habibi Y, Pawlak JJ (2010) The effect of chemical composition on microfibrillar cellulose films from wood pulps: water interactions and physical properties for packaging applications. *Cellulose* 17:835–848
- Spence KL, Venditti RA, Rojas OJ, Habibi Y, Pawlak JJ (2011) A comparative study of energy consumption and physical properties of microfibrillated cellulose produced by different processing methods. *Cellulose* 18:1097–1111
- Sundberg A, Sundberg K, Lillandt C, Holmbom B (1996) Determination of hemicelluloses and pectins in wood and pulp fibres by acid methanolysis and gas chromatography. *Nord Pulp Pap Res J* 11:216–219
- Swatloski RP, Spear SK, Holbrey JD, Rogers RD (2002) Dissolution of cellulose [correction of cellose] with ionic liquids. *J Am Chem Soc* 124:4974–4975
- Varanasi S, Shall AC, Dado P A, Anderson J, Rao K, Paripati P (2008) Biomass pretreatment. WO Patent 2008/11291A2
- Wang QQ, Zhu JY, Gleisner R, Kuster TA, Baxa U, McNeil SE (2012) Morphological development of cellulose fibrils of a bleached eucalyptus pulp by mechanical fibrillation. *Cellulose* 19:1631–1643
- Wasserscheid P, Welton T (2006) *Ionic liquids in synthesis*. Wiley, Weinheim
- Willför S, Sundberg A, Pranovich A, Holmbom B (2005) Polysaccharides in some industrially important hardwood species. *Wood Sci Technol* 39:601–661

PAPER 3

Direct preparation of alginate/cellulose nanofiber hybrid ink from
brown seaweed for 3D biomimetic hydrogels

Berglund L., Forsberg F., Oksman K.

Manuscript

Direct preparation of alginate/cellulose nanofiber hybrid ink from brown seaweed for 3D biomimetic hydrogels

Linn Berglund[†], Fredrik Forsberg[†] and Kristiina Oksman^{†,‡,§,}*

[†] Department of Engineering Sciences and Mathematics, Luleå University of Technology, 97187, Luleå, Sweden, *e-mail: kristiina.oksman@ltu.se

[‡] Fibre and Particle Engineering, University of Oulu, Oulu, Finland

[§] Mechanical & Industrial Engineering, University of Toronto, Canada

Keywords: Algae, nanofibers, 3D printing, bio-based hydrogels, rheological behavior, microstructure

The present study is inspired by a biomimetic approach that represents the natural design of the cell wall structure. This study aims to derive alginate and cellulose together from both the stipe (stem-like) and blade (leaf-like) structures of brown seaweed; further, this is followed by fibrillation for the direct preparation of alginate/cellulose nanofiber hybrid inks. The fibrillation process was evaluated through viscosity tests and microscopy, and the obtained gels were further studied with regard to their rheological behavior. As a proof of concept, the inks were 3D-printed into discs, followed by crosslinking with CaCl_2 to form biomimetic hydrogels that were

subsequently tested under compression. The study showed that the nanofibrillation of brown seaweed after purification treatment is very energy-efficient, with an energy demand lower than 2 kWh/kg, and with nanofiber dimensions below 15 nm. The shear-thinning inks could successfully be printed into 3D discs that, after crosslinking, exhibited an interconnected network structure with favorable mechanical properties.

INTRODUCTION

Brown seaweed is an encouraging and fascinating natural resource with increasing commercial and ecological importance¹. *Laminaria digitata* is one type of fast-growing and large brown seaweed, which consists of a holdfast (root-like), a stipe (stem-like), and a blade (leaf-like) structure that can grow up to 4 m in length.² It grows along the coasts in the relatively cold Northern hemisphere, and its carbohydrate composition varies with season, geographic location, and age³, as well as between the different parts of the seaweed (stipe and blade)⁴. The polysaccharides in brown seaweed differ considerably from those found in terrestrial plants; although cellulose is present in smaller amounts, alginate is the major structural component of the cell wall. Thus, the most common source of alginate for commercial extraction is brown seaweed², which has further industrial uses such as in dental impression and wound dressing materials and as a stabilizer and thickener in ice cream and food⁵.

Alginate consists of 1,4-glycosidically linked α -L guluronic acid (G) and β -D-mannuronic acid (M). The linear chains are made up of different blocks of guluronic and mannuronic acids, referred to as MM or GG blocks (MG or GM blocks), where the linkage in the block structure results in varying degrees of flexibility or stiffness in the alginates. In the presence of Ca^{2+} , the GG blocks form ionic complexes to generate a stacked (crosslinked) structure known as the 'egg-box model', which is responsible for strong gel formation.⁶ Combined with its biodegradability,

biocompatibility, non-antigenicity, and chelating ability⁵, alginate has been widely utilized in the assembly of hydrogels for biomedical applications such as the engineering of cartilage^{7,8} and bone⁹ tissue, in addition to drug delivery¹⁰. 3D printing of alginate has triggered increased attention to the assembly of hydrogels for biomedical purposes, where one of the main challenges lies in achieving shape fidelity of the 3D structure. Although the viscosity of alginate can be adjusted through its concentration and molecular weight¹¹, its rheological behavior is not sufficiently good for structural integrity while printing. Several researchers have solved this problem by introducing cellulose nanofibers (CNFs) to tailor commercial alginate as ink suitable for 3D printing.^{7,12}

CNFs are further attractive for biomedical applications owing to their good mechanical properties and biocompatibility. CNFs can be isolated from renewable sources, although they are often associated with a relatively energy-intensive process in need of more sustainable strategies for large-scale manufacturing.¹³ The introduction of CNFs has shown very promising results, where an increased viscosity combined with a shear-thinning behavior have enabled the printing of complex 3D shapes.⁷ In addition, CNFs have been reported to have a reinforcing effect by significantly enhancing the compressive properties of alginate hydrogels, tested in dry state.⁹ In a recent study by Siqueira *et al.*, 2019, CNFs were shown to be beneficial for the dimension stability and mechanical properties of alginate-based hydrogels, and the presence of an entangled nanofiber network was observed to affect the pore structures, enhancing their size and thus making them more suitable for cell growth.¹⁴

So far, the approach to achieve a multifunctional and 3D-printed hydrogel has been to add another component, such as CNF. This is accomplished by combining the direct crosslinking ability of the alginate with the shear-thinning behavior of CNF.⁷ However, to derive these two

components from biomass, extensive separation processing is required;^{15,16} in contrast, both alginate and cellulose are naturally found in brown seaweed⁶.

Hence, inspired by a biomimetic approach—that is, the natural design of the cell wall structure—we aim to derive alginate and cellulose together from brown seaweed harvested from North Norway to achieve increased process efficiency and reduced environmental impact and to investigate whether there are any differences regarding the different parts of the seaweed. Both the stipe (stem-like) and blade (leave-like) were disintegrated mechanically for the direct preparation of multifunctional alginate/cellulose nanofiber-based hybrid inks. In addition, a study of their printability and shape fidelity was conducted by printing 3D discs, followed by crosslinking with CaCl_2 to form hydrogels. In the preparation of the hybrid inks, the energy demand, the degree of fibrillation, and the obtained nanostructures were evaluated. The hybrid inks were furthermore compared in terms of how the ratio of alginate/cellulose content affected the nanofibrillation process, the rheological behavior, the 3D structure, and the compressive properties of the printed hydrogels.

EXPERIMENTAL SECTION

Materials. Brown seaweed (*Laminaria digitata*) was kindly provided by The Northern Company Co. (Træna, Norway) and used as the raw material in this study. The contents of the raw material are reported in Supporting Information (Table S1). The seaweed was harvested on the west coast of the North Atlantic Ocean in May 2017. The fresh samples were stored in closed bags in the freezer before use. The stipe and blade of the seaweed were prepared in separate batches for comparison and utilization of the entire structure. Both materials were purified and nanofibrillated using equivalent processing conditions.

Sodium chlorite (NaClO_2), sodium hydroxide (pure pellets, NaOH), and acetic acid (96% CH_3COOH) were purchased from Merck KGaA, Darmstadt, Germany. For ionic crosslinking, calcium chloride of laboratory grade was used ($\text{CaCl}_2 \cdot 2\text{H}_2\text{O}$, 90 mM; from Sigma-Aldrich, Sweden). All chemicals were used as received. Deionized water was used for all experiments.

Direct preparation of hybrid inks. The stipe and blade of the seaweed were left in room temperature ($22 \pm 1^\circ\text{C}$) for about 24 h to defrost; subsequently these were cut into smaller pieces prior to purification by bleaching with NaClO_2 (1.7%) in an acetate buffer (pH 4.5) at 80°C for 2 h. After purification, all color was removed and the material was washed until a neutral pH was reached. The solid recovery was calculated as a yield according to the following equation:

$$\text{Yield (\%)} = W_1/W_0 \times 100 \quad (1)$$

where W_1 indicates the dry weight of the sample after the purification and W_0 denotes the initial dry weight of the seaweed. The presented yields are based on the average of three different batches of each material.

The materials (at a concentration of 2 wt.%) were nanofibrillated using an MKZA6-3 ultrafine friction grinder, Masuko Sangyo® Co., Ltd. (Kawaguchi, Japan) with coarse silica carbide (SiC) grinding stones. The structures were mostly intact after the purification, so the first pass through the Masuko grinder was performed with an open gap (20 μm) to pre-disperse the materials, given that no other dispersing equipment was used. The nanofibrillation was conducted in contact mode, with the gap of the two discs set to $-90 \mu\text{m}$, at 1500 rpm. The prepared hybrid inks were denoted S-A-CNF (stipe–alginate–cellulose nanofibers) and B-A-CNF (blade–alginate–cellulose nanofibers).

The energy consumption of the fibrillation process was established by the direct measurement of the power with a energy analyzer, EM24 DIN, Carlo Gavazzi (Belluno, Italy) and from the monitored processing time. The energy demand was calculated from the product of the power and

the time, and the energy consumption is expressed as kilowatt-hour per kilogram of dry weight of nanofiber. The first sample was collected after the first pass through the Masuko grinder with an open gap. Samples were subsequently collected at regular intervals to assess the degree of fibrillation. The process was finalized when a plateau was reached in the viscosity and no larger structures could be observed by microscope. The prepared inks were degassed and kept in a refrigerator at 6 °C prior to the 3D printing of the hydrogels. To further study the nanofibers and their network formation, seaweed nanofilms were prepared for tensile testing using the solvent casting method, where the dispersions were diluted to 1 wt.% concentration by adding water under magnetic stirring, degassed, and subsequently left to dry in petri dishes for about three days at room temperature (22.6 ± 2 °C).

3D printing of biomimetic hydrogels. Cylindrical discs of S-A-CNF and B-A-CNF were 3D-printed using an INKREDIBLE 3D bioprinter, CELLINK AB, (Gothenburg, Sweden), which is a pneumatic-based extrusion bioprinter. The solid discs (10 mm diameter, 4 mm height, 10 layers) were designed using the CAD software 123D Design (Autodesk) and the created STL files were subsequently converted into g-code using Repetier-Host (Repetier Server) software. A nozzle diameter of 0.5 mm was used at a pressure of 5 kPa and a dosing distance of 0.05 mm. The two ink formulations were 3D-printed directly onto a glass petri dish, then crosslinked in a bath of a 90 mM aqueous solution of CaCl_2 for 30 min directly on the petri dish, and finally washed with deionized water.

Chemical composition. The compositions of the purified stipe and blade were studied in terms of alginate and cellulose content, starting with a dry weight of 10 g. For the isolation of the alginate, the procedure of Zubia *et al.* was followed using the formaldehyde alkali treatment method.¹⁷ The

precipitate was washed with absolute ethanol followed by acetone, prior to drying for 24 h at 40 °C. The alginate fraction was expressed as a percentage of dry weight.

The cellulose content was extracted following a modified method described by Siddhanta *et al.*, 2009.¹⁸ The samples were defatted repeatedly with methanol, placed in a 600 ml NaOH (0.5 M) solution at 60 °C overnight, washed and, dried in room temperature. For the removal of any remaining minerals, the dried material was re-suspended in a 200 ml solution of hydrochloric acid (5% v/v), washed, and dried for 24 h at 40 °C. The cellulose fraction was expressed as a percentage on a dry-weight basis.

Optical microscopy (OM). An optical microscope, Nikon Eclipse LV100N POL (Kanagawa, Japan), and the imaging software NIS-Elements D 4.30 were used to study how the fibrillation process affected the material structure and its micrometer-scale size. Polarized optical microscopy (POM) reference images with a polarization filter were also captured.

Rheological properties. Viscosity measurements were performed during the nanofibrillation process to evaluate the degree of fibrillation, and the process was stopped once a viscosity plateau was reached. A Vibro Viscometer SV-10 from A&D Company, Ltd. (Tokyo, Japan) was used at a constant shear rate and with periodical circulation of the sensor plates from zero to peak (sine-wave vibration) at a frequency of 30 Hz. Because the temperature increased during the nanofibrillation owing to the compression and abrasive shearing forces, the viscosity measurements were repeated at a stabilized temperature of 22.3 ± 1.0 °C to confirm that a viscosity plateau had been reached during the process. The presented values are an average of three measurements for each sample.

The rheological behavior of the hybrid inks, S-A-CNF and B-A-CNF, was further analyzed using a Discovery HR-2 rheometer from TA Instruments (Elstree, UK) at 25 °C. A cone-plate (20 mm)

configuration was used and the shear viscosity was measured at shear rates of $0.01\text{--}1000\text{ s}^{-1}$. Furthermore, the change in moduli while crosslinking the ink was measured with a plate–plate configuration (8 mm, gap 500 μm). Oscillation frequency measurements were conducted at 0.1% strain and a frequency of 1 Hz for 10 min, using oscillation amplitude sweeps to establish the linear viscoelastic region. 50 s after the start of the measurement, a 1 mL drop of a 90 mM CaCl_2 solution was added around the inks, causing gelling while the storage and loss moduli were measured simultaneously.

Atomic force microscopy (AFM). The S-A-CNF and B-A-CNF inks were studied using AFM. The fibrillated sample suspension (0.01 wt.%) was dispersed and deposited by spin coating onto a clean mica surface for imaging. The measurements were performed with a Veeco Multimode Scanning Probe (Santa Barbara, USA) in tapping mode, with a TESPA tip (antimony- (n-) doped silicon), Bruker (Camarillo, USA). The nanofiber size (width) was measured from the height images using the Nanoscope V software, and the average values and deviations presented here are based on 50 different measurements. All measurements were conducted in air at room temperature.

Mechanical properties. The prepared nanofilms were tested using conventional tensile testing to provide an indication of the degree of fibrillation. Prior to mechanical testing, the density was calculated using a gravimetric method: an analytic balance was used to determine the weight and a micrometer gauge was used to measure the thickness based on an average of 10 different measurements per material. The sample preparation and the tensile testing procedure have been reported in our previous study.¹⁹ A tensile testing system (AG X; Shimadzu, Japan) equipped with a 1 kN load cell was used at an extension rate of 2 mm/min and with a gauge length of 20 mm. All samples were conditioned at $50 \pm 2.0\%$ relative humidity at $22.1 \pm 1.0\text{ }^\circ\text{C}$ for at least 48 h. The results are averages of at least 10 sets of measurements for each material.

Scanning electron microscopy (SEM). The cross-sections of the stipe and blade raw material were observed using a SEM system (JSM-IT300LV, Tokyo, Japan) at an acceleration voltage of 15 kV to study their microstructures. In addition, the cross-sections of the nanofilms were observed. All samples were coated using a sputter-coater machine (Leica EM ACE200, Austria) with a gold target to prevent electron charging. The coating was performed in a vacuum of approximately 6×10^{-5} mbar under a current of 100 mA for 20 s to obtain a coating thickness of 10 nm.

Compression properties. Uniaxial unconfined compression tests of the 3D printed and crosslinked hydrogels were carried out using a dynamic mechanical analyzer (DMA Q800, TA Instruments, New Castle, USA) at 25 °C. The hydrogels were preloaded using a load of 0.05 N and subsequently compressed up to a strain of 100% and at a strain rate of $10\% \text{ min}^{-1}$. The materials were compared according to the stress and tangent modulus at compressive strain levels of 30% and 60%, respectively. The discs were tested six times for each material; the average results are reported.

X-ray microtomography. The 3D internal architecture of the natural structures after purification, as well as the reassembled nanostructures after fibrillation, 3D printing, and crosslinking, were reconstructed from the stipe and blade, respectively. The samples were frozen at a temperature of approximately -20 °C for at least 24 h; then, they were freeze-dried for 48 h at a temperature of -40 °C using a freeze-dryer (Alpha 2-4 LD plus, CHRIST GmbH, Osterode am Harz, Germany). Samples of approximate size $4 \times 4 \times 4 \text{ mm}^3$ were scanned using a Zeiss Xradia 510 Versa (Carl Zeiss, Pleasanton, CA, USA) with a $20\times$ objective, which performed interior tomography with a field of view of 0.56 mm and voxel size of $0.56 \text{ }\mu\text{m}$. The scanned region of interest was positioned at the exact center of each aerogel sample. The scanning was carried out

with an X-ray tube voltage of 50 kV, an output power of 4 W, and without any X-ray filters. A total of 2401 projections were acquired with an exposure time of 6 s, which resulted in a total scan time of 6 h. The tomographic reconstruction was carried out using filtered back-projection with Zeiss Scout-and-Scan Reconstructor software (version 11.1). The 3D visualization and analysis of the microstructure in the aerogels were obtained using Dragonfly Pro Software (ORS).

RESULTS AND DISCUSSION

Purification and characterization of raw material. The yield and chemical composition after the purification of the raw materials is presented in Table 1.

Table 1. Corresponding sample code of raw materials and their yields, as well as their cellulose and alginate content after the purification.

Raw materials	Initial weight [g]	Bleached weight [g]	Total yield [%]	Cellulose [wt.%]	Alginate [wt.%]	Sample code
Stipe	70	50	71 ± 8	33 ± 6	45 ± 13	S-A-CNF
Blade	70	52	74 ± 7	23 ± 3	46 ± 11	B-A-CNF

The objective of the purification of the seaweed was to remove the pigment and other impurities while maintaining as much of the inherently high alginate content in brown seaweed, together with the cellulose content. Indeed, the yield of the stipe and blade were as high as 71% and 74%, respectively, after the bleaching procedure (Table 1); these yields are comparable to that of wood after direct bleaching (namely, about 70%), which is mainly composed of holocellulose.

An alginate content of 25–30 wt.% and cellulose content of 10–15 wt.% have previously been reported for raw *Laminaria Digitata* seaweed harvested in Scotland during May.²⁰ From Table 1, after the purification, the alginate and cellulose contents were higher, but their relative percentages

were maintained. The stipe had a higher cellulose content, although both structures showed similar alginate content. However, the standard deviations were high, which might reflect the heterogeneity of the raw material even within a species.²¹ Only a limited number of studies have measured the compositional content of the different parts of brown seaweed, and for *Laminaria Digitata* harvested in Scotland, a cellulose content of 6–8 wt.% and 3–5 wt.% have been reported for the stipe and the blade, respectively.⁴ However, the composition of seaweed is highly dependent on factors such as the measuring methods, geography, season, and age²⁰.

Nanofibrillation process and characterization of hybrid inks. Viscosity measurements and OM were used to study the degree of fibrillation throughout the process. A plateau in the viscosity curve indicated strong gel formation by the separated nanofibers with a high aspect ratio, and the microscopy measurements confirmed the absence of intact larger structures at the end of the process. The viscosity measured at room temperature as a function of the energy demand is shown in Figure 1 and the route from the raw materials to the hybrid inks is shown in Figure 2.

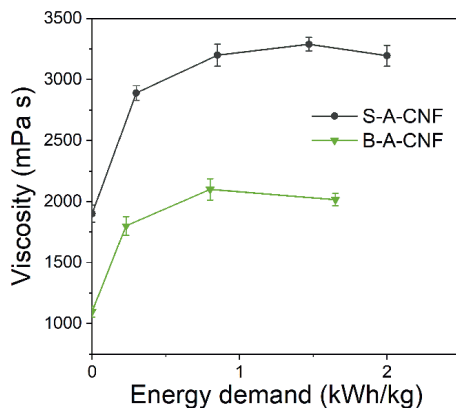


Figure 1. Measured viscosity as a function of the energy consumption during the nanofibrillation process for the preparation of S-A-CNF and B-A-CNF.

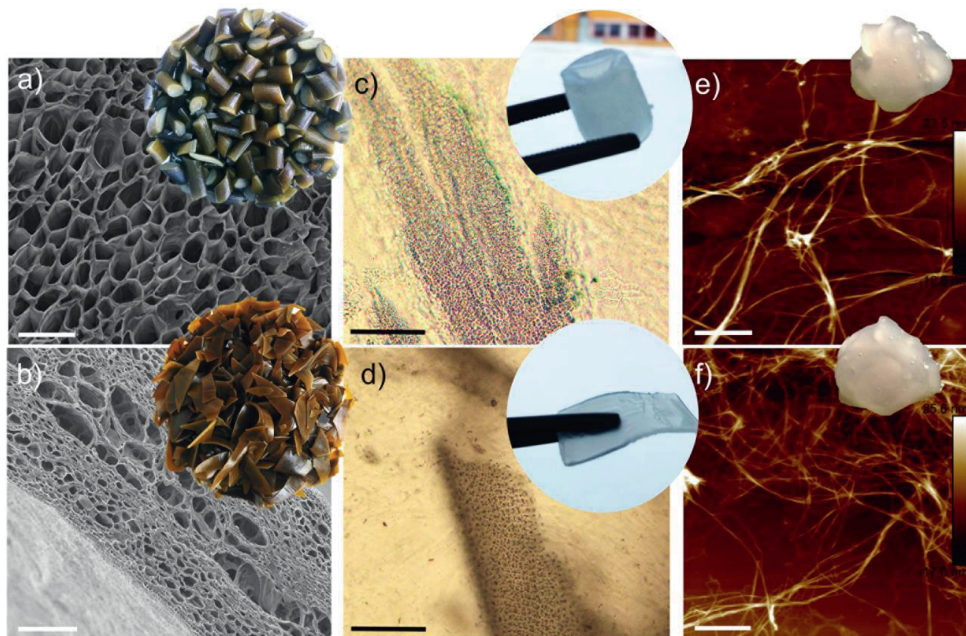


Figure 2. Microstructure of (a) stipe and (b) blade raw material (scale bar: 100 μm); OM after purification of (c) stipe and (d) blade, inset: photographs of the purified stipe and blade, respectively (scale bar: 200 μm); AFM height images of (e) S-A-CNF and (f) B-A-CNF (scale bar: 600 nm), inset: photographs of the hybrid-inks from stipe and blade, respectively.

An increased viscosity and a plateau are clearly observed for both S-A-CNF and B-A-CNF, as shown in Figure 1. For comparison, commercially bleached kraft wood pulp nanofibrillated with an equivalent technique has a significantly lower viscosity plateau at 1565 mPas²⁴. In previous work on the nanofibrillation process for wood pulp, the viscosity was used as an indication of the degree of fibrillation during the process, where the viscosity plateau signified the formation of a strong network of separated nanofibers.^{22,24} Remarkably, the formation of this network of separated cellulosic nanofibers was possible to detect throughout the nanofibrillation process, despite the high amount of non-cellulosic components, such as alginate.

A more organized structure was observed for the stipe (Figure 2a) compared with the more layer-like structure of the blade (Figure 2 b), which displayed a wide range of cell sizes. The brownish/greenish color of the raw materials (inset Figure 2 a,b), appeared to have been removed from the mainly intact structures after the purification process, which are displayed as translucent white hydrogel structures (inset Figure 2 c, d). After purification, thinner layers of the intact structures were visualized under OM (Figure 2 c, d). After the nanofibrillation process, no visible larger structures appeared intact from neither OM, nor POM (Figure S1). The nanofibrillation of the stipe reached a maximum viscosity at an energy demand of 1.5 kWh/kg (Figure 1). In comparison, the blade had a slightly lower energy demand throughout the process, and the maximum viscosity was measured at an energy demand of 1.0 kWh/kg. The slightly higher energy demand of the stipe could be explained by its higher cellulose content (Table 1), which might require more energy to be separated. In addition, the arrangement of cellulose and alginate in the different parts and cell wall structures likely influence the ease of separation. From Figure 2 (e, f), nanofibers were successfully separated from both the stipe and the blade, appearing as gels after the separation (inset), and their dimensions were on average 7 ± 3 nm and 6 ± 3 nm, respectively. Their size distribution is provided in Figure S2. The measured energy consumptions were remarkably low for the nanofibrillation of both seaweed structures and comparable to that of carrot residue¹⁹ (namely, 0.9 kWh/kg); meanwhile, commercially bleached wood kraft pulp reached a maximum viscosity at 8.4 kWh/kg for a similar processing approach²⁴. The importance of the presence of hemicellulose on the nanofibrillation process of wood pulp have previously been studied using ultrafine grinding.²³ The low energy demand suggests that the presence of alginate during nanofibrillation may also be beneficial for the separation of nanofibers.

The seaweed nanofibers were further solvent-casted for the preparation of seaweed nanofilms to evaluate the mechanical properties of the network and provide an indication of the degree of fibrillation. Photographs and microscopy images of the seaweed nanofilms are shown in Figure 3.

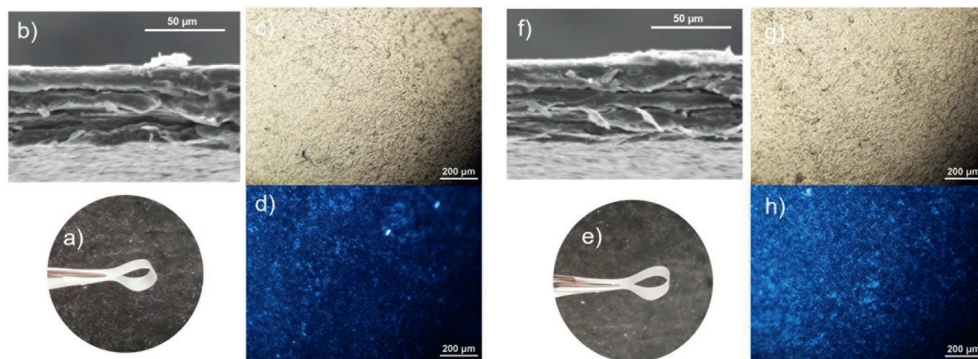


Figure 3. B-A-CNF film: a) photograph, b) OM image of surface, c) POM image of surface, d) SEM image of cross-section. S-A-CNF film: e) photograph, f) SEM image of cross-section, g) OM image of surface, h) POM image of surface.

The seaweed nanofilms were further characterized in terms of density and mechanical properties, which are listed in Table 2.

Table 2. Properties of the S-A-CNF and B-A-CNF nanofilms.

Nanofilms	E-modulus [GPa]	Strength [MPa]	Strain at break [%]	Density [g/cm ³]
S-A-CNF	11.2 ± 1.2	167.5 ± 9.1	2.3 ± 0.6	1.3 ± 0.4
B-A-CNF	9.6 ± 0.9	143.1 ± 10.0	1.7 ± 0.3	1.2 ± 0.3

Figure 3 shows transparent films (a) with an even surface, where no intact structures or agglomeration could be observed (b, c, g, h). The cross-sections of both films displayed a structure

of distinct layers (d, f). A layered structure is typically found in nanofiber networks²⁴; however, the nanofibers appeared embedded in the alginate and no stacked fibers were visible.

The representative stress–strain curves from the uniaxial tension tests of the films after the nanofibrillation process are provided in Supporting Information (Figure S3). Both seaweed nanofilms showed a high modulus and strength, but low strain to break, indicating a successful nanofibrillation, allowing a strong network formation. It has been reported that the addition of CNFs increases the strength and modulus but decreases the strain and flexibility of CaCl₂-crosslinked alginate films.²⁵ Furthermore, by increasing the CNF content in the films from 1% to 15%, the strength was further increased by 35%. Another study that combined CNF (at 90%) and alginate (at 10%) films with CaCl₂ crosslinking, reported the formation of an interpenetrating network, which was further locked by ionic crosslinking into a tough material both in the wet and the dry states.²⁶ S-A-CNF displayed about 15% higher E-modulus and 16% higher strength than B-A-CNF. This could be attributed to the higher cellulose content of S-A-CNF, thus rendering a higher CNF loading.

The mechanical properties of the seaweed nanofilms shown in Table 2 are comparable to those of commercially extracted alginate with added CNF, which has a strength of 100 MPa, and a strain of about 1.5%, though with a higher modulus of 17–18 GPa.²⁵ It should be noted that these films were crosslinked with CaCl₂, which has been previously shown to significantly enhance the mechanical properties of films²⁷.

3D printability and characterization of biomimetic hydrogels. The rheological behavior of the hybrid inks was studied to evaluate their suitability for 3D printing and the results are shown in Figure 4.

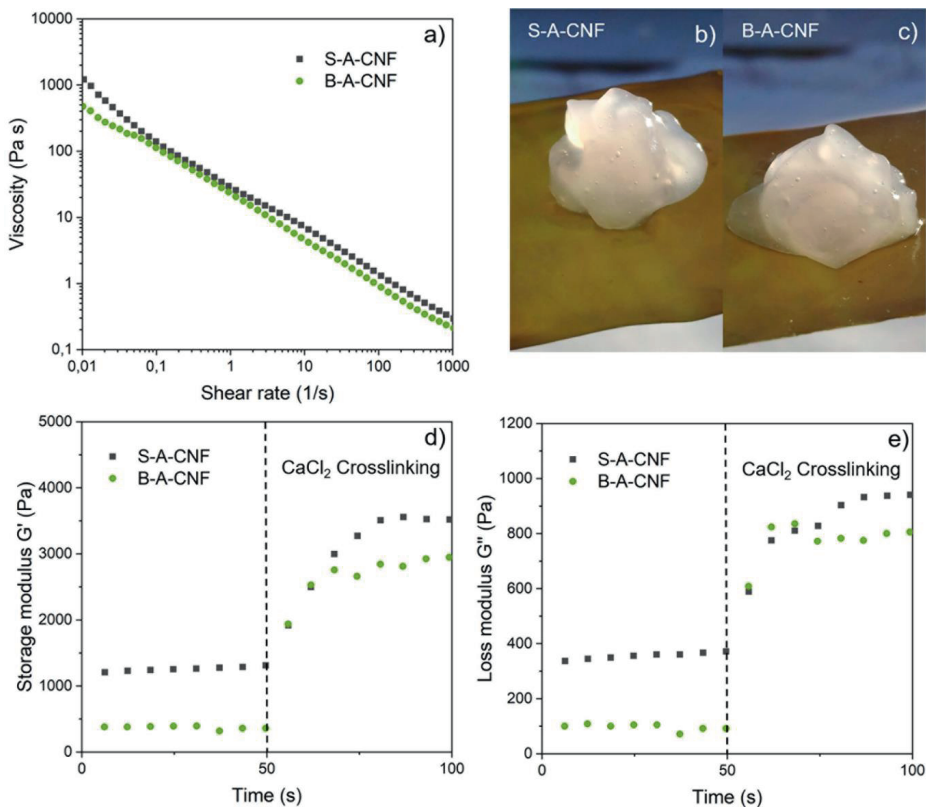


Figure 4. Rheological data of the hybrid inks: (a) viscosity as a function of shear rate, (b, c) photographs of the hybrid-ink gels at 2 wt.%, (d) storage modulus G' , and (e) loss modulus G'' measured over time, where the CaCl_2 solution was added 50 s after the measurement was started.

In Figure 4 (a) a shear-thinning behavior is observed for both the S-A-CNF and B-A-CNF inks, similar to that seen in viscosity graphs previously reported for commercial alginate mixed with CNF⁹ and for pure CNF⁷. For S-A-CNF, the initial viscosity was 1224 Pa s and it decreased to 0.3 Pa s upon increasing the shear rate to 1000 s^{-1} . In comparison, the viscosity of B-A-CNF was initially lower at 578 Pa s and dropped to 0.2 Pa s at a shear rate of 1000 s^{-1} . In addition, the higher viscosity of S-A-CNF can be seen in Figure 4 (b), which displays a more stable gel formation than

that of B-A-CNF, shown in (c). These results are in agreement with the viscosity measurements performed to indicate the degree of fibrillation.

The high viscosity at low shear rates and the shear-thinning behavior with increasing shear rate provide shape fidelity during printing; however, to maintain structural integrity after printing, crosslinking of the alginate is required. Hence, the gelling behavior of the hybrid inks was studied by measuring the loss and storage moduli as a function of time while crosslinking with CaCl_2 (Figure 4 d & e). Both the storage modulus (d) and the loss modulus (e) displayed an instant increase upon the addition of a CaCl_2 solution at 50 s and became gradually linear after an additional 50 s. The time was measured for an additional 5 min to confirm this plateau. The higher storage modulus of S-A-CNF reflects a higher degree of crosslinking and results in an increased strength or rigidity.

3D-printability and crosslinking enable the use of inks in a wide range of applications that, for example, require specific shapes for wound dressing²⁸ or even for 3D printing of living tissues and organs⁷. The printability and stability of 3D discs of S-A-CNF and B-A-CNF inks prepared at 2 wt.% solid content were studied, and the printing parameters were tuned through a trial-and-error method. Both hybrid inks could be printed without collapse of the structure. However, a minor shrinkage and some swelling at the center, appearing as a slightly convex surface, were observed after crosslinking of the discs. These tendencies of shape deformation after CaCl_2 crosslinking have previously been reported for 3D-printed alginate/CNF hydrogels.^{7,28} This behavior might reflect inadequate homogeneity of the diffusion-based CaCl_2 crosslinking approach. Ionic crosslinking of alginate using CaCl_2 has been widely studied. By varying parameters such as the crosslinking ratio²⁹ and the crosslinking time³⁰, the mechanical properties of printed hydrogels can be tuned. Other factors such as the molecular weight and the M/G ratio are related to the raw

material and its alginate extraction process. These factors have a large influence both on the crosslinking behavior and the fundamental mechanical behavior of the hydrogels.⁵ The 3D-printed S-A-CNF and B-A-CNF hydrogels were evaluated under compression to determine their mechanical properties after crosslinking, as presented in Figure 5.

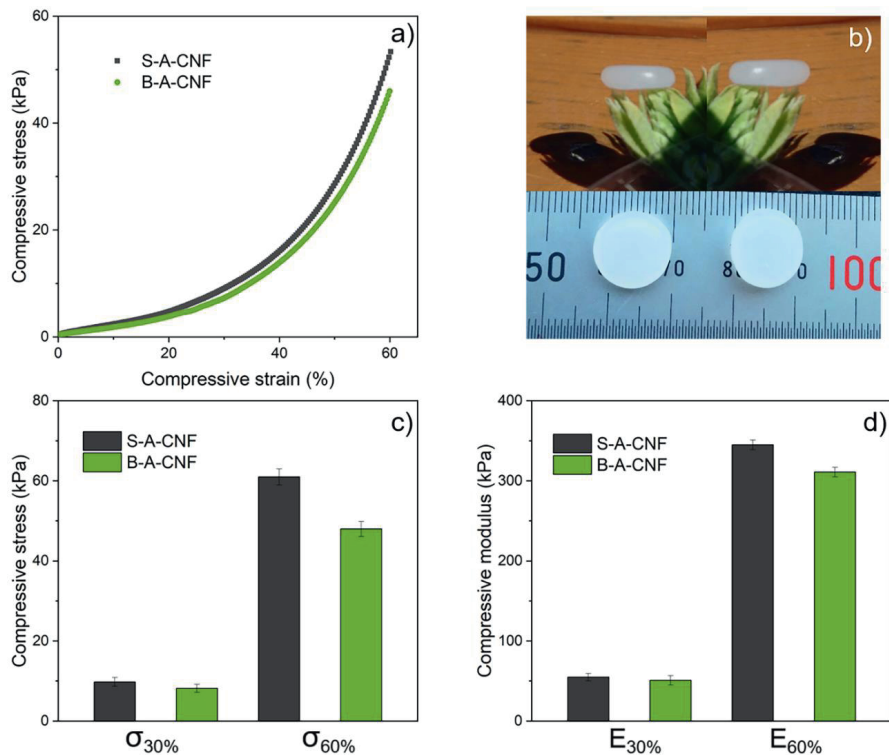


Figure 5. (a) Representative compressive stress–strain curves for a strain up to 60%, (b) photographs of the hydrogels after crosslinking, (c) compressive strength, and (d) compressive modulus at 30 and 60% strain.

Because the compressive stress and strain curves revealed a viscoelastic non-linear stress–strain behavior, the compressive modulus and strength at 30 and 60% strain were used for mechanical

characterization (Figure 5a) of the 3D-printed hydrogels (b). From (c) and (d), S-A-CNF shows generally better compressive properties than B-A-CNF. This is in good agreement with the rheological behavior of the gels and could be explained by the higher amount of CNF in S-A-CNF reinforcing the structure. However, the stiffness of alginate hydrogels is directly related to their crosslinking, and S-A-CNF with a relatively lower amount of alginate than B-A-CNF; displayed a higher stiffness, as seen from Figure 5(d).

In *Laminara digitata*, a higher amount of alginate rich in guluronic acid (G), instead of mannuronic acid (M), was previously shown for the stipe than that of the blade of the seaweed⁶; therefore, the stipe has a lower M/G ratio. Alginates with lower M/G ratio are known to display a higher affinity to crosslinking (mechanical rigidity), and the gel strength of the alginate is mainly dependent on the content and length of G.³¹ A lower M/G ratio of the alginate in the S-A-CNF hydrogel than that of B-A-CNF may further contribute to the higher compressive properties of the former, in particular, its stiffness.

It is also notable that the maximum compressive strength was measured at around 80% strain for the B-A-CNF hydrogel (175.2 ± 3 kPa), shown in the compressive graphs (Figure S4a). At this strain, the B-A-CNF hydrogel fractured while the S-A-CNF hydrogel was only compressed, without any visual fractures (Figure S4b). The alginate of the S-A-CNF ink and its CNF content appeared to assemble into a biomimetic hydrogel with high compressive stiffness and strength, but highly flexible.

The direct preparation method used in this study limits the tuning of the mechanical properties of the hydrogels by altering the ratio of the two components, alginate and CNF, and establishing their separate contributions. However, the influence of factors such as the concentration of the solid content and CaCl_2 has previously been shown to be highly effective for tailoring the

mechanical behavior of the hydrogels.³² Commercial alginate with a dry content of 2 wt.%, crosslinked with a 50 mM CaCl_2 solution for hydrogel formation (compared to 90 mM used in this study), displayed a compressive strength and modulus of 25 and 32 kPa, respectively, at 60% strain. Moreover, it was shown that these values could be improved to some extent by increasing the solid content and CaCl_2 concentration. From Figure 5 (c, d), the strength and modulus of the S-A-CNF hydrogel are 345 and 61 kPa, respectively, at the same strain, signifying a contribution from entangled CNF network. The compressive properties imply that the alginate of the hybrid inks has an inherently favorable mechanical behavior and crosslinking ability, which could be further explored and utilized to adjust its mechanical properties.

To study the morphology of the natural seaweed structure after purification in comparison with the nanofibrillated and reassembled hydrogel structure after crosslinking, the samples were imaged using X-ray microtomography, as shown in Figure 6.

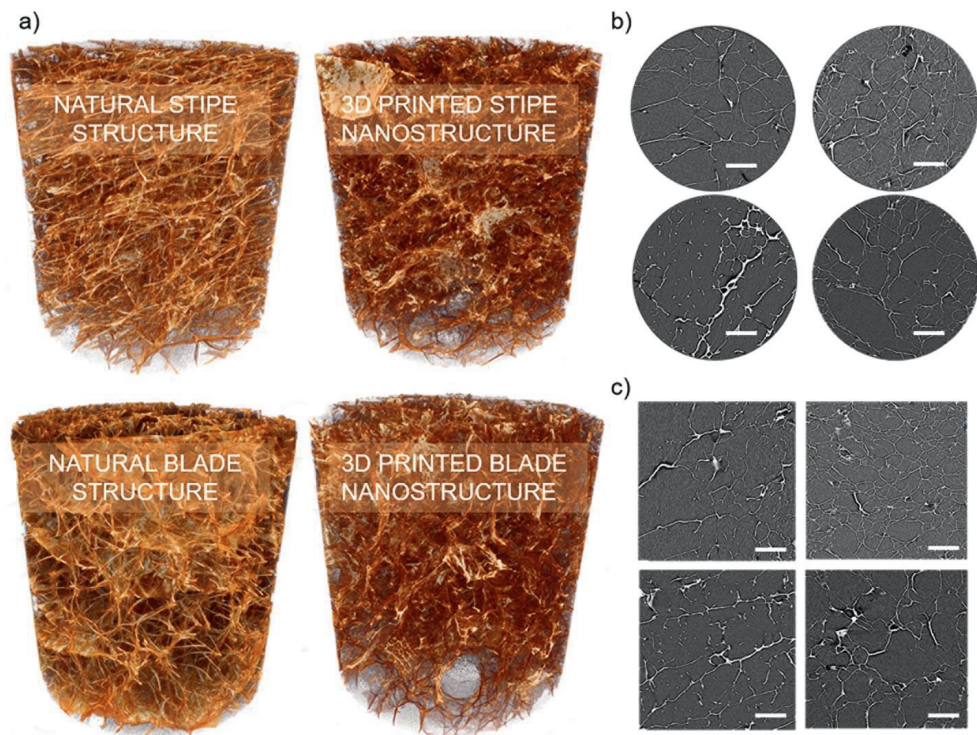


Figure 6. a) X-ray microtomography 3D reconstruction of the structure of natural seaweed after purification and of the nanofibrillated, 3D-printed, and crosslinked structures derived from the seaweed stipe and blade. b) Horizontal slice of the 3D reconstruction (circular) and c) longitudinal slice of the 3D reconstruction (square). The scale bar corresponds to 100 μm .

The addition of CNFs has been reported to contribute to the formation of a more favorable structure for cell growth by favoring a web-like structure with larger pores ranging from 40 to 150 μm .¹⁴ As observed in the 3D reconstruction of Figure 6 (a), as well as in the 2D slices (Figure 6 b, c), the nanofibrillation of the cellulosic part of the seaweed into CNFs promoted the formation of an interconnected network structure upon reassembling, compared to that of the natural structure.

The natural structures were intact in the form of natural hydrogels after the purification, as shown in Figure 2 (e & f). After freeze-drying, both the stipe and the blade displayed a porous structure, where the layered structure of the raw blade material observed by SEM (Figure 2b) was apparent also after the purification (Figure 6 a–c). The 3D-printed hydrogels displayed open interconnected pores with a wide range of pore diameters of 10–150 μm and 20– 200 μm for the stipe and the blade, respectively.

CONCLUSION

This paper reports on a direct method to prepare alginate/CNF hybrid inks with a rheological behavior suitable for 3D printing from seaweed. Both the hybrid inks prepared from the stipe (S-A-CNF) and the blade (B-A-CNF) of the seaweed displayed a shear-thinning behavior and could be reassembled using the extrusion-based 3D-printing technique. Furthermore, the developed hybrid inks were sufficiently crosslinked with CaCl_2 to formulate mechanically robust biomimetic hydrogels. The S-A-CNF ink had a higher CNF/alginate ratio than B-A-CNF and demonstrated a higher viscosity and better compressive properties. Purification followed by energy-efficient nanofibrillation provided a direct preparation method of a multifunctional material, where the crosslinking ability of the alginate with the shear-thinning behavior of the CNF were combined in the formulated hybrid inks. Moreover, the presence of alginate appeared to be beneficial for an energy-efficient nanofibrillation process, further promoting the use of seaweed as a source of raw material. Our results demonstrate the potential use of a direct, efficient, and upscalable approach for the preparation of alginate/CNF hybrid inks instead of employing separate methods to extract and combine the materials to achieve 3D printability; thus, our method could be considered as a green alternative to current extraction approaches. We conclude that the hybrid inks are suitable

for the 3D printing of hydrogels that have a favorable mechanical behavior after crosslinking and a promising open interconnected network structure applicable to a wide range of applications. Further work on the shape fidelity of more complex shapes, the effect of solid contents, the crosslinking degree, as well as bioprinting with living cells and cell viability is needed for the use of these hybrid inks, for example, as bioinks in 3D bioprinting of soft tissue.

SUPPORTING INFORMATION

Raw material content; OM, POM, and photographs of the materials after purification and after fibrillation; nanofiber size distribution of the hybrid inks; stress and strain curves from tensile testing of nanofilms; compressive stress and strain curves from testing of the 3D-printed and CaCl_2 -crosslinked hydrogels and photographs of the hydrogel samples after the compression test.

ACKNOWLEDGEMENT

The authors acknowledge the financial support of the European Regional Development Fund under the Interreg Nord: Sea-Surf-Snow (project no: 20201287); Bio4Energy—a strategic research environment, appointed by the Swedish government and Kempe Foundations for the use of AFM and X-ray microtomography. Lucas Gerardin and Boris Valldecabres are acknowledged for their work on the preparation of the nanofilms.

REFERENCES

- (1) FAO (2019). FAO yearbook. Fishery and Aquaculture Statistics 2017. Food and Agriculture Organization of the United Nations. Rome, 2019.
- (2) Misurcova, L. In *handbook of marine macroalgae: biotechnology and applied phycology*, 1st ed.; Se-Kwon, K., Eds.; JohnWiley & Sons, Ltd.: New Delhi, India, 2012; p 181-182.
- (3) Manns, D.; Nielsen, M. M.; Bruhn, A.; Saake, B.; Meyer, A. S. Compositional variations of brown seaweeds *Laminaria digitata* and *Saccharina latissima* in Danish waters. *J. Appl. Phycol.* **2017**, *29* (3), 1493-1506.
- (4) Black, W. A. P. The seasonal variation in the cellulose content of the common Scottish Laminariaceae and Fucaceae. *J. Mar. Biol. Assoc. U. K.* **1950**, *29* (2) 379-387.
- (5) Abdul Khalil, H. P. S.; Lai, T. K.; Tye, Y. Y.; Rizal, S.; Chong, E. W. N.; Yap, S. W.; Hamzah, A. A.; Nural Fazita, M. R.; Paridah, M. T. A review of extractions of seaweed hydrocolloids: properties and applications. *EXPRESS Polym. Lett.* **2018**, *12*(4), 296–317.
- (6) Peteiro, C. In *alginates and their biomedical applications*, Rehm, B.; Moradali, M. Eds.; Springer Series in Biomaterials Science and Engineering vol 11; Springer, Singapore, 2017; p 27-58.
- (7) Markstedt, K.; Mantas, A.; Tournier, I.; Martínez Ávila, H.; Hägg, D.; Gatenholm, P. 3D bioprinting human chondrocytes with nanocellulose–alginate bioink for cartilage tissue engineering applications. *Biomacromolecules* **2015**, *16*, 1489– 1496.

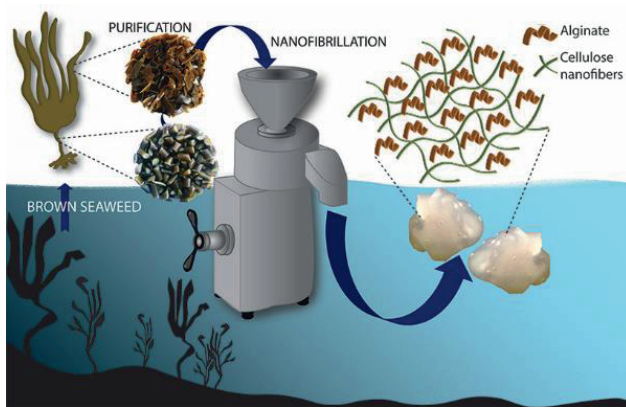
- (8) Naseri, N.; Deepa, B.; Mathew, A. P.; Oksman, K.; Girandon, L. Nanocellulose-based interpenetrating polymer network (IPN) hydrogels for cartilage applications. *Biomacromolecules* **2016**, *17* (11), 3714-3723.
- (9) Abouzeid, R. E.; Khiari, R.; Beneventi, D.; Dufresne, A. Biomimetic mineralization of three-dimensional printed alginate/TEMPO-oxidized cellulose nanofibril scaffolds for bone tissue engineering. *Biomacromolecules* **2018**, *19* (11), 4442-4452.
- (10) García-Astrain, C.; Avérous, L. Synthesis and evaluation of functional alginate hydrogels based on click chemistry for drug delivery applications. *Carbohydr. Polym.* **2018**, *190*, 271-280.
- (11) Kong, H. J.; Lee, K. Y.; Mooney, D. J.; Decoupling the dependence of rheological/mechanical properties of hydrogels from solids concentration. *Polymer* **2002**, *43* (23), 6239-6246.
- (12) Chinga-Carrasco, G. Potential and limitations of nanocelluloses as components in biocomposite inks for three-dimensional bioprinting and for biomedical devices. *Biomacromolecules* **2018**, *19* (3), 701-711.
- (13) Falsini, S.; Bardi, U.; Abou-Hassan, A.; Ristori, S. Sustainable strategies for large-scale nanotechnology manufacturing in the biomedical field. *Green Chem.* **2018**, *20*, 3897-3907.
- (14) Siqueira, P.; Siqueira, É.; de Lima, A. E.; Siqueira, G.; Pinzón-Garcia, A. D.; Lopes, A. P.; Cortés Segura, M. E.; Isaac, A.; Vargas Pereira, F.; Botaro, V. R. Three-dimensional stable alginate-nanocellulose gels for biomedical applications: towards tunable mechanical properties and cell growing. *Nanomaterials* **2019**, *9* (1), 78-100.

- (15) Sadhukhan, J.; Gadkari, S.; Martinez-Hernandez, E.; Ng, K. S.; Shemfe, M.; Torres-Garcia, E.; Lynch, J. Novel macroalgae (seaweed) biorefinery systems for integrated chemical, protein, salt, nutrient and mineral extractions and environmental protection by green synthesis and life cycle sustainability assessments. *Green Chem.* **2019**, *21*, 2635- 2655.
- (16) Nascimento, D. M.; Nunes, Y. L.; Figueirêdo, M. C. B.; de Azeredo, H. M. C.; Aouada, F. A.; Feitosa, J. P. A.; Rosa, M. F.; Dufresne, A. Nanocellulose nanocomposite hydrogels: technological and environmental issues. *Green Chem.* **2018**, *20*, 2428-2448.
- (17) Zubia, M.; Payri, C.; Deslandes, E. Alginate, mannitol, phenolic compounds and biological activities of two range-extending brown algae, *Sargassum mangarevense* and *Turbinaria ornata* (Phaeophyta: Fucales), from Tahiti (French Polynesia). *J. Appl. Phycol.* **2008**, *20*, 1033–1043.
- (18) Siddhanta, A. K.; Prasad, K.; Meena, R.; Prasad, G.; Mehta, G. K.; Chhatbar, M. U.; Oza, M. D.; Kumar, S.; Sanandya, N. Profiling of cellulose content in Indian seaweed species. *Bioresour. Technol.* **2009**, *100*, 6669–6673.
- (19) Berglund, L.; Noël, M.; Aitomäki, Y.; Öman, T.; Oksman, K. Production potential of cellulose nanofibers from industrial residues: efficiency and nanofiber characteristics. *Ind. Crop. Prod.* **2016**, *92*, 84-92.
- (20) Schiener, P.; Black, K. D.; Stanley, M. S.; Green, D. H. The seasonal variation in the chemical composition of the kelp species *Laminaria digitata*, *Laminaria hyperborea*, *Saccharina latissima* and *Alaria esculenta*. *J. Appl. Phycol.* **2015**, *27*, 363–373.

- (21) Manns, D.; Deutschle, A. L.; Saake, B.; Meyer, A. S. Methodology for quantitative determination of the carbohydrate composition of brown seaweeds (Laminariaceae). *RSC Adv.* **2014**, *4*, 25736- 25746.
- (22) Lahtinen, P.; Liukkonen, S.; Pere, J.; Sneek, A.; Kangas, H. A comparative study of fibrillated fibers from different mechanical and chemical pulps. *Bioresources* **2014**, *9*, 2115–2127.
- (23) Iwamoto, S.; Abe, K.; Yano, H. The effect of hemicelluloses on wood pulp nanofibrillation and nanofiber network characteristics. *Biomacromolecules* **2008**, *9* (3), 1022-1026.
- (24) Berglund, L.; Anugwom, I.; Hedenström, M.; Aitomäki, Y.; Mikkola, J. P.; Oksman, K. Switchable ionic liquids enable efficient nanofibrillation of wood pulp. *Cellulose* **2017**, *24*, 3265-3279.
- (25) Sirviö, J. A.; Kolehmainen, A.; Liimatainen, H.; Niinimäki, J.; Hormi, E. O. Biocomposite cellulose-alginate films: Promising packaging materials. *Food Chem.* **2014**, *151*, 343-351.
- (26) Benselfelt, T.; Engström, J.; Wågberg, L. Supramolecular double networks of cellulose nanofibrils and algal polysaccharides with excellent wet mechanical properties. *Green Chem.* **2018**, *20*, 2558-2570.
- (27) Liling, G.; Di, Z.; Jiachao, X.; Xin, G.; Xiaoting, F.; Qing, Z. Effects of ionic crosslinking on physical and mechanical properties of alginate mulching films. *Carbohydr. Polym.* **2016**, *136*, 259-265.

- (28) Leppiniemi, J.; Lahtinen, P.; Paajanen, A.; Mahlberg, R.; Metsä-Kortelainen, S.; Pinomaa, T.; Pajari, H.; Vikholm-Lundin, I.; Pursula, P.; Hytönen, V. P. 3D-printable bioactivated nanocellulose–alginate hydrogels. *ACS Appl. Mater. Interfaces* **2017**, *9* (26), 21959-21970.
- (29) Freeman, F. E.; Kelly, D. J. Tuning alginate bioink stiffness and composition for controlled growth factor delivery and to spatially direct MSC fate within bioprinted tissues. *Scientific Reports* **2017**, *7* (17042), 1-12.
- (30) Di Giuseppe, M.; Law, N.; Webb, B.; Macrae, R. A.; Liew, L. J.; Sercombe, T. B.; Dilley, R. J.; Doyle, B. J. Mechanical behaviour of alginate-gelatin hydrogels for 3D bioprinting. *J. Mech. Behav. Biomed. Mater.* **2018**, *79*, 150-157.
- (31) Lee, K. Y.; Mooney, D. J. Alginate: properties and biomedical applications. *Prog. Polym. Sci.* **2012**, *37* (1), 106-126.
- (32) Nunamaker, E. A.; Otto, K. J.; Kipke, D. R. Investigation of the material properties of alginate for the development of hydrogel repair of dura mater. *J. Mech. Behav. Biomed. Mater.* **2011**, *79*, 150-157.

Table of Contents Graphic



Supporting Information

Direct preparation of alginate/cellulose nanofiber hybrid-ink from brown seaweed for 3D biomimetic hydrogels

Linn Berglund,[†] Fredrik Forsberg,[†] Kristiina Oksman^{,†,§,||}*

[†] Department of Engineering Sciences and Mathematics, Luleå University of Technology, 97187, Luleå, Sweden

[§] Fibre and Particle Engineering, University of Oulu, Oulu, Finland

^{||} Mechanical & Industrial Engineering, University of Toronto, Canada

Table S1 Content for 100g of brown seaweed blades provided by the supplier The Northern Company.

Content	100g
Fat	<0.5g
Carbohydrate	5.9g
Fiber	6.4g
Protein	1.6g
Salt	1.8g
Potassium	0.78g
Calcium	0.19g
Magnesium	0.13g
Iodine	0.041g

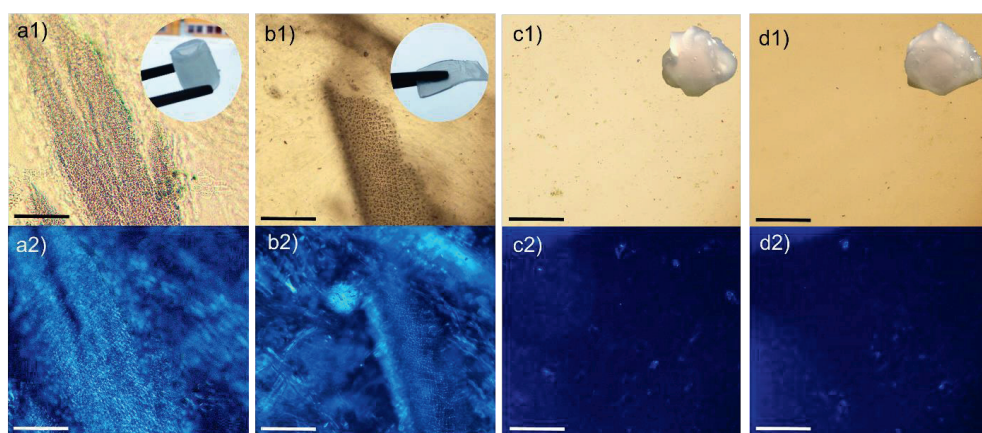


Figure S1. OM and POM of the stipe a1), a2), and blade b1), b2), respectively, and inset photograph after purification. OM and POM of the stipe c1), c2), and blade d1), d2), respectively and inset photograph of the gel, after the nanofibrillation.

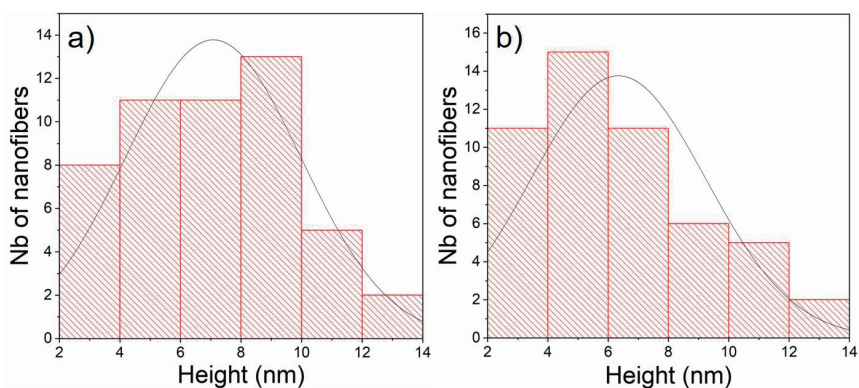


Figure S2. Nanofiber size distribution measured from AFM height images from a) S-A-CNF, and b) B-A-CNF.

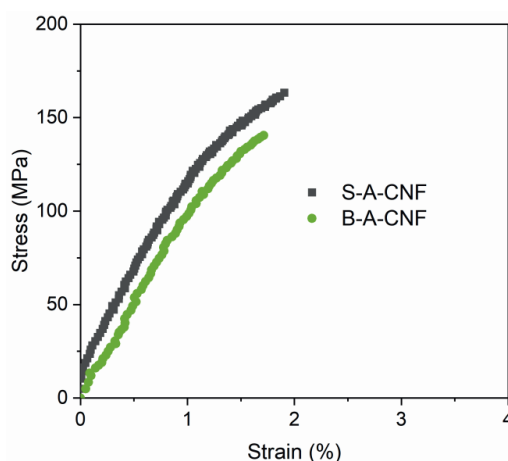


Figure S3. Stress and strain curves from tensile testing of the nanofilms prepared from the stipe-alginate-cellulose nanofiber (S-A-CNF), and blade-alginate-cellulose nanofiber (B-A-CNF) samples after purification and nanofibrillation.

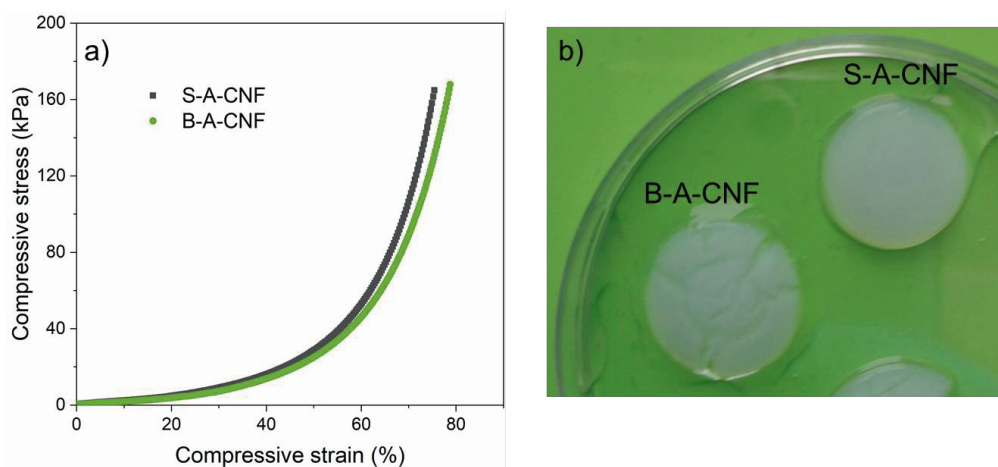


Figure S4. a) Compressive stress and strain curves from testing of the 3D printed and CaCl_2 crosslinked hydrogels, from the stipe-alginate-cellulose nanofiber (S-A-CNF), and blade-alginate-cellulose nanofiber (B-A-CNF) hybrid-inks, b) photographs of the hydrogels samples after compression test.

PAPER 4

Promoted hydrogel formation of lignin-containing arabinoxylan aerogel using cellulose nanofibers as a functional biomaterial

Berglund L., Forsberg F., Jonoobi M., Oksman K.

RSC Adv., 8 (2018) 38219–38228

doi:10.1039/C8RA08166B


 Cite this: *RSC Adv.*, 2018, **8**, 38219

Promoted hydrogel formation of lignin-containing arabinoxylan aerogel using cellulose nanofibers as a functional biomaterial†

 Linn Berglund,^a Fredrik Forsberg,^{ib} Mehdi Jonoobi^{ca} and Kristiina Oksman^{ib}*^{ad}

In this work, three-dimensional (3D) aerogels and hydrogels based on lignin-containing arabinoxylan (AX) and cellulose nanofibers (CNF) were prepared. The effects of the CNF and the crosslinking with citric acid (CA) of various contents (1, 3, 5 wt%) were evaluated. All the aerogels possessed highly porous (above 98%) and lightweight structures. The AX-CNF hydrogel with a CA content of 1 wt% revealed a favorable network structure with respect to the swelling ratio; nanofiber addition resulted in a five-fold increase in the degree of swelling (68 g of water per g). The compressive properties were improved when the higher CA content (5 wt%) was used; when combined with CNF, there was a seven-fold enhancement in the compressive strength. The AX-CNF hydrogels were prepared using a green and straightforward method that utilizes sustainable resources efficiently. Therefore, such natural hydrogels could find application potential, for example in the field of soft tissue engineering.

 Received 2nd October 2018
Accepted 8th November 2018

DOI: 10.1039/c8ra08166b

rsc.li/rsc-advances

1. Introduction

Amongst polysaccharides, cellulose and its nano-derivatives have been extensively utilized to form natural hydrogels.¹ Research has also increasingly focused on the use of hemicellulose as a promising, low-cost, biodegradable and biocompatible precursor for hydrogels.² Arabinoxylan (AX) is the primary hemicellulose found in annual plants, and is also readily available in residues and side-streams in the agricultural industry.³ Furthermore, AX exhibits antioxidant and anti-inflammatory properties because of its ferulic acid content. It also has a vital function in nature, providing rigidity to plant cell walls *via* the crosslinking of polysaccharides and lignin.⁴

Many methods are used to process hydrogels to engineer their properties depending on their intended use; this renders them more attractive for use in a wide range of fields. The large-scale production of packaging materials represents one area where more environmentally friendly products, which allow for biodegradation, are required.⁵ In addition, the biocompatibility of natural structures is beneficial with regard to biomedical applications, such as tissue engineering.⁶

The term aerogel is increasingly used for porous structures dried through different means, such as supercritical drying from alcogel,⁷ or freeze casting *via* lyophilization.⁸ The latter allow for drying directly from water, though both approaches can be applied for the assembly of highly porous, 3D structures that can be used as is, or rehydrated to form a natural hydrogel.

The mechanical robustness of hemicellulose hydrogels have previously shown to be improved by bio-mimicking concepts using cellulose nanofibers (CNFs) as functional and renewable reinforcement material.^{8,9} Another approach involves crosslinking *via* chemical or physical means for structural stability, enabling water uptake without the occurrence of disintegration.¹⁰ However, to maintain the low environmental impact that the raw material source offers, as well as its biodegradability and biocompatibility, the use of greener, non-toxic crosslinking agents should be considered. Citric acid (CA) is regarded as a non-toxic and relatively inexpensive crosslinking agent that has been used to modify polysaccharides such as cellulose¹¹ and xylan.^{12,13}

Still, the limited number of available commercial products consisting of natural hydrogels is related, to some extent, to the inadequate mechanical properties of the hydrogels. In addition, these hydrogels have high production costs, and a relatively complex preparation procedure is required to transform the raw material into the final product.⁶

Lignin-containing materials are a promising approach to reduce cost and energy input as well as need of chemical pre-treatments for efficient conversion technologies. The presence of lignin have been associated with enhanced mechanical performance in aqueous environment,¹⁴ yet also lower hydrophilicity¹⁵ of natural nanofiber structures.

^aDivision of Materials Science, Luleå University of Technology, 97187, Luleå, Sweden.
E-mail: kristiina.oksman@ltu.se

^bDivision of Fluid and Experimental Mechanics, Luleå University of Technology, 97187, Luleå, Sweden

^cDepartment of Wood and Paper Science and Technology, Faculty of Natural Resources, University of Tehran, Karaj, Iran

^dFibre and Particle Engineering, University of Oulu, Oulu, Finland

† Electronic supplementary information (ESI) available: X-ray microtomography videos of 3D reconstruction of AX and AX-CNF samples at 5 wt% CA content. See DOI: 10.1039/c8ra08166b



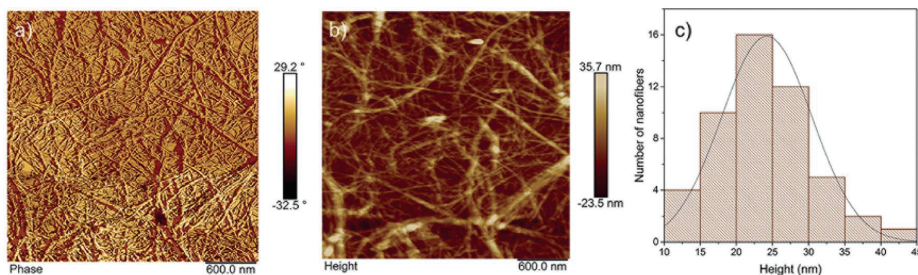


Fig. 1 AFM (a) phase and (b) height images of the cellulose nanofibers following the ultrafine grinding process, and (c) size distribution of the nanofiber width, measured from the height image.

Part of the complexity for hemicellulose-based materials lies in obtaining high purity *i.e.* low lignin content and low color value hemicellulose.¹⁶ Still there have been limited research on the feasibility of processing and properties of lignin-containing biomaterials overall and hemicellulose hydrogels in particular.^{17,18} A better understanding of their properties and the role of CNFs on hydrogel formation can offer new insight into green and efficient conversion of hemicellulose-based hydrogels.

In this study, freeze-casted CA crosslinked hydrogels was formed using lignin-containing AX, where water and CNFs were used as a solvent and as reinforcing building blocks, respectively. This provides an alternative route for the preparation of natural, barley-residue-based hydrogels with superior swelling and mechanical behaviors to those formed with AX alone. It is also important to use straightforward and green processing procedures to prepare the product from the raw materials, hence improving the prospects of commercial use. The aim of this study is to understand the role of the CNFs, in relation to the lignin-containing AX, and to study the effect of crosslinking using various amounts of CA, on the structure–property relationships of the hydrogels. This study characterizes the properties of the as-prepared aerogels with regard to their surface characteristics and internal structures. It also characterizes the formation of the hydrogels with regard to their swelling and mechanical behavior.

2. Experimental

2.1. Materials

2.1.1 Hemicellulose. AX, extracted from barley (*Hordeum vulgare*) husk, was purchased from Xylophane AB (Gothenburg, Sweden). The molar mass was $34 \times 103 \text{ g mol}^{-1}$.¹⁹ This is composed of 48.5 wt% xylose, 11.7 wt% arabinose, and 3.8 wt% glucose, with a xylose to arabinose ratio of 4.15. It also contains 19.6 wt% lignin, 6.8 wt% protein, 4.2 wt% fats, 4.3 wt% ash, and less than 1 wt% starch, as reported by the supplier.

2.1.2 Crosslinking agent. A CA ACS reagent, $\geq 99.5\%$, was purchased from Sigma-Aldrich (Saint Louis, USA), with a molecular weight of $192.12 \text{ g mol}^{-1}$.

2.1.3 Cellulose nanofibers. CNFs were prepared from brewers' spent grain (BSG), which was obtained following the

malting and brewing process from a large Finnish brewery. Purification was performed using a procedure described in a previous study, wherein following the purification process a chemical composition of 70 wt% cellulose, 23 wt% hemicellulose, and 4.2 wt% lignin was reported.²⁰ Secondly, the pulp was fibrillated according to a previously reported method.²⁰ Briefly, a 2 wt% suspension was fibrillated using a super mass colloid MKCA6-3 (Masuko Sangyo Co., Ltd. Kawaguchi, Japan), which was operated at 1500 rpm, with a minimum gap of $\sim 90 \text{ }\mu\text{m}$. The atomic force microscopy (AFM) phase and height images of the prepared CNFs are shown, together with their size distribution, in Fig. 1. The size distribution was based on the measurements of 50 nanofibers; the average width (height) was $24 \pm 6 \text{ nm}$.

2.2. Preparation of the aerogels

The AX and CA were first mixed in distilled water, under magnetic stirring at $30 \text{ }^\circ\text{C}$, until the AX dissolved (1 h). The CNFs were added, under continuous stirring, to obtain an AX/CNF ratio of (1 : 1), where the polysaccharide (AX, AX/CNF) content of the distilled water solution was 2 wt%. Various CA contents of 1, 3, and 5 wt% were used. The viscous suspensions were dispersed using a dispersing instrument UltraTurrax, IKA T25, (IKA®-Werke GmbH & Co. KG, Staufen, Germany) operated at 10 000 rpm for 10 min. They were then cast in plastic Petri dishes, where the base of the mold was subsequently exposed to liquid nitrogen. The samples were stored in a freezer at a temperature of approximately $-20 \text{ }^\circ\text{C}$ for at least 24 h prior to lyophilization, which was conducted for 48 h using a freeze-dryer Alpha 2-4 LD plus (CHRIST GmbH, Osterode am Harz, Germany), under a temperature of $-40 \text{ }^\circ\text{C}$ and vacuum of 0.12 mbar. The freeze-casted aerogels were subsequently allowed to react for 3 h within an oven at $120 \text{ }^\circ\text{C}$ to activate the CA crosslinker. In addition, samples of each composition were maintained at room temperature as control samples with regard to the heat-activated crosslinking reaction. Fig. 2 shows the process used to prepare the aerogel, which was allowed to swell in water to form a hydrogel. In this study, the prepared cross-linked gel-structures are referred to as AX, and the structures with the addition of cellulose nanofibers are denoted as AX-CNF.



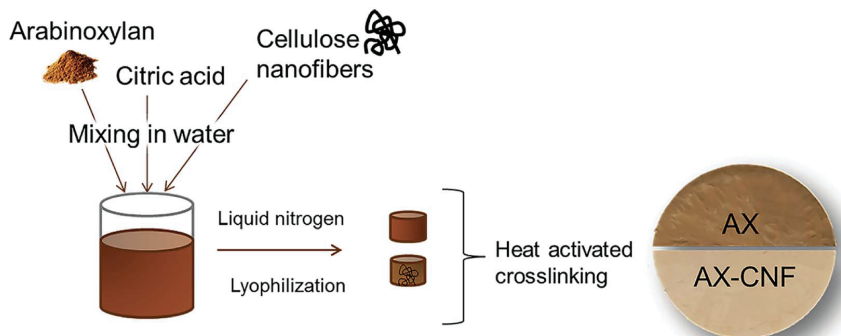


Fig. 2 Schematic representation of the procedure used to prepare AX- and AX-CNF aerogels.

2.3. Characterization

2.3.1 Density and porosity. The density of the aerogels, denoted as ρ_{aerogel} , was calculated using a gravimetric method; an analytic balance was used to determine the weight of the aerogels, and a micro-meter gauge was used to measure the thickness of the aerogels, based on an average of ten different measurements. The level of porosity was subsequently calculated using the density value; it was assumed that the skeletal density ($\rho_{\text{cellulose}}$) of the aerogel was represented by cellulose,²¹ namely 1.46 g cm^{-3} :

$$\text{Porosity (\%)} = 100 \times [1 - (\rho_{\text{aerogel}}/\rho_{\text{cellulose}})] \quad (1)$$

2.3.2 Swelling properties. The pre-weighed aerogels were immersed in distilled water at room temperature to determine their swelling capacity. The swollen hydrogels were removed from the distilled water, and gently blotted in filter paper to remove any excess water. The hydrogels were then weighed at regular intervals until an equilibrium state was reached; this was achieved after 48 and 56 h for the AX-CNF and AX samples, respectively. The data were measured in triplicate and the average values are reported. The equilibrium swelling ratio was calculated using the following equation:⁸

$$\text{Swelling ratio (g g}^{-1}\text{)} = [(W_2 - W_1)/W_1] \quad (2)$$

where W_1 and W_2 denote the mass of the sample under the aerogel state and the swollen hydrogel state, respectively.

Wettability of the surface of the aerogel was characterized via water contact angle measurements using an EASYDROP contact angle measuring system, which incorporated drop shape analysis control (DSA1) and evaluation software (Krüss GmbH, Hamburg, Germany). A 4 μL drop of water was placed onto the sample, and the instrument software calculated the contact angle, over time, using a sessile drop technique; the reported values are the average of ten measurements.

2.3.3 Mechanical performance. Uniaxial compression tests were performed on the swollen crosslinked hydrogels in their equilibrium state at 25 $^{\circ}\text{C}$ using a dynamic mechanical analyzer

DMA Q800 (TA Instruments, New Castle, USA). The samples were compressed up to a strain of 100%, at a strain rate of $10\% \text{ min}^{-1}$. Prior to each test, the samples were preloaded using a load of 0.05 N. The modulus ($E_{<5\%}$) was calculated from the initial linear region of the stress-strain curves with a strain level below 5%. In addition to the maximum compressive strength (σ) the materials were compared by the stress ($\sigma_{50\%}$) and tangent modulus ($E_{50\%}$) at a 50% compressive strain level. For each gel, samples, with dimensions of $15 \times 15 \text{ mm}$, and a height of 10 mm were tested eight times for reproducibility reasons; the average results are reported.

2.3.4 Fourier transform infrared (FTIR) analysis. FTIR spectra were recorded using a FTIR spectrometer VERTEX 80 (Bruker Corp., Billerica, USA) to determine any changes in the functional groups of the AX and AX-CNF aerogels (5 wt%). The highest concentration of 5 wt% was chosen in order to amplify the FTIR signals. The absorbance mode was used to analyze the samples over the wavelength range of $4000\text{--}400 \text{ cm}^{-1}$. For the analysis, a disk was prepared from finely ground samples, which were mixed with KBr, using a pressure of 400 kg cm^{-2} for a period of about 1 min.

2.3.5 Scanning electron microscopy (SEM). The microstructure of the aerogels fractured surfaces along the freezing direction, as prepared with liquid nitrogen, was observed using a SEM JSM-IT300LV (JEOL®, Tokyo, Japan) at an acceleration voltage of 15 kV. The samples were coated using a coating system (Bal-Tec MED 020) with a tungsten target. The coating was performed within a vacuum of approximately 6×10^{-5} mbar, under a current of 100 mA, for 20 s to obtain a coating thickness of 3–5 nm.

X-ray microtomography was used to examine the 3D internal microstructure for two of the aerogels (AX and AX-CNF) at 5 wt% CA content. The samples of approximate size $4 \times 4 \times 4 \text{ mm}$, were scanned using a Zeiss Xradia 510 Versa (Carl Zeiss, Pleasanton, CA, USA), using a $20\times$ objective, which allowed interior tomography with a field of view (FOV) of 0.66 mm, and the spatial resolution 0.67 μm (voxel size). The scanned region of interest (ROI) was positioned in the exact center of each aerogel sample. The scanning was carried out with an X-ray tube voltage of 60 kV, an output effect of 5 W, and without any X-ray



Table 1 Density and porosity values of the aerogel samples

Sample code	Density (g cm^{-3})	Porosity (%)
AX-1CA	0.023 ± 0.002	98.33 ± 0.00
AX-3CA	0.028 ± 0.002	98.13 ± 0.01
AX-5CA	0.028 ± 0.001	98.13 ± 0.00
AX-1CA-CNF	0.019 ± 0.002	98.73 ± 0.00
AX-3CA-CNF	0.023 ± 0.003	98.47 ± 0.01
AX-5CA-CNF	0.024 ± 0.002	98.40 ± 0.00

filters. A total number of 2201 projections were acquired with an exposure time of 4 s, which resulted in a total scan time of 3 h and 20 min. The tomographic reconstruction was carried out using filtered backprojection, within Zeiss Scout-and-Scan Reconstructor software (version 11.1). The 3D visualization and analysis of the microstructure in the aerogels were obtained using Dragonfly Pro software (ORS).

3. Results and discussion

3.1. Porosity of aerogels and their hydrogel formation

The density and porosity of the crosslinked aerogels were measured based on their weight prior to being immersed in water for hydrogel formation. For all samples, porous lightweight structures were obtained after freeze casting and heat activated crosslinking; the average porosity value was 98.4% (Table 1). The average porosity of the samples is comparable to that of hemicellulose-based gels obtained from spruce galactoglucomannans (GGM) and reinforced with wood nanofibers, namely $98.45 \pm 0.23\%$ on average.⁸ Furthermore, the values obtained in this study can also be compared to those of cellulose-based gels, namely TEMPO-oxidized wood nanofibers, which were prepared using various solvents prior to sublimation, and have porosity values of 92.8–99%.²¹ The porosity of the hydrogels is regarded a critical parameter with regard to their

performance in scaffolds designed for tissue-engineering applications. Here, the highly porous and interconnected microarchitecture provides a large surface area relative to the volume of the scaffold. This promotes cell growth and new tissue formation.¹⁰ The crosslinking, as well as the addition of CNFs, appeared to have a limited influence on the porosity values; the difference between the highest and lowest values was 0.6%.

The rehydration of the aerogels for the hydrogel formation and their degree of swelling was the initial assessment in terms of maintaining its structural stability in contact with water, thus reflecting the crosslinking. Both the visual appearance of the samples upon their immersion in water, and the swelling equilibrium of the hydrogels are shown in Fig. 3.

All the prepared hydrogels displayed an opaque color, as shown in Fig. 3. The effect of lignin on hemicellulose extraction has previously been reported by Liu *et al.*¹⁶ The aforementioned study showed that the presence of lignin limited the dissolution of the hemicellulose and resulted in a relatively dark-colored hemicellulose. This was caused by the linking of the hemicellulose and the formation of lignin-carbohydrate complexes. The AX hydrogels could be visually distinguished because they had a darker color than that of the AX-CNF hydrogels; owing to their greater hemicellulose and lignin contents. When compared with the control samples that were maintained at room temperature, the hydrogels that were placed in an oven after the freeze-casting process, for the heat-activated crosslinking reaction to occur, appeared to have been successfully crosslinked. Thus, the control samples exhibited increased solubility, and consequently, immediately following immersion, lost their structural integrity. This can be observed in Fig. 3 (left). However, the AX hydrogel with a CA content of 1 wt%, which was presumed to have been crosslinked, also disintegrated upon weighing. Consequently, the crosslinked AX-CNF hydrogels were the only samples that were capable of retaining water without their structural stability being

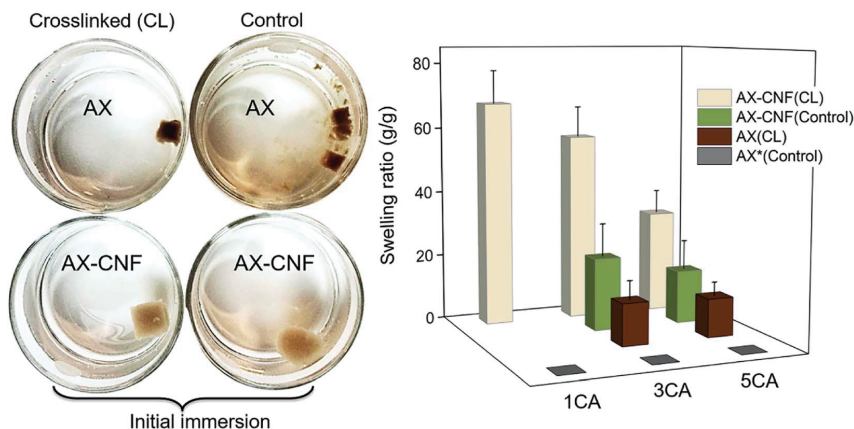


Fig. 3 Photograph of the hydrogels with a CA content of 1 wt%, captured immediately following their immersion in water (left). Effect of the CA concentration and CNF addition on the equilibrium swelling ratio (right).



compromised at a low CA ratio. At equilibrium, the weight of these samples increased by up to 68 (± 10) times their initial weight (Fig. 3, right). This may be attributed to the occurrence of crosslinking between the hydroxyl groups of the cellulose nanofibers and the carboxyl groups of CA,¹¹ which further stabilizes the structure, although the crosslinking-agent quantities were low. The degree of swelling of the AX-CNF hydrogels obtained from barley residues was generally greater than those of other nanoreinforced hemicellulose-based hydrogels prepared with comparable techniques, such as liquid-nitrogen followed by lyophilization. Galactoglucomannans (GGM), obtained from spruce and reinforced with nanofibers, absorbed up to 37 g of water per g.⁸ Furthermore, glucuronoarabinoxylan (GAX), obtained from oat spelt and reinforced with nanocrystals, displayed a holding capacity of 25 g of water per g.²²

As the CA content of the hydrogels increased, a reduction in the degree of swelling was observed for all the hydrogels (Fig. 3); this indicates that there was an increase in the crosslinking density of the samples. This resulted in the presence of a less impenetrable network within the hydrogel, which diminished the swelling ratio.

Interestingly, when the CNF addition was equal to the AX quantity, the structure appeared to be maintained even without the heat-activated crosslinking reaction, as shown in Fig. 3 for the control samples (AX-CNF) with CA contents of 3 and 5 wt%. Moreover, this indicates that the physical bonds formed by the CNFs are not solely responsible for the maintenance of the structures, since the sample with the CA content of 1 wt% lost its shape. Furthermore, this suggests that during processing, the presence of CA, above a content of 3 wt%, has an influence on the structural stability of the sample to some extent. Azeredo *et al.*²³ indicated that, even at room temperature, the crosslinking reaction occurred within hemicellulose films with CA.

Another plausible influencing factor could be owed to the presence of structural irregularities in the form of asymmetrical pores. These are often created during rapid freezing conditions such as that of liquid-nitrogen, and thus undermine stability.²⁴

The wetting behavior towards water was assessed to further compare the surface water adsorption performance of the various aerogels with respect to the degree of crosslinking and CNF addition. Instant complete wetting behavior was observed for all the AX-CNF aerogels, where the water droplets were adsorbed into the samples in less than one second. Consequently, no contact angles could be measured, with the exception of the AX samples, which showed a more gradual adsorption. This could be partly because the AX aerogels have a greater lignin content, which has a hydrophobic nature, than the AX-CNF aerogels, where hydrophilic cellulose constitutes an equal part of the aerogel. The continuous wetting processes of the AX aerogels with CA contents of 1, 3, and 5 wt% are presented in a series of photographs, shown in Fig. 4a, together with the measured contact angle as a function of time, shown in Fig. 4b.

As shown in Fig. 4a, two wetting regimes were observed during the tests. Initially, good wettability was observed, and over time, complete wetting rapidly occurred for all the AX aerogels irrespective of the CA content. However, the time required to achieve complete wetting appeared to be related to the CA content, where the wettability tended to increase as the quantity of the crosslinking agent increased, as shown in Fig. 4b. Increased hydrophilicity has previously been reported in studies involving the crosslinking of xylan¹² and cellulose²⁵ with CA. This was explained by the incorporation of carboxyl groups on the surface of the material. The contact angle of the AX aerogels decreased as the CA content increased (Fig. 4); this was followed by instant, complete wetting with the CNF

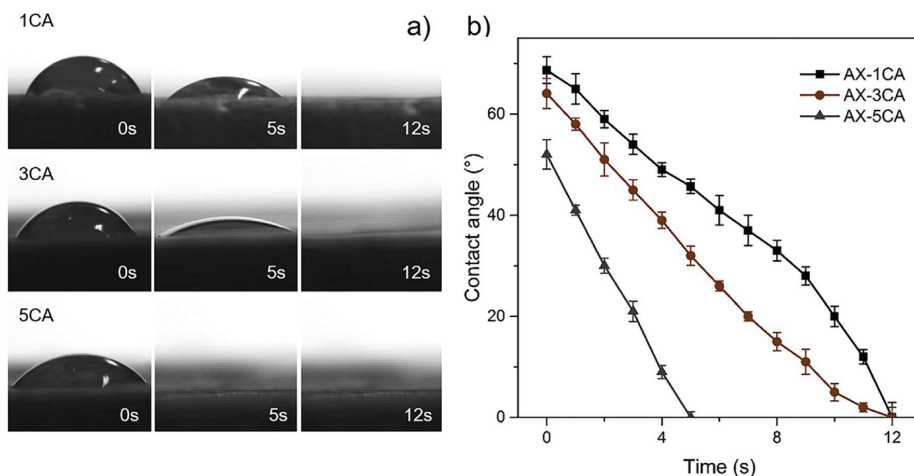


Fig. 4 (a) Photographs of the various water adsorption rates of the AX aerogels with CA contents of 1, 3, and 5 wt%, and (b) the measured contact angle, as a function of time, of the AX aerogels with CA contents of 1, 3, and 5 wt%.



Table 2 Compressive strength (σ) and modulus ($E_{<5\%}$) determined at the initial portion (strain < 5%) of the stress versus strain curves, and stress ($\sigma_{50\%}$) and compressive modulus ($E_{50\%}$) determined at 50% strain level

Sample code	σ (kPa)	$E_{<5\%}$ (kPa)	$\sigma_{50\%}$ (kPa)	$E_{50\%}$ (kPa)
AX-3CA	11.3 \pm 4.4	32.6 \pm 19.2	1.2 \pm 0.6	17.7 \pm 2.2
AX-5CA	16.1 \pm 3.0	40.9 \pm 17.1	1.8 \pm 0.4	20.2 \pm 2.0
AX-1CA-CNF	67.2 \pm 11.2	24.9 \pm 13.2	1.5 \pm 0.5	4.5 \pm 2.4
AX-3CA-CNF	80.7 \pm 9.4	33.3 \pm 9.0	2.9 \pm 0.6	13.2 \pm 2.6
AX-5CA-CNF	115.7 \pm 6.2	50.4 \pm 10.3	4.9 \pm 0.4	27.1 \pm 3.1

addition. These observations indicate that the hydrophilicity of the samples increased, which correlates with the greater equilibrium swelling ratio of the AX-CNF hydrogels, as well as the faster time to obtain equilibrium state.

In the case of the hydrogels, the swelling force is counteracted by the retractive force that is induced by the crosslinked polymer network.²⁶ This consequently affects their mechanical behavior. Therefore, the hydrogels that were insoluble in water during the swelling test were assumed to be adequately crosslinked. These samples were further tested under compression.

3.2. Mechanical properties of the hydrogels

The compressive stress, as a function of strain, was studied to see the effect of the CNF on the compressive properties of the crosslinked AX hydrogels. The mechanical properties of the hydrogels are displayed in Table 2. The representative compressive stress-strain curves are shown in Fig. 5a, and enlarged for 50% strain level in Fig. 5b.

As can be seen in Table 2, the maximum compressive strength (σ) of the AX hydrogels with CA contents of 3 and 5 wt% was significantly increased with the CNF addition, representing a seven-fold enhancement, respectively.

The highest strength (116 kPa) of the nanoreinforced AX hydrogel were superior to those reported for a commercially used, synthetic poly(*N*-isopropylacrylamide) (PNIPAM, temperature-responsive polymer) hydrogel reinforced with TEMPO-oxidized CNFs (79.6 kPa), which was tested under similar conditions.²⁷ In a previous study, the compression stresses of xylan-rich hemicellulose hydrogels were reported to increase from 13.6 kPa to 38.6 kPa as the degree of crosslinking increased.²⁸ This behavior was also observed for both σ and $\sigma_{50\%}$ of all hydrogels (Table 2 and Fig. 5).

As shown in Fig. 5a, the nanoreinforced hydrogels exhibited "J"-shaped curves, which is typical behavior for soft, biological

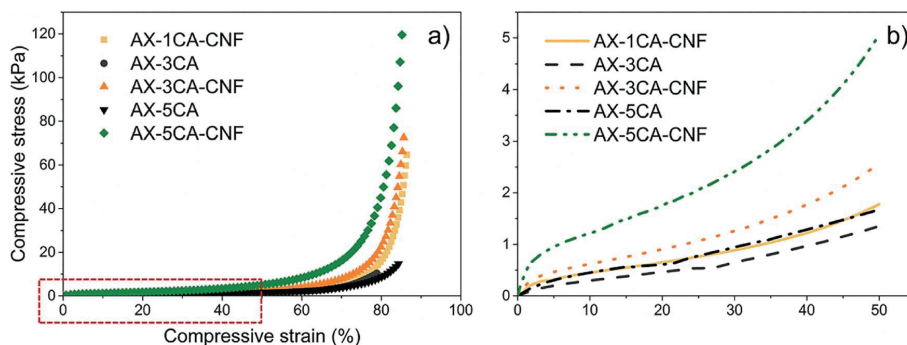


Fig. 5 (a) Representative compressive stress-strain curves of the equilibrium swollen AX-CNF hydrogels with CA contents of 1, 3, and 5 wt%, and the AX hydrogels with CA contents of 3 and 5 wt%. *AX-1-CA disintegrated in water, and was not tested in compression. (b) The representative compressive stress-strain curves enlarged at 50% strain.

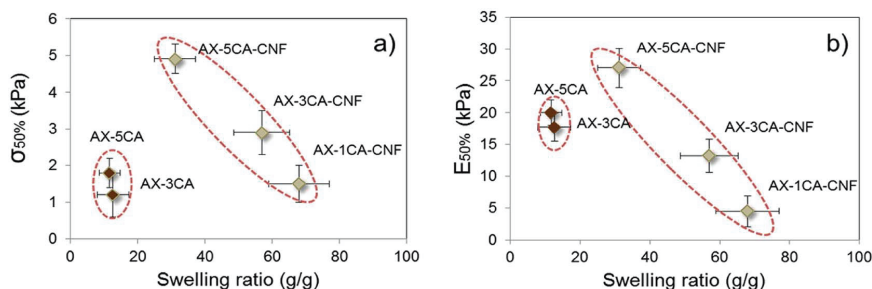


Fig. 6 (a) Compressive strength ($\sigma_{50\%}$) and (b) compressive modulus ($E_{50\%}$) of hydrogels as a function of their swelling ratio.



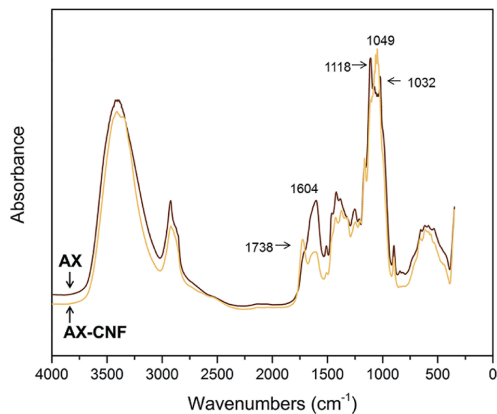


Fig. 7 FTIR spectra of the AX and AX-CNF aerogels with CA contents of 5 wt%; obtained following crosslinking.

tissues such as natural tendons and ligaments²⁹ and has previously been reported for nanoreinforced hemicellulose-based hydrogels.³⁰

To produce soft tissue-engineering scaffolds with sufficient mechanical support, the modulus of the material should lie between 10 kPa and 350 MPa.³¹ For all the hydrogels in this study, the modulus calculated over the linear strain region (Table 2) lie within the lower range of this interval.

The correlation between swelling degree and compressive modulus has previously been reported for hemicellulose-reinforced nanofiber hydrogels and explained by the plasticizing effect of water.⁹ The water content has also been reported to strongly affect both compressive strength and modulus of

nanoreinforced- polyvinyl alcohol³² and gelatin/chitosan³³ hydrogels negatively. The mechanical properties as a function of swelling degree were thus investigated for the hydrogels in this study at 50% strain, and presented in Fig. 6.

A descending trend was apparent for $\sigma_{50\%}$ (Fig. 6a) and $E_{50\%}$ (Fig. 6b) of AX-CNF hydrogels with increased swelling. As described in Section 3.1, the reduction in swelling could be explained by the structure stabilization through crosslinking, which in turn was expected to result in enhanced mechanical properties. However, also noticeable from Fig. 6 was that the AX samples were grouped closely together; deviating by their low strength and moderate modulus in relation to their lower swelling ratio. This could be explained by a combination of inadequate crosslinking and the less hydrophilic nature of the lignin-containing AX hydrogels. Inhomogeneous crosslink density distribution, known as spatial inhomogeneity has been reported to dramatically reduce the strength of hydrogels,³⁴ this is further in agreement with the significantly lower $\sigma_{50\%}$ of AX samples in comparison to their nanoreinforced counterpart at equivalent amount of CA (Fig. 6a).

The hydrophobic nature of lignin combined its natural role as a structural material providing rigidity to plants is likely an influential factor on hydrogel behavior acting to reduce the swelling meanwhile conceivably providing stiffness for the AX samples as seen for $E_{50\%}$ in Fig. 6b, this was also apparent from Table 2 for the resistance towards initial pore wall bending of the structure as calculated over the linear region, $E_{<5\%}$.

3.3. FTIR-analysis

Following the heat-activated reaction with CA, FTIR spectroscopy was used to compare the AX and AX-CNF samples, as presented in Fig. 7, and study any changes that occurred during crosslinking.

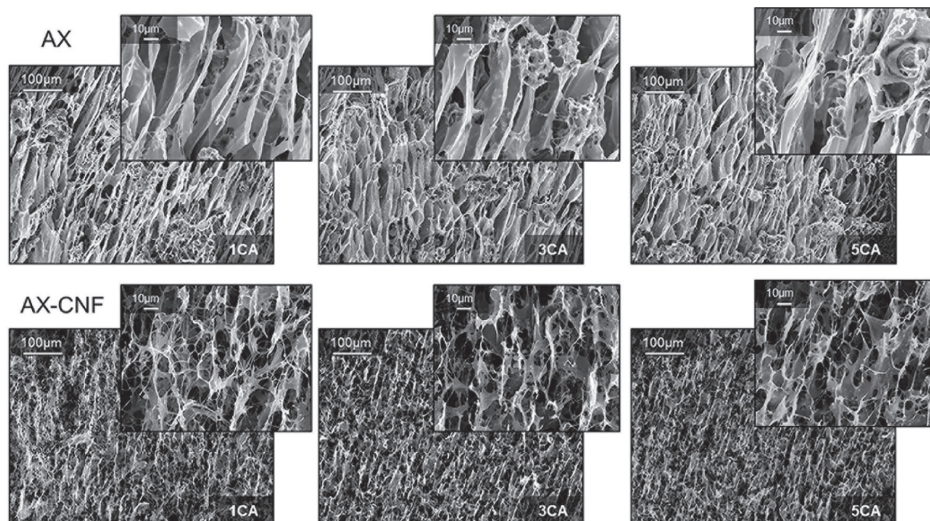


Fig. 8 SEM fracture surfaces along the freezing direction of the AX and AX-CNF aerogels with CA contents of 1, 3, and 5 wt%.



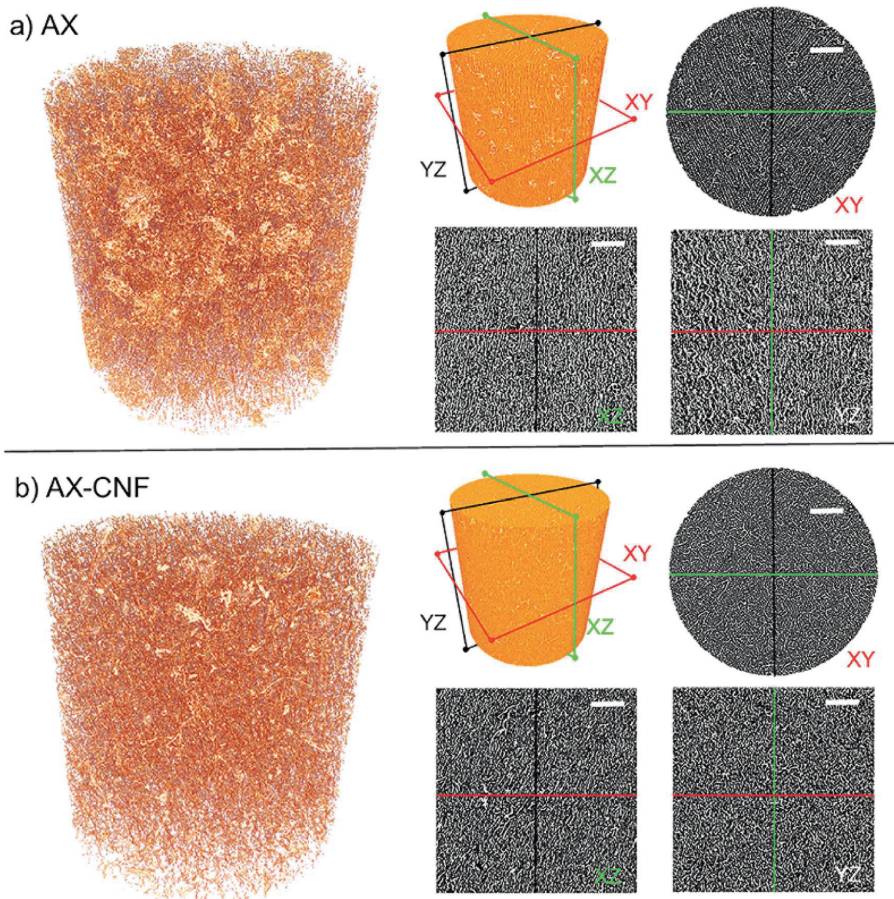


Fig. 9 X-ray microtomography 3D reconstruction of the pore structure of (a) AX and (b) AX-CNF and schematic representation of their cross-sectioning for imaging of the aerogels at a CA content of 5 wt% at different sections, respectively. The scale bar corresponds to 100 μm.

As shown in Fig. 7, the AX sample displays a peak at 1118 cm^{-1} . However, in the case of the AX-CNF sample, the peak shifts and is represented at 1049 cm^{-1} ; both these peaks are reported to be indicative of AX.³⁵ In addition, the AX sample also revealed a peak at 1032 cm^{-1} , which was assigned to the deformation vibrations of C-H bonds within the aromatic rings associated with lignin.³⁶ The peak at 1604 cm^{-1} , which is ascribed to the presence of carboxyl groups, was observed in the spectra of both aerogels; however, this peak was more intense in the case of the AX samples (Fig. 7). This peak was previously reported for xylan-based hydrogels that were crosslinked with CA.¹³

A shoulder was observed at around 1738 cm^{-1} in the case of the AX sample; however, a distinct peak appeared at the same position in the case of the AX-CNF aerogel (Fig. 7). This is assigned to the characteristic stretching bands of carbonyl groups of ester groups. It could be owed to the ester linkage of

the carboxylic groups of the *p*-coumaric- and ferulic acids of the hemicellulose and/or lignin.³⁷ Previous researchers, which observed such signals near 1738 cm^{-1} , have also described the peak to be related to anhydride formation. This is an intermediate reaction that is required for the reaction between the CA and hydroxyl groups, and observed during the modification of cellulose¹¹ and xylan¹² with CA contents of 20 wt% or greater. The absence of a distinct peak related to AX may be attributed to the relatively low quantity of CA used in this study.

The results from Fig. 7 indicate that in the presence of the cellulose nanofibers (AX-CNF), the crosslinking of the xylan backbone, *via* the reaction with the CA, appeared to be intensified compared with that of the AX alone. This could be attributed to the three hydroxyl groups of the cellulose, which are available at each monomer unit for esterification. However, the hemicelluloses only possess one or two hydroxyl groups, and thus, they are less susceptible to modification.³⁵



3.4. Morphology

The microstructures of the aerogels fractured surfaces in the freezing direction prepared with liquid nitrogen were observed using electron microscope and the micrographs are shown in Fig. 8.

As shown in the top row of Fig. 8, an oriented, channel-like structure dominates the inner architecture of the AX aerogel. During the initial liquid-nitrogen freezing process, ice crystals are formed and grow in the direction parallel to the temperature gradient.³ Hence, after sublimation the bottom-up freezing direction of the AX samples displayed an ordered arrangement of elongated channels in the crystal growth direction. The second row of results shows that the formation of a network structure with open interconnected pores was promoted when the CNFs were introduced as a component; this possibly contributed to the superior absorption ability of the sample. However, the crystal growth direction appeared to have been impeded by the introduction of nanofibers, thus the AX-CNF aerogel displayed a less oriented structure, in comparison to that of AX. Orientation of aerogel pores upon freeze casting has previously been described for some polysaccharides, such as AX, glucuronoxylan (GX), glucuronarabinoxylan (GAX),³ guar galactomannan (GM), and galactoxyloglucan (XG).³⁸ However, the oriented structure of GAX, as observed with electron microscope was reported to be maintained when cellulose nanocrystals was used as reinforcement³

Alakalhunmaa *et al.*⁸ reported the formation of CNFs with oriented lamellar structures during unidirectional freezing, which acted as support pillars within the pore walls, and were thus responsible for the load-bearing ability of the material. This is in agreement with the results of the compression testing in this study; the nanofibers could be responsible for the reinforcement effect, which potentially could be further promoted by their orientation to some extent. When the CA content was increased, there was no obvious variation observed in the scanned images of the AX and AX-CNF, as shown in Fig. 8. This indicates that the aerogel structure that formed during the freeze-casting was not affected by the differences in the CA contents, and also that the structure was maintained throughout the various assembly steps.

The influence of nanofibers on the architectural features was further investigated by X-ray microtomography and presented in Fig. 9. The morphologies seen in two-dimensional microscopy images (Fig. 8) were confirmed from Fig. 9, displaying porous structures. A fibrillar network architecture with the addition of CNFs (b) can be observed in comparison to the clearer channel type structure of AX (a). Furthermore, the preferred growth direction of the ice crystals resulting in oriented pores in the freezing direction for both AX (a) and AX-CNF (b) was confirmed, though the AX-CNF sample showed a less uniform orientation, as observed from the XZ and YZ sections. From Fig. 9, the pores of AX (a) and AX-CNF (b) appeared uniformly distributed in the horizontal (XY), as well as vertical (XZ) and (YZ) sections of the scans. This can be further observed from the 3D reconstruction videos of the samples provided in ESI.1 and ESI.2.†

4. Conclusions

In conclusion, highly porous lignin-containing AX-based 3D structures were crosslinked using CA, and reinforced with CNFs. This was achieved by applying a green and robust processing route, which was combined with the effective usage of sustainable resources obtained from inexpensive underutilized barley residues. The compressive properties of the hydrogels were improved by the incorporation of the nanofibers, which resulted in reinforcement and a seven-fold increase in the compressive strength. The CNF addition also promoted the crosslinking, as shown by the FTIR results. The reinforcement effect is believed to have been further promoted by the orientation of the aerogel structure, as shown by the electron microscopy and X-ray microtomography observations. Furthermore, there was a five-fold increase in the degree of swelling; this is likely to be attributed to the formation of a favorable, interconnected network architecture, which is due to the presence of the CNFs.

At low CA contents (1 wt%), the swelling was promoted, where the final weight of the sample was 68 times greater than its initial weight. When the amount of crosslinking agent was increased to 5 wt%, the compressive strength and modulus were improved, but the adsorption performance was impaired. Therefore, the 3 wt% threshold could be used depending on the desired function for the intended application.

The addition of cellulose nanofibers in combination with CA crosslinking greatly promoted the hydrogel formation and properties of AX, thus resulting in an alternative green and efficient processing route of lignin-containing hemicellulose hydrogel that could potentially be used commercially for soft tissue engineering applications.

Conflicts of interest

There are no conflicts to declare.

Acknowledgements

This work was supported by Bio4Energy, a strategic research environment appointed by the Swedish government and WOOD-PRO – the Nordic Forest Research Co-operation Committee (SNS) project.

Notes and references

- 1 K. Oksman, Y. Aitomäki, A. P. Mathew, G. Siqueira, Q. Zhou, S. Butylina, S. Tanpichai, X. Zhou and S. Hooshmand, *Composites, Part A*, 2016, **83**, 2–18.
- 2 L. S. Hu, M. H. Du and J. P. Zhang, *Open J. For.*, 2018, **8**, 15–28.
- 3 T. Köhnke, A. Lin, T. Elder, H. Theliander and A. J. Ragauskas, *Green Chem.*, 2012, **14**, 1864–1869.
- 4 N. Kumar and V. Pruthi, *Biotechnol. Rep.*, 2014, **4**, 86–93.
- 5 A. R. V. Ferreira, V. D. Alves and I. M. Coelho, *Membranes*, 2016, **6**, 1–17.
- 6 J. Ma, X. Li and Y. Bao, *RSC Adv.*, 2015, **5**, 59745–59757.



- 7 G. Pajonk, *J. Phys., Colloq.*, 1989, **50**, 13–22.
- 8 S. Alakalhunmaa, K. Parikka, P. A. Penttilä, M. T. Cuberes, S. Willför, L. Salmén and K. S. Mikkonen, *Cellulose*, 2016, **23**, 3221–3238.
- 9 J. Liu, G. Chinga-Carrasco, F. Cheng, W. Xu, S. Willför, K. Syverud and C. Xu, *Cellulose*, 2016, **23**, 3129–3143.
- 10 V. J. Reddy, S. Radhakrishnan, R. Ravichandran, S. Mukherjee, R. Balamurugan, S. Sundarajan and S. Ramakrishna, *Wound Repair Regen*, 2013, **21**, 1–16.
- 11 C. Demitri, R. Del Sole, F. Scalera, A. Sannino, G. Vasapollo, A. Maffezzoli, L. Ambrosio and L. Nicolais, *J. Appl. Polym. Sci.*, 2008, **110**, 2453–2460.
- 12 A. Salam, R. A. Venditti, J. J. Pawlak and K. El-Tahawy, *Carbohydr. Polym.*, 2011, **84**, 1221–1229.
- 13 S. Wang, H. Li, J. Ren, C. Liu, F. Peng and R. Sun, *Carbohydr. Polym.*, 2013, **92**, 1960–1965.
- 14 S. S. Nair and N. Yan, *Cellulose*, 2015, **22**, 3137–3150.
- 15 E. Rojo, M. S. Peresin, W. W. Sampson, I. C. Hoeger, J. Vartiainen, J. Laine and O. J. Rojas, *Green Chem.*, 2015, **17**, 1853–1866.
- 16 K. X. Liu, H. Q. Li, J. Zhang, Z. G. Zhang and J. Xu, *Bioresour. Technol.*, 2016, **214**, 755–760.
- 17 D. Kai, J. T. Mein, L. C. Pei, K. C. Yun, L. Y. Yong and J. L. Xian, *Green Chem.*, 2016, **18**, 1175–1200.
- 18 X. Song, F. Chen and S. Liu, *Bioresources*, 2016, **11**, 6378–6392.
- 19 M. Gröndahl, L. Bindgård, P. Gatenholm and T. Hjertberg, *US Pat.*, 2014/0093724A1, 2014.
- 20 L. Berglund, M. Noël, Y. Aitomäki, T. Öman and K. Oksman, *Ind. Crops Prod.*, 2016, **92**, 84–92.
- 21 H. Sehaqui, Q. Zhou and L. A. Berglund, *Compos. Sci. Technol.*, 2011, **71**, 1593–1599.
- 22 T. Köhnke, T. Elder, H. Theliander and A. J. Ragauskas, *Carbohydr. Polym.*, 2014, **100**, 24–30.
- 23 H. M. C. Azeredo, C. Kontou-Vrettou, G. K. Moates, N. Wellner, K. Cross, P. H. F. Pereira and K. W. Waldron, *Food Hydrocolloids*, 2015, **50**, 1–6.
- 24 K. R. Hixon, T. Lu and S. A. Sell, *Acta Biomater.*, 2017, **62**, 29–41.
- 25 M. G. Raucci, M. A. Alvarez-Perez, C. Demitri, D. Giugliano, V. De Benedictis, A. Sannino and L. Ambrosio, *J. Biomed. Mater. Res., Part A*, 2015, **103**, 2045–2056.
- 26 A. Borzacchiello and L. Ambrosio, in *Hydrogels: biological properties and applications*, ed. R. Barbucci, Springer-Verlag, Milan, 2011, pp. 9–20.
- 27 J. Wei, Y. Chen, H. Liu, C. Du, H. Yu, J. Ru and Z. Zhou, *Ind. Crops Prod.*, 2016, **92**, 227–235.
- 28 X. W. Peng, J. L. Ren, L. X. Zhong, F. Peng and R. C. Sun, *J. Agric. Food Chem.*, 2011, **59**, 8208–8215.
- 29 V. Guarino, A. Gloria, R. de Santis and L. Ambrosio, in *Biomedical applications of hydrogels handbook*, ed. R. M. Ottenbrite, et al., Springer Science, New York, 2010, pp. 227–245.
- 30 Y. Guan, B. Zhang, J. Bian, F. Peng and R. C. Sun, *Cellulose*, 2014, **21**, 1709–1721.
- 31 R. Jin and P. J. Dijkstra, in *Biomedical applications of hydrogels handbook*, ed. R. M. Ottenbrite, et al., Springer Science, New York, 2010, pp. 203–225.
- 32 S. Butylina, S. Geng and K. Oksman, *Eur. Polym. J.*, 2016, **81**, 386–396.
- 33 N. Naseri, J. M. Poirier, L. Girandon, M. Fröhlich, K. Oksman and A. P. Mathew, *RSC Adv.*, 2016, **6**, 5999–6007.
- 34 O. Okay, in *Hydrogel Sensors and Actuators*, ed. G. Gerlach and K. F. Arndt, Springer-Verlag, Berlin Heidelberg, 2009, pp. 1–14.
- 35 J. M. Fang, R. C. Sun, J. Tomkinson and P. Fowler, *Carbohydr. Polym.*, 2000, **41**, 379–387.
- 36 F. G. Calvo-Flores, J. A. Dobado, J. Isac-García and F. J. Martín-Martínez, in *Lignin and lignans as renewable raw materials: chemistry, technology and applications*, ed. C. V. Stevens, John Wiley & Sons, West Sussex, 2015, pp. 164–166.
- 37 M. Sain and S. Panthapulakkal, *Ind. Crops Prod.*, 2006, **23**, 1–8.
- 38 K. S. Mikkonen, K. Parikka, J. P. Suuronen, A. Ghafar, R. Serimaab and M. Tenkanen, *RSC Adv.*, 2014, **4**, 11884–11892.

